P2

NASA CR-121212
IITRI-B6107-34
(Part 2)

FINAL REPORT

ADDITIONAL THERMAL FATIGUE DATA ON NICKEL- AND COBALT-BASE SUPERALLOYS

By

Maurice A. H. Howes
Metals Research Division

IIT RESEARCH INSTITUTE
10 West 35th Street
Chicago, Illinois 60616

Prepared for

NATIONAL AERONAUTICS AND SPACE ADMINISTRATION

March 15, 1973

CONTRACT NAS3-14311

NASA-Lewis Research Center
Cleveland, Ohio

Peter T. Bizon, Project Manager

1. Report No.
NASA CR-121212

2. Government Accession No.

3. Recipient's Catalog No.

4. Title and Subtitle
ADDITIONAL THERMAL FATIGUE DATA ON NICKEL- AND COBALT-BASE SUPERALLOYS

5. Report Date
March 15, 1973

6. Performing Organization Code

7. Author(s)
Maurice A. H. Howes

8. Performing Organization Report No.
IITRI-B6107-34 (Part 2)

10. Work Unit No.

9. Performing Organization Name and Address
IIT Research Institute
10 West 35 Street
Chicago, Illinois 60616

11. Contract or Grant No.
NAS 3-14311

13. Type of Report and Period Covered
Contractor Report
6/11/70-2/28/73

12. Sponsoring Agency Name and Address
National Aeronautics and Space Administration
Washington, D.C. 20546

14. Sponsoring Agency Code

15. Supplementary Notes
Project Manager, Peter T. Bizon, Materials and Structures Division, NASA-Lewis Research Center, Cleveland, Ohio 44135

16. Abstract

The fluidized bed technique has been used to measure the relative thermal-fatigue resistance of 21 superalloys: B1900, B1900 DID, IN-100, MAR-M 200, Udimet 700 wrought and cast, NX-188, WAZ-20, TAZ-8A, M22, IN 713C, IN 738, IN 162, MAR-M 509, René 80, RBH, NASA VI A, TD-NiCr, MAR-M 302, WI-52, and X-40. IN-100, MAR-M 200, NX-188, WAZ-20 and TAZ-8A were also tested in the directionally solidified form. B1900, B1900 DID, IN-100, MAR-M 200, Udimet 700, NX-188, WAZ-20 and TAZ-8A were tested with surface protection. Among the 36 variations of composition, solidification method, and surface protection the cycles to cracking differed by 2-3 orders of magnitude. Some alloys suffered serious weight losses and oxidation. Previous fluidized bed thermal fatigue data on some of these alloys were reported in NASA CR-72738. Thermal fatigue data, oxidation, and dimensional changes are reported in NASA CR-121211. Metallographic and hardness data are given in this report. This investigation is part of a general study of thermal fatigue conducted by the NASA-Lewis Research Center.

17. Key Words (Suggested by Author(s))
Thermal Fatigue
Coatings
Nickel Base Alloys
Cobalt Base Alloys
Oxidation
Fluidized Bed

18. Distribution Statement
Unclassified - Unlimited

19. Security Classif. (of this report)	20. Security Classif. (of this page)	21. No. of Pages	22. Price*
Unclassified	Unclassified	75	$3.00

* For sale by the National Technical Information Service, Springfield, Virginia 22151

FOREWORD

This report describes the work performed under NASA Contract NAS3-14311 on the project entitled "Thermal Fatigue Testing of High-Temperature Alloys." The report covers the period June 11, 1970 to February 28, 1973. Other fluidized bed thermal fatigue data of nickel- and cobalt-base alloys obtained between March 24, 1967 and May 20, 1970 is reported in NASA CR-72738.

This report is presented in two parts. Part 1 (NASA CR-121211) describes the thermal fatigue testing and the results obtained. Part 2, this report, describes the metallographic examination.

The NASA personnel assigned to this contract were:

Leonard W. Schopen - Contracting Officer
Peter T. Bizon - Project Manager

The IITRI personnel who contributed to this project include Maurice Howes (Project Manager), E. R. Porlier (Administrative Supervisor), R. K. Nolen, G. Grzeda, T. Croak, E. Chester, L. Hopkins, and V. Johnson.

Data are contained in Logbooks No. C20053, C20054, C20059, C200902, and C20061.

The IITRI internal designation for this report is IITRI-B6107-34 (Part 2).

Preceding page blank

TABLE OF CONTENTS

	Page
SUMMARY	1
INTRODUCTION	2
METALLOGRAPHY	3
HARDNESS MEASUREMENTS	4
RESULTS	4
B1900 and B1900 DID	4
IN-100	5
MAR-M 200	5
Udimet 700	5
Udimet 700 (SEW) Clad + Xcoat B	5
NX-188	6
WAZ-20	6
TAZ-8A	7
M22	7
IN-713C	7
IN-738	8
IN-162	8
MAR-M 509	8
René 80	8
RBH	8
NASA VI A	8
TD-NiCr	9
MAR-M 302	9
WI-52	9
X-40	9
DISCUSSION AND CONCLUSIONS	9
REFERENCES	11

PRECEDING PAGE BLANK

LIST OF FIGURES

		Page
1	Microstructure of B1900 Specimens.	17
2	Microstructure of B1900 DID + Jocoat Specimens	21
3	Microstructure of IN-100 Specimens	24
4	Microstructure of IN-100 Directionally Solidified. . .	28
5	Microstructure of IN-100 Directionally Solidified + Jocoat	30
6	Microstructure of MAR-M 200 Specimens.	33
7	Microstructure of Udimet 700 Wrought Specimens	34
8	Microstructure of Udimet 700 Cast Specimens.	35
9	Microstructure of Udimet 700 (SEW) Clad + Xcoat B. . .	37
10	Microstructure of NX-188 Specimens	40
11	Microstructure of NX-188 with RT-1A Coating.	43
12	Microstructure of NX-188 Directionally Solidified. . .	45
13	Microstructure of NX-188 Directionally Solidified + RT-1A Coating.	48
14	Microstructure of WAZ-20 + Jocoat.	51
15	Microstructure of WAZ-20 Directionally Solidified + Jocoat	54
16	Microstructure of TAZ-8A	57
17	Microstructure of TAZ-8A (SEW) Clad + Xcoat B.	60
18	Microstructure of TAZ-8A Directionally Solidified. . .	64
19	Microstructure of M22 Specimens.	65
20	Microstructure of IN 713C Specimen	66
21	Microstructure of IN 738 Specimen.	67
22	Microstructure of IN 162 Specimen.	68

LIST OF FIGURES (cont.)

		Page
23	Microstructure of MAR-M 509.	69
24	Microstructure of René 80.	70
25	Microstructure of RBH.	70
26	Microstructure of NASA VI A Alloy.	71
27	Microstructure of TD-NiCr Specimens.	72
28	Microstructure of MAR-M 302.	73
29	Microstructure of WI-52.	74
30	Microstructure of X-40 Specimens	75

LIST OF TABLES

1	Samples Sectioned for Metallographic Examination . . .	12
2	Hardness Change in Set G Specimens (Not Coated). . . .	13
3	Hardness Change in Set H Specimens (Not Coated). . . .	14
4	Hardness Change in Set I Specimens (Not Coated). . . .	15
5	Microhardness Surveys From Surface and From Side of Crack.	16

SUMMARY

This investigation is part of a general study of thermal fatigue conducted by the NASA-Lewis Research Center. This program used the fluidized bed heating and cooling technique to measure the relative thermal fatigue resistance of 21 superalloys. An earlier investigation is reported in NASA CR-72738. The alloys in this investigation included B1900, B1900 DID, IN-100, MAR-M 200, Udimet 700 (cast and wrought), NX-188, WAZ-20, TAZ-8A, M22, IN-713C, IN-738, IN-162, MAR-M 509, René 80, RBH, NASA VI A, TD-NiCr, MAR-M 302, WI-52, and X-40. Four types of surface protection were used on selected alloys. These were Jocoat, Xcoat A, clad + Xcoat B, and RT-1A coat. The IN-100, MAR-M 200, NX-188, WAZ-20, and TAZ-8A were tested in both the random and directional solidified forms. The resistance to cracking was measured by cycling specimens between fluidized beds at 1129°C and 357°C, 1046°C and 274°C, and 1088°C and 316°C. The time of immersion in each bed was 3 minutes. The specimens were examined for cracks at intervals, and the lengths of the first three cracks were measured. When sufficient crack propagation data were obtained, the specimen was removed from test.

The tested alloys having the best resistance to thermal fatigue cracking were NX-188 directionally solidified and TAZ-8A clad + Xcoat B. The number of cycles required to crack different alloys varied widely, from over 6100 cycles for the best materials to 13 cycles for several of the worst materials. This represents a 500:1 difference in behavior under very severe testing conditions. Oxidation occurs during thermal cycling and some alloys experienced considerable weight loss. The directionally solidified alloys were particularly susceptible and normally should be protected with a coating.

Metallographic examination indicates that as much attention should be given to processing the alloy as to the alloy composition. Directional solidification is an obvious case of process improvement of properties but other techniques of controlling microstructure are also important. Any structure with a large constituent or line of constituents is potentially weak in thermal fatigue. The test results indicate that processing should be designed to give a fine well-dispersed structure without a pronounced dendritic pattern and without grain boundaries lined with carbides or blocks of other constituents.

INTRODUCTION

The purpose of the reported work was to use the fluidized bed technique to measure the relative thermal fatigue cracking resistance of twenty-one high-temperature superalloys that could be used for advanced air breathing engines. The study included metallographic and hardness studies before and after thermal fatigue testing. The work was carried out in a facility designed and built by IIT Research Institute.

This investigation is part of a general study of thermal fatigue being undertaken by the NASA-Lewis Research Center. Other parts of the study and the possible use of the data are described by Spera.(1) An earlier part of this general study was the previous fluidized bed thermal fatigue work by Howes.(2) An analytical life prediction to these data is given by Spera et al.(3)

Thermal fatigue is a possible failure mechanism in any situation that involves fluctuating temperatures. If certain materials are heated or cooled rapidly and continuously, cracking sometimes occurs. This phenomenon, which is often called thermal shock, is caused by thermal gradients present during rapid temperature change. As a result, strain is produced which is related to the coefficient of expansion of the material. Failure occurs when thermally induced stresses exceed the strength of the material after starting as a crack in the most sensitive area. In metals, the thermal fatigue mechanism often results in the gradual formation of a network of cracks and is commonly referred to as craze cracking, heat cracking, or fire cracking. Any part which undergoes temperature cycling during service is likely to fail by this mechanism.

Failures due to thermal fatigue can be found in brake drums, turbine blades, internal combustion engine pistons, rolls for forming hot steel, forging dies, railway wheels, furnace components, and in molds used for glass and metal molding. Thermal fatigue can become the dominant failure mode in aircraft gas turbine engines as the operating temperature and thermal gradients become more severe and the expected service life becomes longer.

Many methods of heating and cooling have been used to simulate the thermal cycles experienced in actual applications. Some of the earliest work used direct flame impingement on a surface. However, unless carefully controlled, the combustion products and variation in temperature conditions can introduce an arbitrary environment which can influence the cracking mechanism.

High-frequency heating and electrical resistance heating systems can be used to establish simulated thermal cycling conditions; however, they are generally expensive to construct for the

multi-station test facilities which are needed to amass data quickly. In the consideration of thermal fatigue, the crack propagation rate is as important as the start of cracking. For instance, a material that cracks early might be satisfactory if the crack propagation rate is very slow. With high frequency and resistance heating, the formation of a crack alters the flux or current densith in such a way that the crack is overheated and measurement of propagation rate becomes meaningless.

The fluidized bed heating system for thermal fatigue testing has many advantages and no significant disadvantages. The bed construction is simple and relatively inexpensive. The rate of heat transfer to a specimen or group of specimens is high. The heat content of a particulate solid fluidized media is also high, so that a large number of specimens or a large specimen can be rapidly and repeatedly heated without lowering the bed temperature significantly. The fluid bed system uses low-velocity air flows (on the order of 1 fps), and in this respect the high-velocity gas flows in a turbine engine are not simulated. The first reported use of fluidized beds for thermal fatigue testing was in 1958 by Glenny and co-workers.[4] Since that time there have been many reports of the use of this technique to evaluate thermal fatigue resistance.[5-13] A bibliography of the literature of thermal fatigue up to 1967 was compiled by Carden.[14]

The original high-temperature bed described by Glenny was 6 in. in diameter and was heated by wire-wound elements of 4 kw total input. For this program much heavier loads of test specimens had to be cycled, and a bed diameter of 11.5 in. with a power input of 55 kw was required. The low-temperature bed was controlled at an intermediate temperature instead of room temperature; thus the lower temperature beds were required to have provisions for both heating and cooling.

The entire report is presented in two parts. Part 1 (NASA CR-121211) includes all thermal fatigue results, together with weight and dimensional changes. Part 2, this report, describes the metallographic and hardness measurements.

METALLOGRAPHY

At the end of the test program 100 samples were sectioned for metallography. The sections taken are listed in Table 1. For the longitudinal sections a portion containing a major crack was cut and mounted in a thermosetting plastic. Transverse sections were taken at the center of the specimens. Samples were prepared in the conventional way using automatic polishing with final finishing using a microcloth wheel and 0.05 micron abrasive powder. Kalling's reagent was used for the majority of the etched samples.

HARDNESS MEASUREMENTS

At various inspection times during thermal cycling hardness readings were taken on all uncoated samples. A Rockwell C hardness was taken on the surface at the center of the specimen and a 1 kg DPH taken at the end of the 0.040 in. radius after cleaning the surface with fine emery paper. Results for the three series of tests are given in Tables 2, 3, and 4.

Microhardness surveys were taken on selected metallographic samples in two positions:

1. From the surface near the mid-section of the specimen, starting in a coating or layer if present.

2. Below the surface starting from the edge of a major crack.

Hardness impressions were made at 0.002, 0.004, 0.006, 0.010, and 0.015 in. from the surface or crack. Photomicrographs were taken to illustrate selected microhardness surveys. Microhardness survey results are given in Table 5.

RESULTS

All sections detailed in Table 1 were examined and photomicrographs were made of selected samples. These are presented in Figures 1 to 30. A total of 100 specimens were sectioned. The longitudinal sections were selected to contain a major crack and several possible crack sites on the 0.025 in. edge. These sections were taken parallel to the mid-chord plane of the specimen. Transverse sections were complete cross sections taken at or near the center of the specimen.

B1900 and B1900 DID (Figures 1 and 2)

The typical structure of B1900 is shown in Figure 1. Note the gamma matrix with dispersed gamma prime and the light-etching carbide particles mainly at the grain boundaries. The light-etching surface layer is due to oxidation and possible depletion of some alloying elements. Figures 1g, 1h, and 1i show B1900 with a Jocoat layer, which has diffused into the base material. The transverse section (1i) shows that more grain boundary carbides exist below the surface than near the surface. Figure 1c and 1d show

longitudinal samples of B1900 from stress-rupture bars and are similar to the structure shown in Figure 1a.

Thermal cracks appear to initiate at and progress along grain boundaries as typified by Figures 1e and 1f.

B1900 DID is shown in Figure 2. These structures are similar but show increased gamma prime and a tendency for complex carbides to appear within the grain. The Jocoat layer appears well diffused and coherent on all sections examined.

IN-100 (Figures 3 to 5)

Figure 3c shows the typical cast structure of IN-100 with small white patches of primary gamma prime. At 500X (Figure 3d) the eutectic formation of the primary gamma prime is clearly seen together with a complex carbide. Dispersed carbides are seen throughout the structure, and a possible path for crack propagation is evident at the grain boundaries.

The appearance of Jocoat and Xcoat A is shown in Figure 3f, g and i. Both are adequately bonded and would appear to be equally effective.

Directionally solidified samples are shown in Figures 4 and 5. Primary gamma prime is more evident, and some grain boundaries are clearly delineated but do not break surface (Figure 5c). The sides of the cracks are oxidized, as shown in Figures 4d and 4e. Cracks apparently follow grain boundaries.

MAR-M 200 (Figure 6)

Typical structures are shown in Figure 6. In general cracks follow the grain boundaries.

Udimet 700 (Figures 7 and 8)

Typical wrought and cast structures are shown in Figures 7 and 8.

Udimet 700 (SEW) Clad + Xcoat B (Figure 9)

This alloy is shown in Figure 9 and consists of precipitated gamma prime within the gamma matrix with dispersed carbide. There

is a tendency for carbides to form at grain boundaries (Figure 9e). These grain boundaries run directly to the metal-cladding interface providing easy crack propagation paths if the cladding becomes detached, as it has in Figures 9a and 9b.

The cladding shows poor adhesion to the base metal with little or no diffusion to help bonding. This type of cladding cannot be effective until the bonding is improved. Generally, areas that showed good bonding were free from cracking.

NX-188 (Figures 10 to 13)

The NX-188 shows the usual gamma prime structure with some evidence of the presence of primary gamma prime. There is a definite dendritic cast pattern (Figure 10e) with interdendritic carbides (Figure 10f). NX-188 is shown with the RT-1A coating in Figure 11; although the diffusion bond does not appear as well diffused as Xcoat A or Jocoat (Figures 3 and 5), it seems to be adequate for good adhesion.

NX-188 DS is shown in Figures 12 and 13. These sections show gamma prime/gamma structures with little evidence of grain boundary weakness except in the transverse sections (Figures 12f and 13f). The oxidized surface in Figure 12 shows clear evidence of depletion which extends down the sides of cracks (Figure 12c). The RT-1A coating appears to be diffused very well into the DS alloy (Figure 13), but the coating appears to be attacked.

WAZ-20 (Figures 14 and 15)

Both WAZ-20 and WAZ-20 DS show pronounced dendritic type structures remaining after casting. It appears that severe compositional gradients may exist. The combination of dendrites and grain boundaries provides easy paths for cracking in the random solidified alloys (Figure 14c). The bond between the Jocoat and the alloy is deficient since the coating is quickly lost. The alloy also oxidizes and scales rather badly after the coating is gone.

The directionally solidified alloy (Figure 15) shows similar structures except that the dendrites appear to block the line of cracking and failure initiates at wide notches instead of deep cracks (Figure 15a). Islands of complex carbides are common in these structures (Figure 15c).

TAZ-8A (Figures 16 to 18)

One of the puzzling features of the thermal fatigue results was why the TAZ-8A single-edge wedge specimens exhibited superior thermal fatigue resistance to the double-edge wedge specimens. Geometry alone could not account for the large difference. This question is easily answered by reference to Figure 16c where the pronounced dendritic pattern of the double wedge can be seen. Dendrites are present in the single wedge (Figure 16e) but to a much lesser degree. This difference can be produced in the same composition by processing differences. For instance, if a hot mold is used, the solidification pattern is more even and there is greater opportunity for diffusion to occur. Also an oxide (such as nickel oxide) may be incorporated in the first slurry as a grain refiner. This helps the formation of a fine structure during solidification.

Figures 16d and 16f show that this structure consists basically of primary gamma prime and gamma prime in a gamma matrix. There is very little evidence of carbide formation.

The clad sample shown in Figure 17 shows that the cladding does not form a good bond with the substrate and cannot be relied upon at this stage of development although it has provided some protection. The cladding is nonprotective, and the interface is attacked once the cladding is breached (see Figure 17d, e, and f).

The TAZ-8A directionally solidified material is shown in Figure 18, and it appears that the poorer performance of this alloy may be due to the interconnected areas of primary gamma prime. The random solidified structure shown in Figure 16e can be expected to perform better than the directionally solidified structure shown in Figure 18a because of the large islands of gamma allowing easy crack propagation paths.

This composition shows alloy depletion from the surface and from the edges of cracks and should benefit from a reliable coating system.

M22 (Figure 19)

Typical M22 structures are shown in Figure 19.

IN-713C (Figure 20)

The untested IN-713C structure is shown in Figure 20.

IN-738 (Figure 21)

This structure consists of primary gamma prime, precipitated gamma prime, and dispersed carbides in a gamma matrix. Alloy depletion takes place from the surface and from the edges of the crack.

IN-162 (Figure 22)

The untested IN-162 structure is shown in Figure 22.

MAR-M 509 (Figure 23)

This is a cobalt-base alloy, and the structure consists of MC particles in script form with a few areas of $M_{23}C_6$ particles in eutectic form and precipitate form in the dendritic alpha solid-solution matrix. Figure 23b shows that oxidation occurs preferentially at the carbide particles, and there is a tendency to form wide notches rather than tight cracks.

René 80 (Figure 24)

This alloy consists of gamma prime in a gamma matrix with some dispersed carbides and a definite carbide layer at the grain boundaries. Figure 24 shows a crack propagating along the carbide at the boundaries.

RBH (Figure 25)

This structure consists of primary or eutectic M_6C particles and MC particles in the solid solution matrix. The carbide formation at the grain boundaries provides lines of weakness for crack propagation.

NASA VI A (Figure 26)

This alloy contains dispersed primary gamma prime of considerable size and precipitated gamma prime in a gamma matrix. There are well-dispersed carbides throughout the structure. The crack

propagation path appears to prefer the boundaries between the primary gamma prime and the other constituents (Figure 26b).

TD-NiCr (Figure 27)

This structure contains rather large precipitated particles in the fine-grained solid-solution matrix. There seems to be a very definite grain boundary weakness making crack propagation easy and rapid. This is evidenced by the large number of cracks at the grain boundaries.

MAR-M 302 (Figure 28)

The untested structure of MAR-M 302 is shown in Figure 28.

WI-52 (Figure 29)

The untested structure of WI-52 is shown in Figure 29.

X-40 (Figure 30)

The cobalt-base alloys seem to have a greater variety of structure than the nickel-base alloys. This structure is again carbides in a solid-solution matrix, but the presence at grain boundaries is more pronounced (Figure 30b). This produces lines of weakness (Figure 30c) and also easy paths for the penetration of oxidation products.

DISCUSSION AND CONCLUSIONS

In the development of superalloys in the past major attention has been given to obtaining high strength and creep resistance with possibly good corrosion resistance and thermal stability. Thermal fatigue resistance was barely considered. Obtaining a high performance alloy is a matter of compromise, and a structure that resists creep may be inferior in a thermal fatigue situation.

In the present investigation and also in the previous work (NASA CR-72738), there is ample evidence that as much attention should be given to processing as to the actual alloy composition.

Directional solidification is an obvious case of improvement of properties by several orders of magnitude, but other techniques may be equally important. Any structure with a large constituent or line of constituents is potentially weak in thermal fatigue. Examination of the microstructures when compared with the thermal fatigue test results indicates that processing should be arranged to give a fine well-dispersed structure without a pronounced dendritic pattern and without grain boundaries lined with carbides or blocks of other constituents.

In the testing completed the results indicate trends but not the absolute order since some of the alloys may not be in the optimum condition as regards their structure.

REFERENCES

1. Spera, D. A., "Aerospace Structural Materials," NASA-SP-227, November 1969, pp. 43-57.

2. Howes, M. A. H., "Thermal Fatigue Data on 15 Nickel- and Cobalt-Base Alloys," NASA CR-72738, 1970.

3. Spera, D. A., et al., "Thermal Fatigue Resistance of 15 High-Temperature Alloys Determined by the Fluidized-Bed Technique," NASA TMX-52975, March 1971.

4. Glenny, E., et al., "A Technique for Thermal-Shock and Thermal-Fatigue Testing Based on the Use of Fluidized Solids," J. Inst. Metals, 87, 1958-1959, 294-302.

5. Glenny, E., and Taylor, T. A., "A Study of the Thermal-Fatigue Behavior of Metals," J. Inst. Metals, 88, 1959-1960, 449-461.

6. Cox, M., and Glenny, E., "Thermal Fatigue Investigations," Engineer, 210, 1960, 346-350.

7. Glenny, E., and Taylor, T. A., "The Thermal Fatigue Behavior of Metals," J. Inst. Metals, 89, 1960-1961, 439 (discussion).

8. Glenny, E., "Thermal Fatigue," Met. Rev., 6 (24), 1961, 387-465.

9. Glenny, E., "A Study of the Significant Factors Governing the Thermal Fatigue Behavior of High-Temperature Alloys," Ph.D. Dissertation, University of London, 1962.

10. Franklin, A. W., et al., "Some Metallurgical Factors Influencing the Thermal Fatigue Resistance of Wrought Ni-Cr-Base High-Temperature Alloys," J. Inst. Metals, 92, 1963-1964, 313-321.

11. Glenny, E., and Northwood, J. E., "Some Observations on the Thermal-Fatigue Behavior of Casting Alloys for Gas-Turbine Blading," Foundry Trade J., 119, 1965, 607-620.

12. Glenny, E., and Restall, J. E., "Evaluation of the Properties of Protected Molybdenum and 0.45 Percent Titanium-Molybdenum Alloy," J. Less-Common Metals, 9, 1965, 367-387.

13. Northwood, J. E., et al., "An Evaluation of a Chromium-Base Alloy for High-Temperature Service," J. Less-Common Metals, 14, 1968, 157-165.

14. Carden, A. E., "Bibliography of the Literature on Thermal Fatigue," Rep. MH67-AEC-3, NASA Grant NsG-381, August 1967, 120 pp.

TABLE 1. - SAMPLES SECTIONED FOR METALLOGRAPHIC EXAMINATION

Specimen	As Received	Tested S-R Bars	Long. 1915/ 525°F (Set H)	Long. 1990/ 600°F (Set I)	Long. 2065/ 675°F (Set G)	Trans. 2065/ 675°F (Set G)
B1900	b	1	1	b		
B1900 + Jocoat				b	1	1
B1900 DID + Jocoat	1			1	1	1
IN-100	b	1	1	b		
IN-100 + Jocoat	1		1	b	1	1
IN-100 + Xcoat A			1	1	1	1
IN-100 DS	b	1		b	1	1
IN-100 DS + Jocoat	1			b	1	1
MAR-M 200	b	1	1	b		
MAR-M 200 + Jocoat				1	1	
MAR-M 200 DS				b	1	
Udimet 700 Wrought	b	1	1	b		
Udimet 700 Cast	b	1	1	b		
Udimet 700 Wrought, Clad + Xcoat B (SEW)[a]				-	1	1
NX-188	c			1	1	1
NX-188 + RT-1A Coat	c			1	1	1
NX-188 DS	c			1	1	1
NX-188 DS + RT-1A Coat	c			1	1	1
WAZ-20 + Jocoat				1	1	1
WAZ-20 DS + Jocoat				1	1	1
TAZ-8A	b	1	1	b	1	
TAZ-8A (SEW)[a]				1	1	1
TAZ-8A Clad + Xcoat B (SEW)[a]				-	1	1
TAZ-8A DS	1			1	1	1
M22	b	1	1	b		
IN 713C	b	1	1	b		
IN 738	1		1	1	1	
IN 162	b	1	1	b		
MAR-M 509	1		1	1	1	
René 80	1		1	1	1	
RBH	1			1	1	
NASA VI A	1		1	1	1	
TD-NiCr	b	1	1	b	1	
MAR-M 302	b	1	1	b		
WI-52	b	1	1	b		
X-40	b	1	1	b	1	
TOTAL	9	14	19	16	26	16

Total Sections = 100

[a]Single Edge Wedge

[b]From CR-72738

[c]Sectioned by NASA-Lewis

TABLE 2. - HARDNESS CHANGE IN SET G SPECIMENS (NOT COATED)

2065/675°F (1129/357°C) cycle, 3 min dwell in each bed

Alloy and Condition	Spec. Ident.	Original Hardness	Hardness After Given Cycles											
			25	50	100	200	300	500	1100	2200	2400	2900	5100	6500
			Microhardness on 0.040 in. Radius, DPH (1 kg load)											
IN-100 DS	7	422	393	393	-	386	-	386	376	-	-	350		
MAR-M 200 DS	3	454	445	437	-	427	-	427	427	-	428			
NX-188	1	503	-	-	445	412	-	397						
NX-188 DS	1	519	-	-	445	371	-	371	356	-	-	-	-	344
TAZ-8A		544	538	524	-	501	-	462	454					
TAZ-8A (SEW)		490	490	-	490	-	-	-	483	-	-	-	454	
TAZ-8A DS	1	463	-	-	454	440	-	440	437	437				
IN-738	2	422	-	-	407									
MAR-M 509	9	413	413	413	-	399	-	399						
René 80	1	405	-	-	374									
RBH	1	285	-	-	299	328	333							
NASA VI A	2	483	475	452	-	454	438							
TD-NiCr		293	285	285	-	250								
X-40		422	402	402	-	362	360							
			Surface Hardness on Center Section, R_C											
IN 100 DS	7	38	37	37	-	36	-	35	35	-	-	35		
MAR-M 200 DS	3	41	40	39	-	37	-	37	37	-	36			
NX-188	1	39	-	-	38	37	-	33						
NX-188 DS	1	36	-	-	35	35	-	-	33	-	-	-	-	30
TAZ-8A		45	45	45	-	45	-	44	44					
TAZ-8A (SEW)		43	43	-	43	-	-	-	42	-	-	41		
TAZ-8A DS	1	42	-	-	42	42	-	41	40	39				
IN-738	2	39	-	-	38									
MAR-M 509	9	38	37	37	-	36	-	36						
René 80	1	42	-	-	38									
RBH	1	25	-	-	30	31	31							
NASA VI A	2	42	41	41	-	40	39							
TD-NiCr		30	29	28	-	26								
X-40		38	38	37	-	37	36							

TABLE 3. - HARDNESS CHANGE IN SET H SPECIMENS (NOT COATED)

1915/525°F (1046/274°C) cycle, 3 min dwell in each bed

Alloy and Condition	Original Hardness	Hardness After Given Cycles		
		50	200	500
Microhardness on 0.040 in. Radius, DPH (1 kg load)				
B1900	410	406	408	398
IN-100	399	371	372	-
MAR-M 200	431	434	395	-
Udimet 700 wrought	420	394	371	-
Udimet 700 cast	423	394	364	375
TAZ-8A	544	524	485	485
M22	416	429	416	402
IN 713C	423	413	399	372
IN 738	422	420	415	420
IN 162	423	421	413	393
MAR-M 509	412	406	371	372
René 80	405	413	423	421
NASA VI A	475	458	431	420
TD-NiCr	293	291	291	-
MAR-M 302	526	482	425	413
WI-52	420	431	375	377
X-40	422	398	398	393
Surface Hardness on Center Section, R_C				
B1900	38	38	37	37
IN-100	38	38	37	-
MAR-M 200	40	40	38	-
Udimet 700 wrought	40	38	37	-
Udimet 700 cast	38	36	36	35
TAZ-8A	45	44	44	44
M22	37	38	38	38
IN 713C	40	38	37	37
IN 738	39	39	38	37
IN 162	39	38	37	37
MAR-M 509	38	37	36	36
René 80	42	40	38	37
NASA VI A	42	42	41	40
TD-NiCr	31	29	29	-
MAR-M 302	49	44	43	41
WI-52	36	35	35	35
X-40	39	38	38	38

TABLE 4. - HARDNESS CHANGE IN SET I SPECIMENS (NOT COATED)

1990/600°F (1088/316°C) cycle, 3 min dwell in each bed

Alloy and Condition	Spec. Ident.	Original Hardness	Hardness After Given Cycles						
			50	300	500	700	1200	2000	4000
			Microhardness on 0.040 in. Radius, DPH (1 kg load)						
MAR-M 200 DS	12	454	445	437	-	437	428	428	428
NX-188	2	503	463	445	-	383			
NX-188	4	503	-	-	437				
NX-188 DS	2	524	480	445	-	437	420	395	370
NX-188 DS	4	503	480	445	-	437	428	383	370
TAZ-8A		560	524	524	-	524	500		
TAZ-8A (SEW)		490	490	490	-	490	483	498	503
TAZ-8A DS	2	454	445	445	-	445	445	445	445
TAZ-8A DS	4	463	445	445	-	445	445	445	445
IN-738	3	445	-	-	428				
MAR-M 509	15	412	454	454	-	420			
René 80	3	405	-	-	445				
RBH	2	285	-	-	333				
NASA VI A	14	483	483	445	-	437			
			Surface Hardness on Center Section, R_C						
MAR-M 200 DS	12	41	40	40	-	40	40	39	39
NX-188	2	40	39	38	-	38			
NX-188	4	39	-	-	37				
NX-188 DS	2	36	36	36	-	36	34	35	35
NX-188 DS	4	37	36	36	-	36	34	34	34
TAZ-8A		45	45	45	-	45	45		
TAZ-8A (SEW)		43	43	43	-	43	43	43	42
TAZ-8A DS	2	42	43	43	-	43	43	43	43
TAZ-8A DS	4	42	43	43	-	43	43	43	43
IN-738	3	39	-	-	39				
MAR-M 509	15	38	38	38	-	37			
René 80	3	42	-	-	41				
RBH	2	25	-	-	34				
NASA VI A	14	42	42	42	-	41			

TABLE 5. - MICROHARDNESS SURVEYS FROM SURFACE AND FROM SIDE OF CRACK

Specimen	Thermal Cycles	Microhardness Traverse, Knoop (200 g load)											
		From Surface						From Side of Crack					
		.002 in.	.004 in.	.006 in.	.010 in.	.015 in.	See Fig.	.002 in.	.004 in.	.006 in.	.010 in.	.015 in.	See Fig.
B1900 + Jocoat	1700	468[a]	510[a]	436	416	394		430	480	457	441	457	
B1900 DID + Jocoat	2300	569[a]	436	421	430	430		411	411	430	468	486	
IN-100 + Jocoat	300	619[a]	480	569	505	493		446	500	619	468	441	
IN-100 DS	2900	300	441	436	446	446		394	426	416	416	426	4d
IN-100 DS + Jocoat	2700	436[a]	486[a]	474	474	468	5d	408	372	372	416	416	
MAR-M 200 + Jocoat	550	457[a]	511	539	511	593		468	468	500	505	474	
MAR-M 200 DS	2400	486	505	525	525	546		511	546	554	546	546	
Udimet 700 Clad + Xcoat B (SEW)	1300	345	426	416	403	385	9b	403	421	408	436	408	
NX-188	500	411	411	397	416	403		421	421	421	394	441	
NX-188 + RT-1A Coat	1100	396[a]	411[a]	655[a]	380	372	11c	403	385	356	356	356	
NX-188 DS	6500	312	411	453	436	436	12d	372	436	397	321	312	
NX-188 DS + RT-1A Coat	6100	335[a]	325[a]	353	312	380	13d	297	297	321	321	335	
WAZ-20 + Jocoat	50	376	464	411	376	411	14b	411	411	404	404	464	
WAZ-20 DS + Jocoat	6100	411	427	427	376	385		397	411	427	346	390	15b
TAZ-8A	1100	506	487	454	506	506	16b	441	465	561	480	465	
TAZ-8A Clad + Xcoat B (SEW)	5100	442	526	627	601	510		454	500	426	487	540	17b
TAZ-8A DS	6100	480	465	506	506	495		546	601	546	512	465	
IN 738	200	436	442	442	442	422	21a	411	411	399	411	407	

[a]Indicates hardness impression in coating.

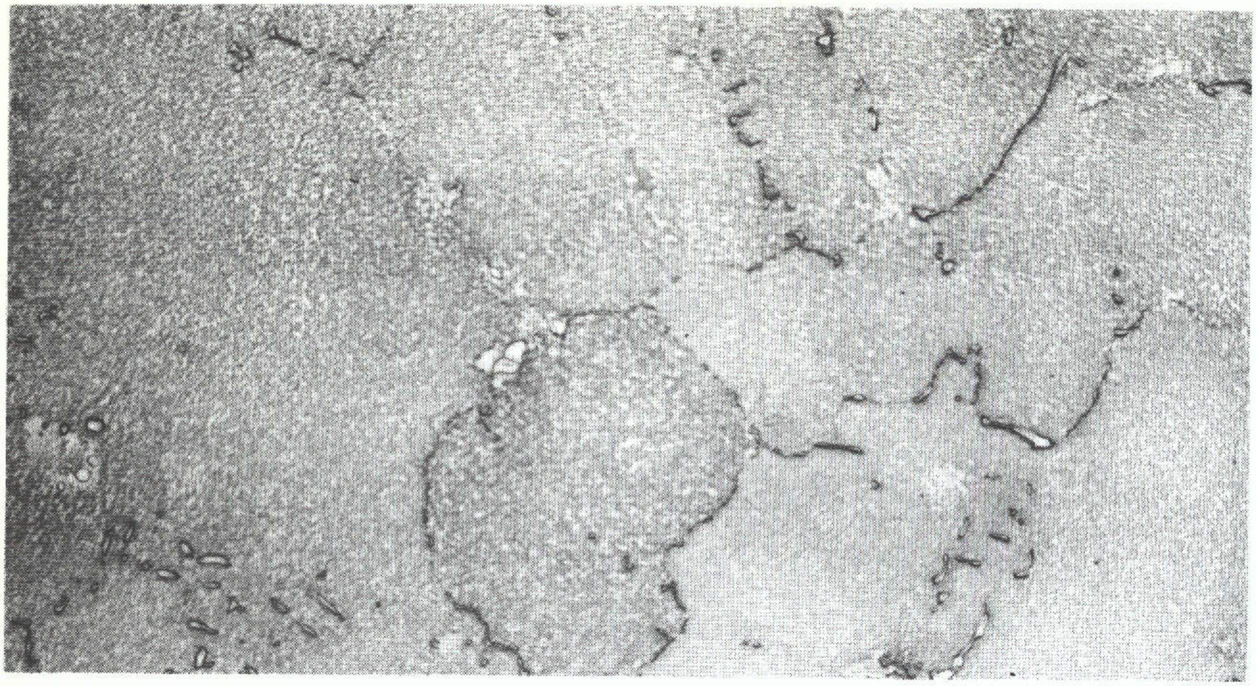

(a) X500

Untested transverse section from uniaxial specimen

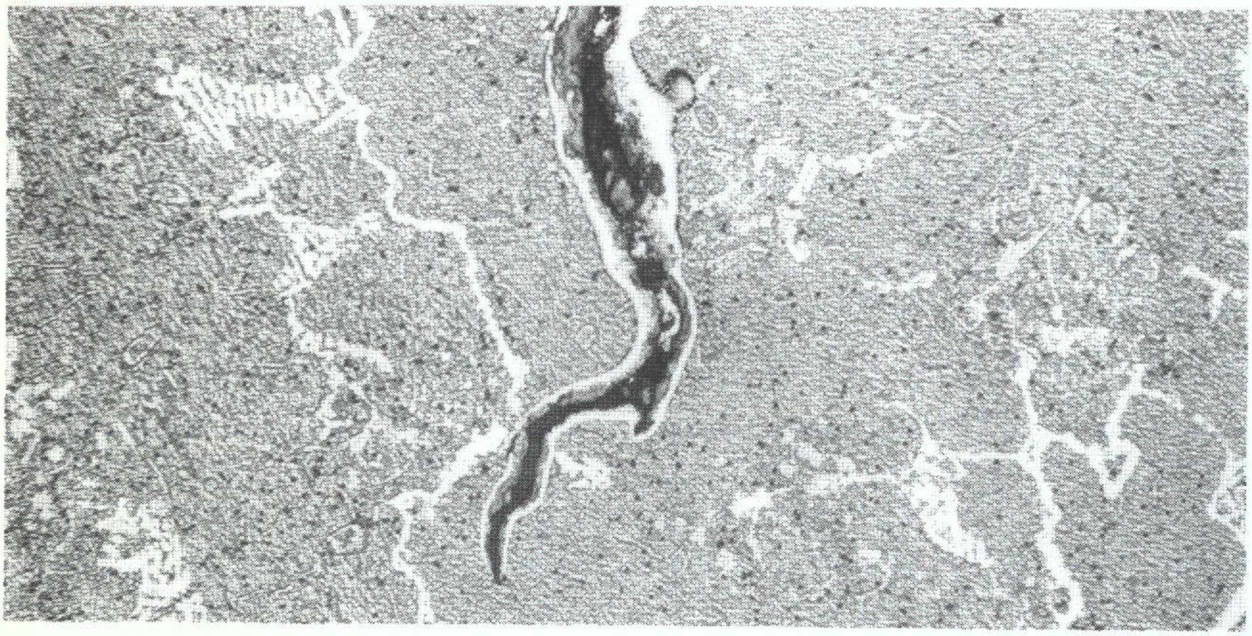

(b) X500

Longitudinal section from thermal fatigue specimen tested at 1990/600°F for 500 cycles

Figure 1

Microstructure of B1900 Specimens (Kalling's etch)

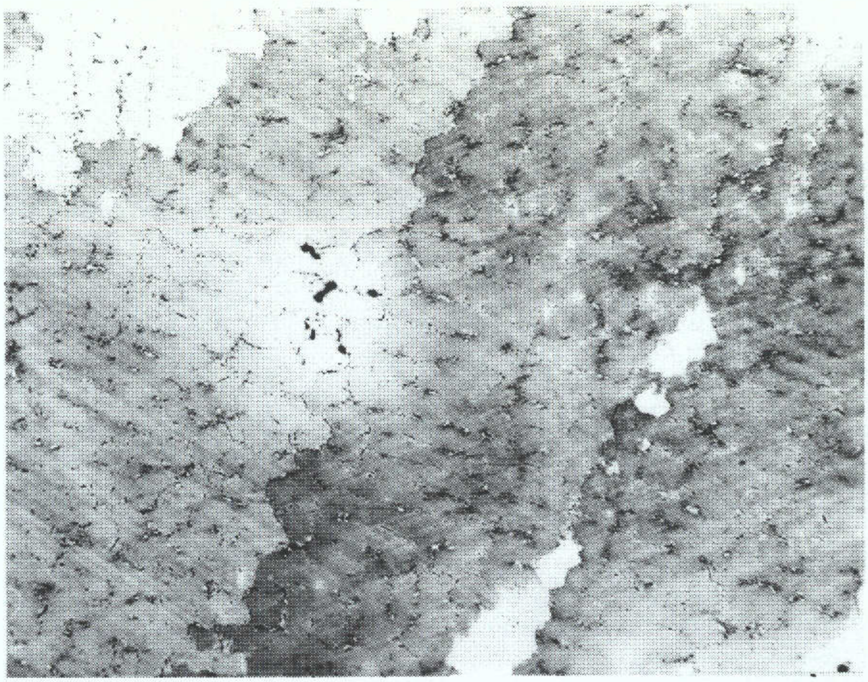

(c) X100

Longitudinal section from stress-rupture bar.
Tested for 100 hr at 1800°F.

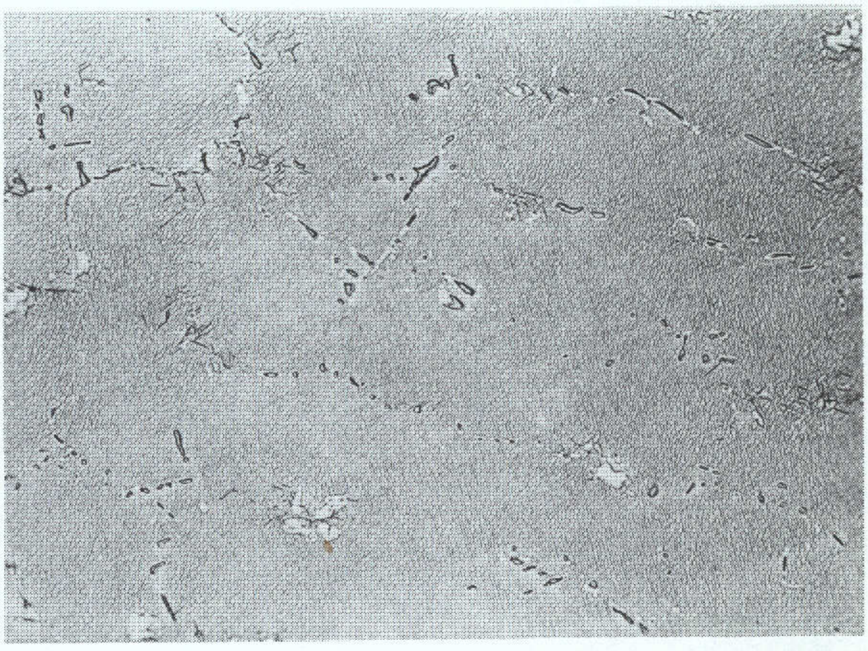

(d) X500

As (c)

Figure 1 (cont.)

Microstructure of B1900 Specimens

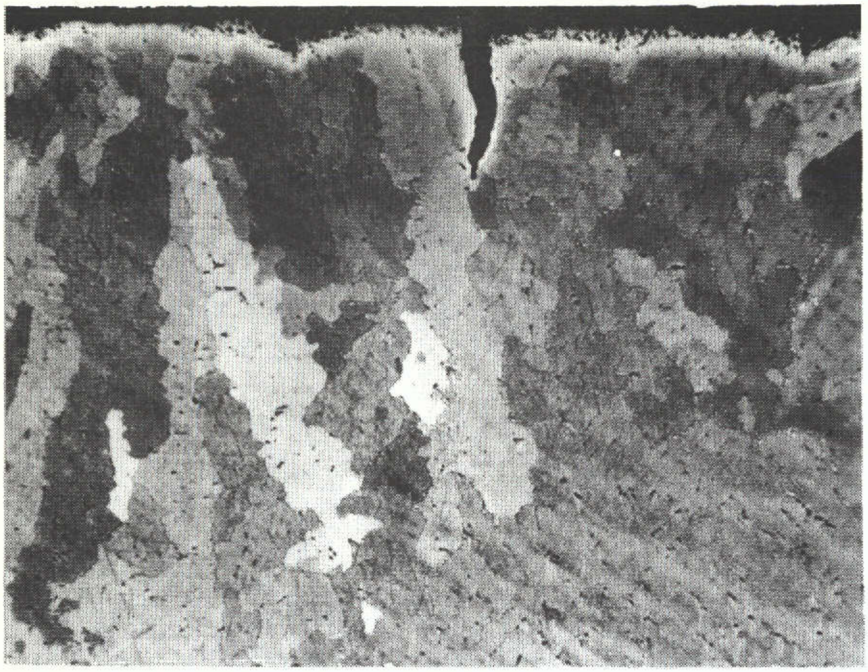

(e) X100

Longitudinal section tested at 1915/525°F for 600 cycles

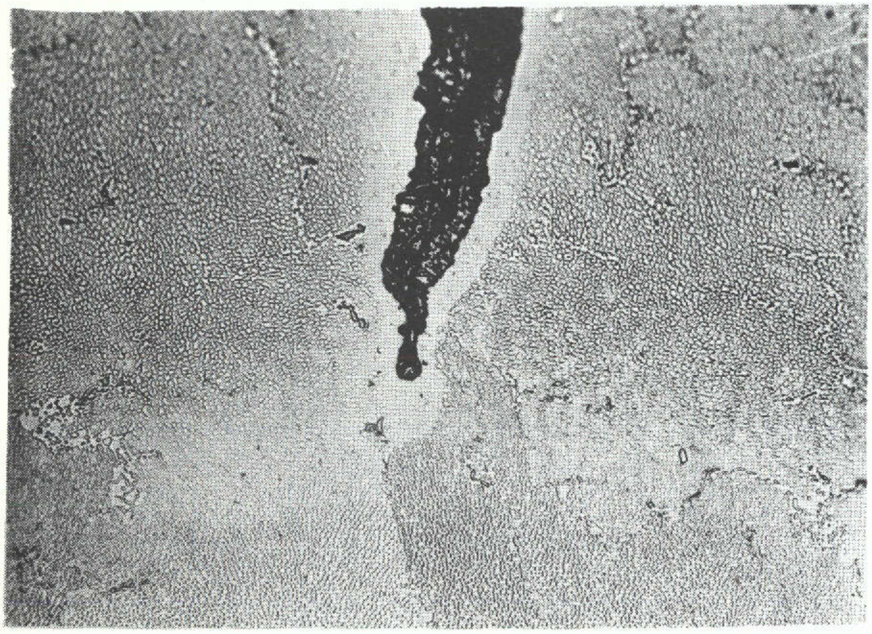

(f) X500

As (e)

Figure 1 (cont.)
Microstructure of B1900 Specimens

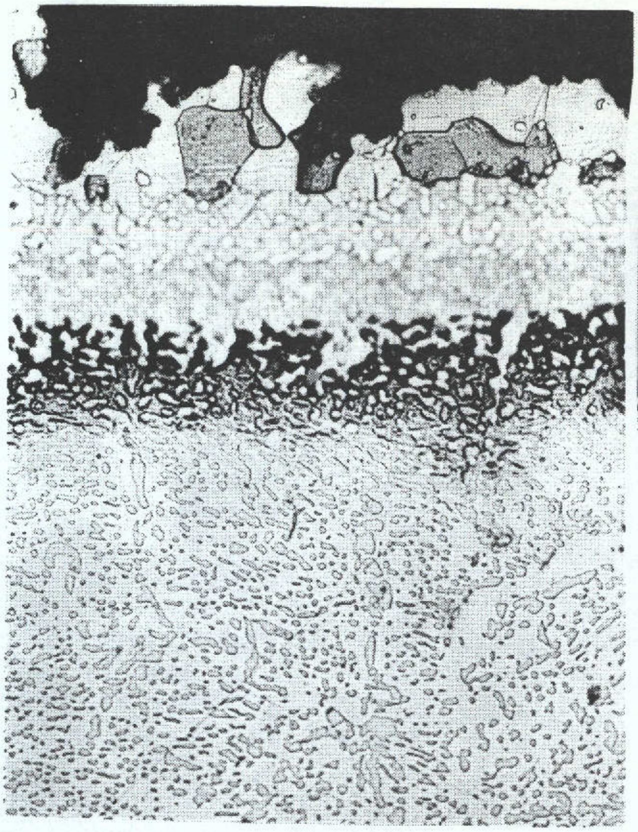

(g) X500
B1900 + Jocoat, transverse section tested at 2065/675°F for 1700 cycles

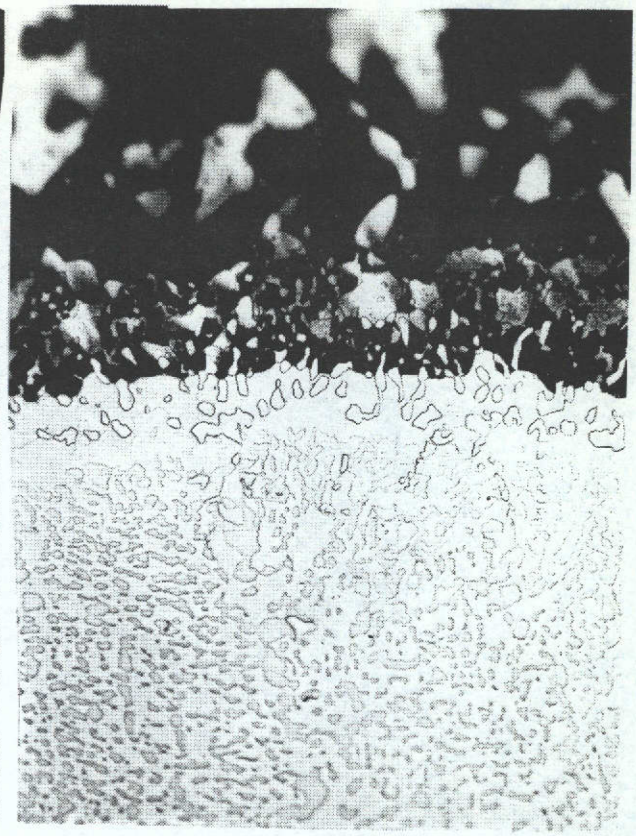

(h) X500
As (g), longitudinal section

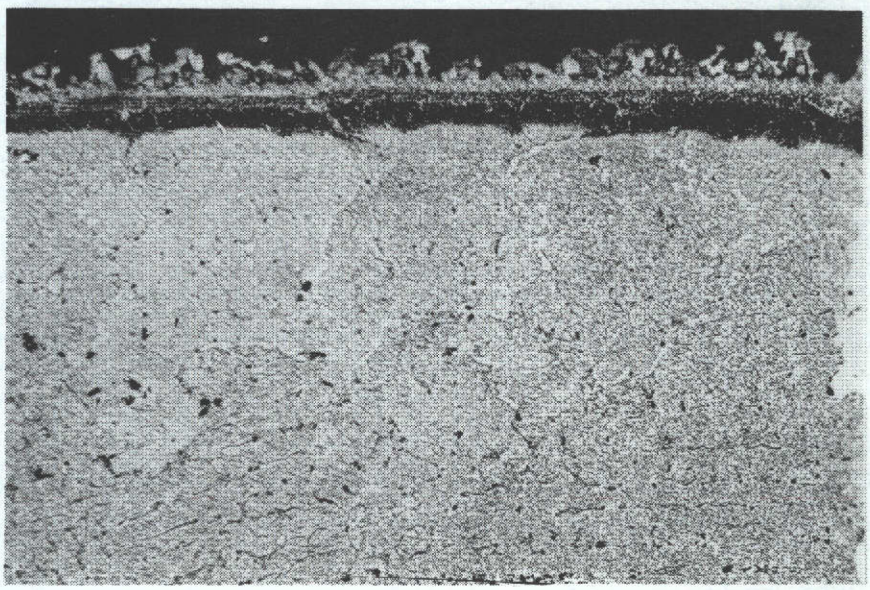

(i) X100
As (g)

Figure 1 (cont.)

Microstructure of B1900 Specimens

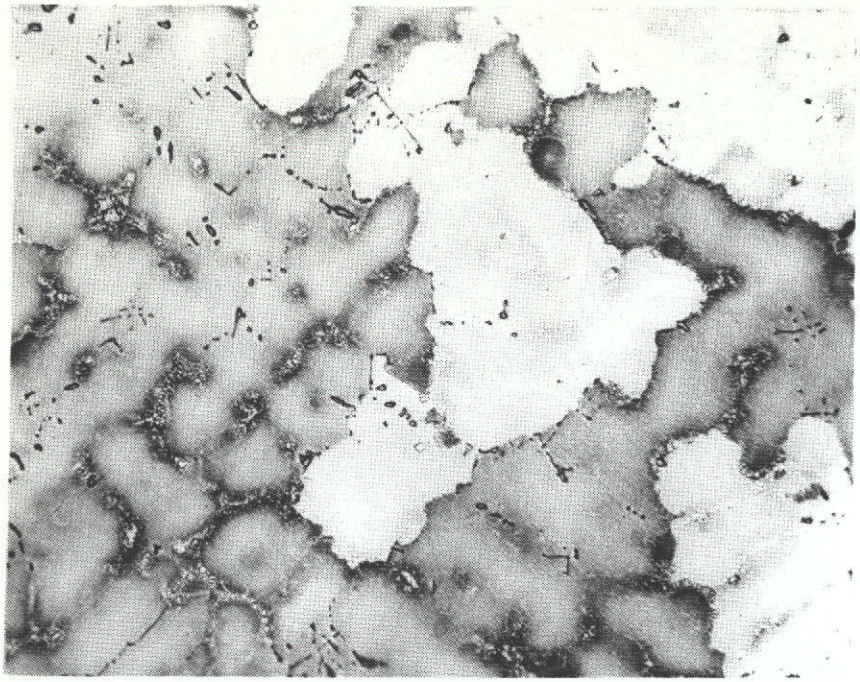

(a) X100

Untested transverse structure

(b) X500

Untested transverse structure

Figure 2

Microstructure of B1900 DID + Jocoat Specimens
(Kalling's etch)

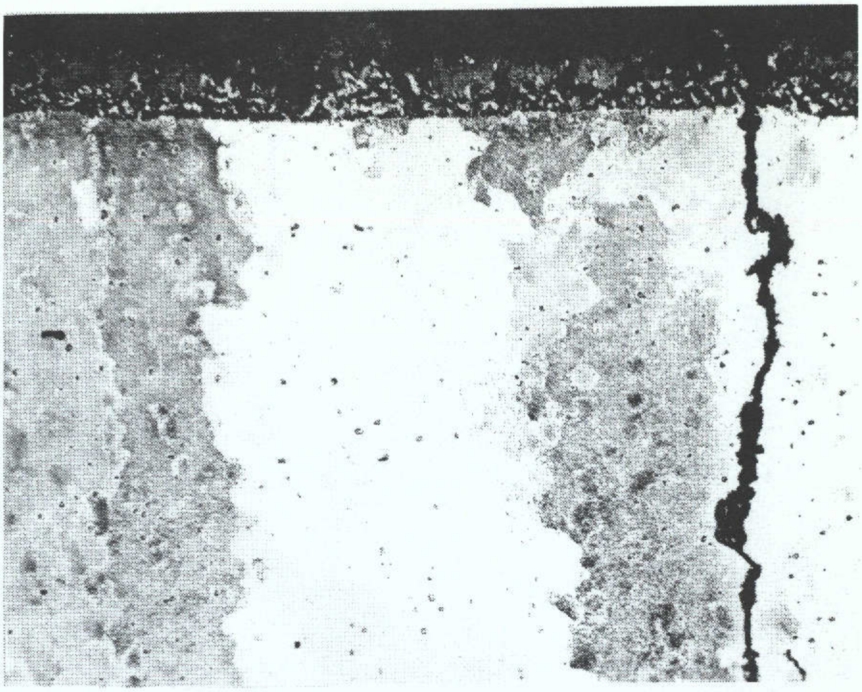

(c) X100

Longitudinal section tested at 1990/600°F for 3250 cycles

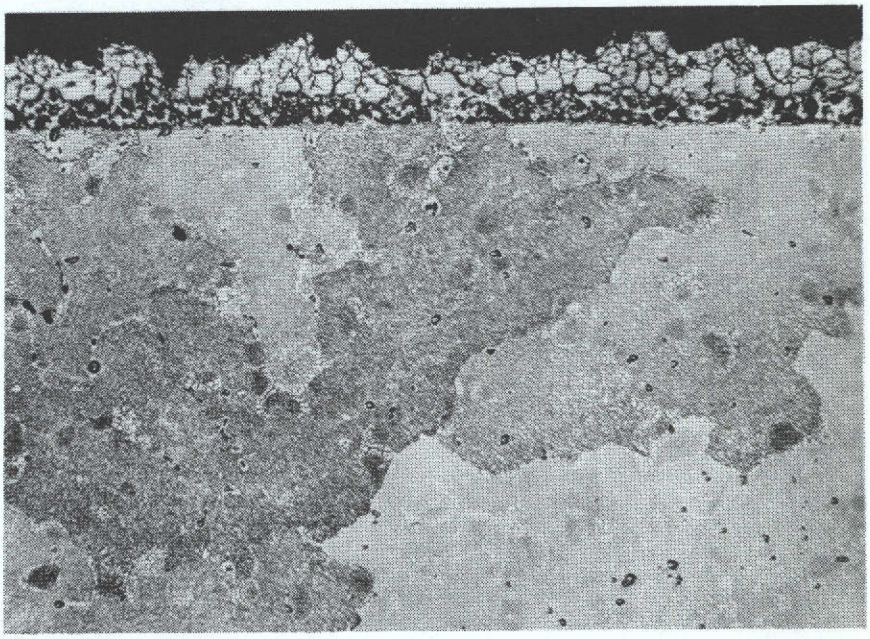

(d) X100

Transverse section tested at 2065/675°F for 2300 cycles

Figure 2 (cont.)
Microstructure of B1900 DID + Jocoat Specimens

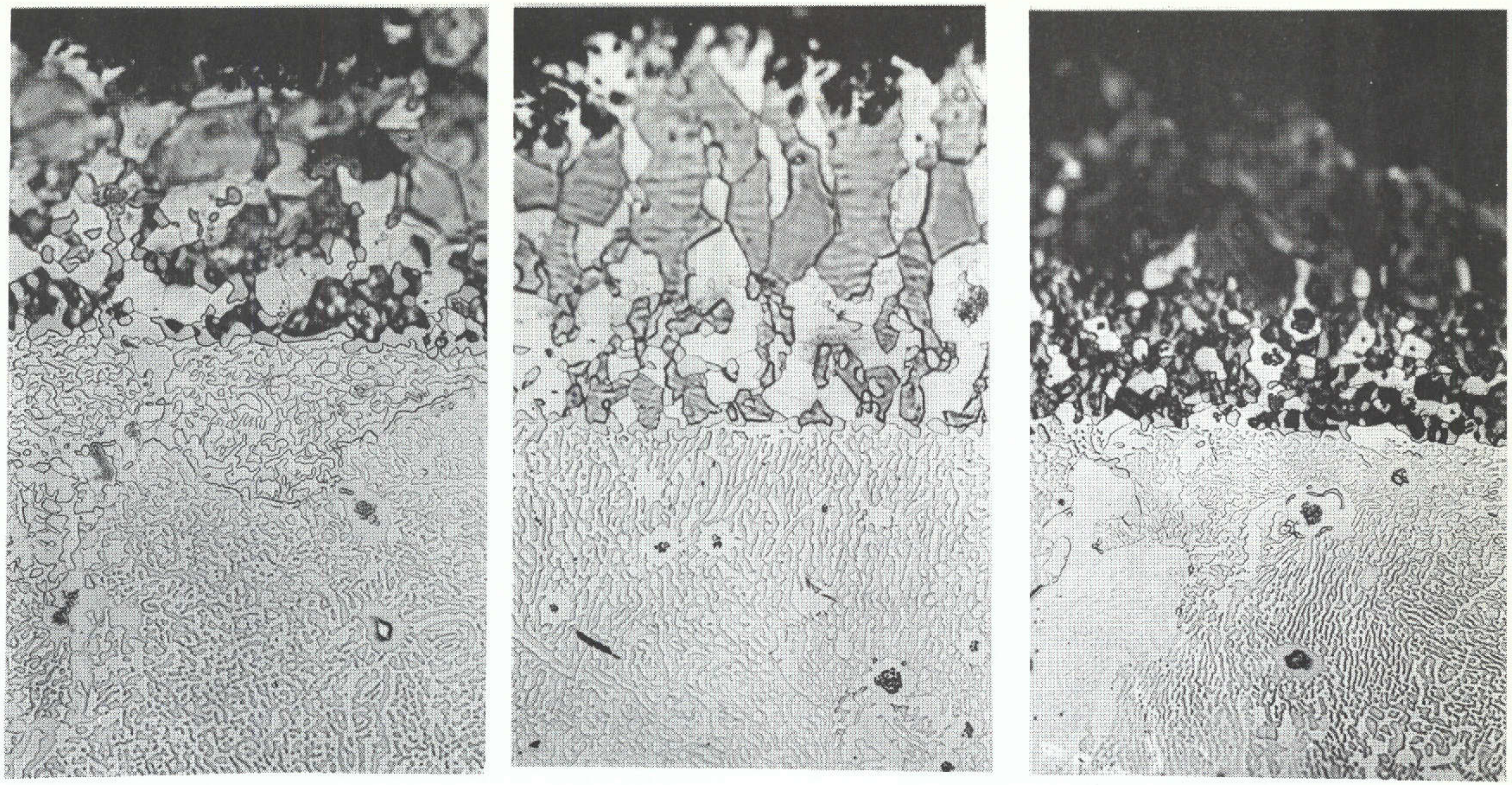

(e) X500

Longitudinal section tested at 1990/600°F, 3250 cycles

(f) X500

Longitudinal section tested at 2065/675°F, 2300 cycles

(g) X500

As (f), transverse section

Figure 2 (cont.)

Microstructure of B1900 DID + Jocoat Specimens

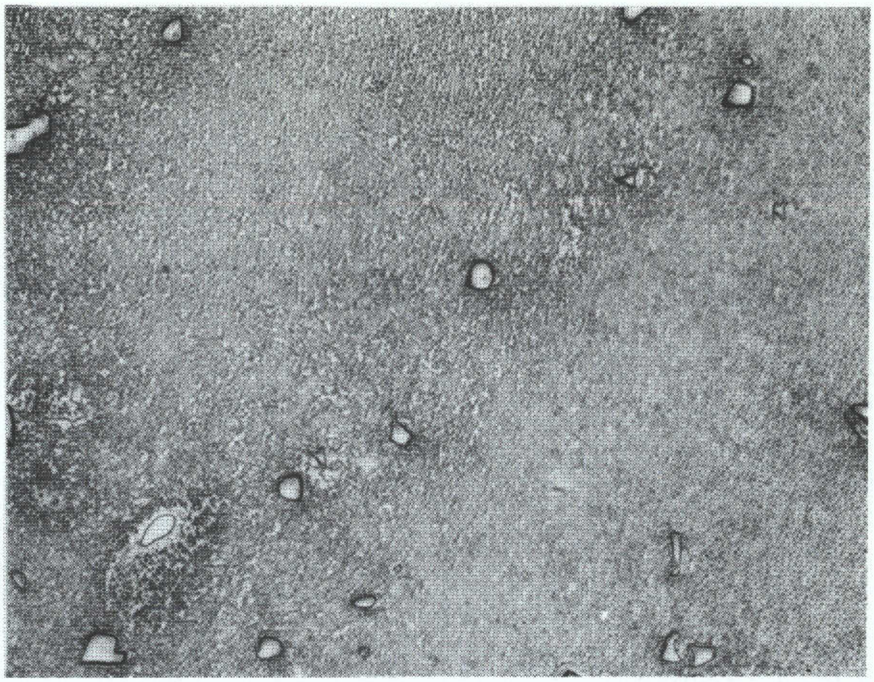

(a) X500

Untested transverse section from uniaxial specimen

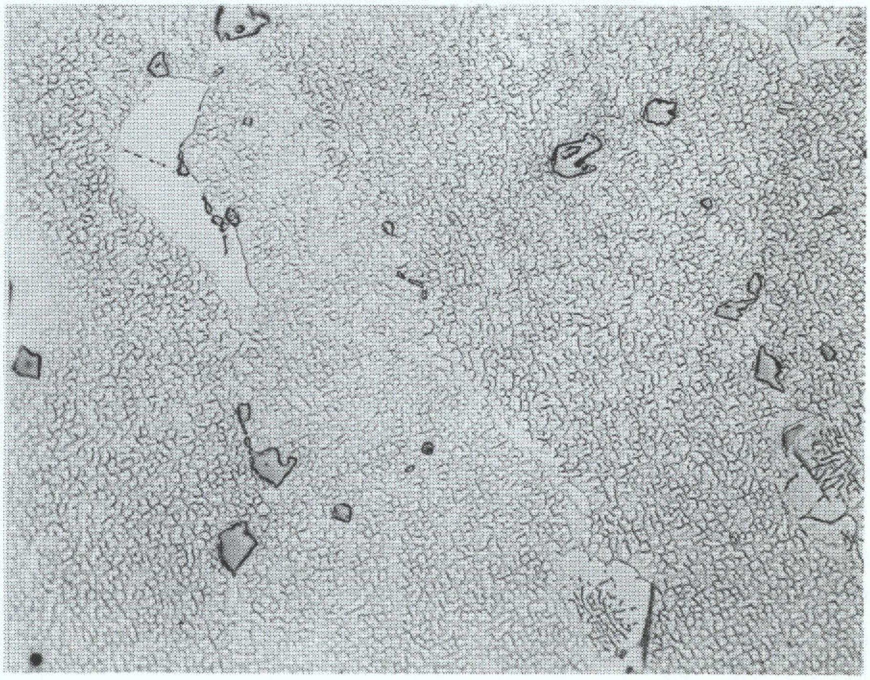

(b) X500

Longitudinal section tested at 2065/675°F for 200 cycles

Figure 3

Microstructure of IN-100 Specimens (Kalling's etch)

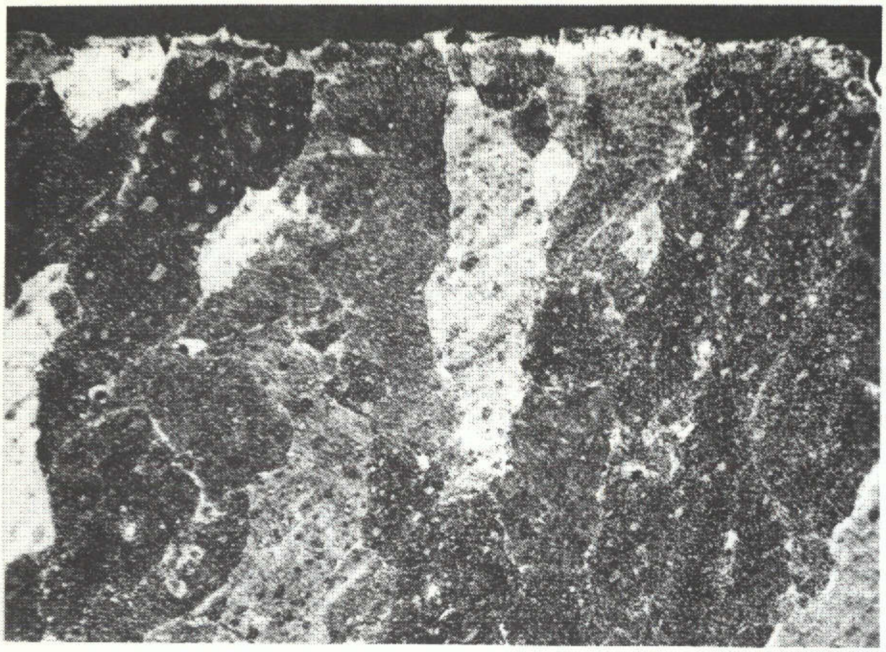

(c) X100

Longitudinal section tested at 1915/525°F for 200 cycles

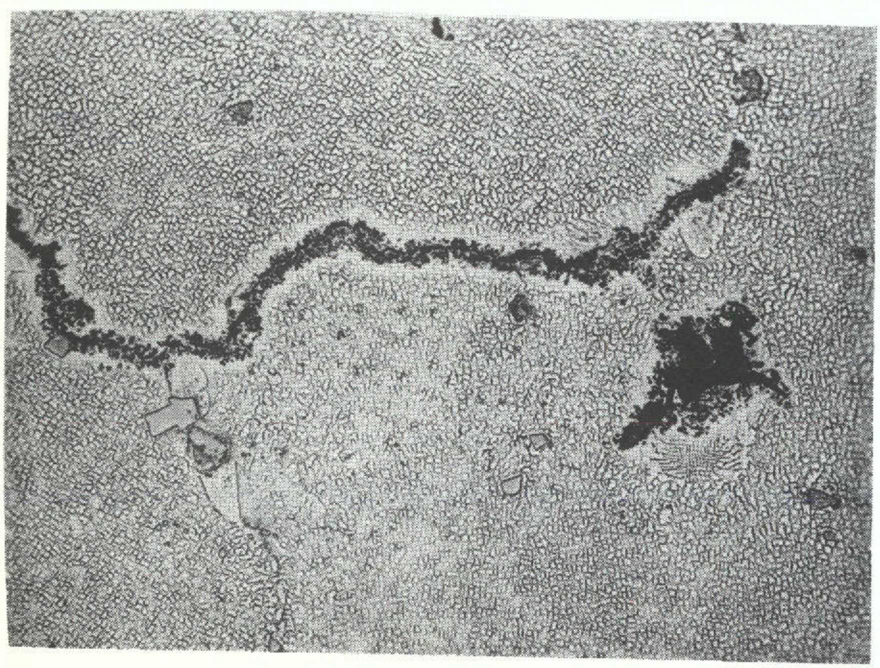

(d) X500

As (c), showing possible crack formation

Figure 3 (cont.)

Microstructure of IN-100 Specimens

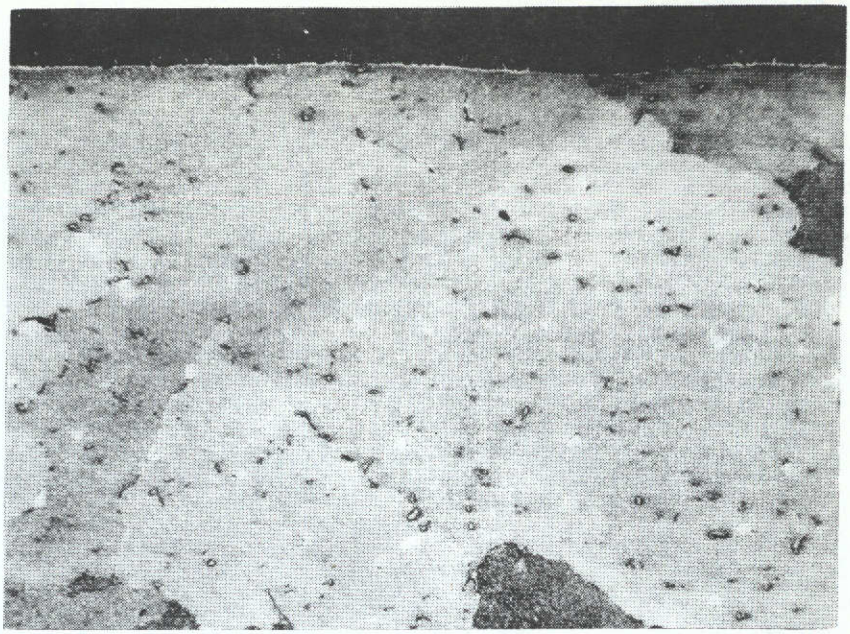

(e) X100

IN-100 + Jocoat, transverse section tested at 2065/675°F for 200 cycles

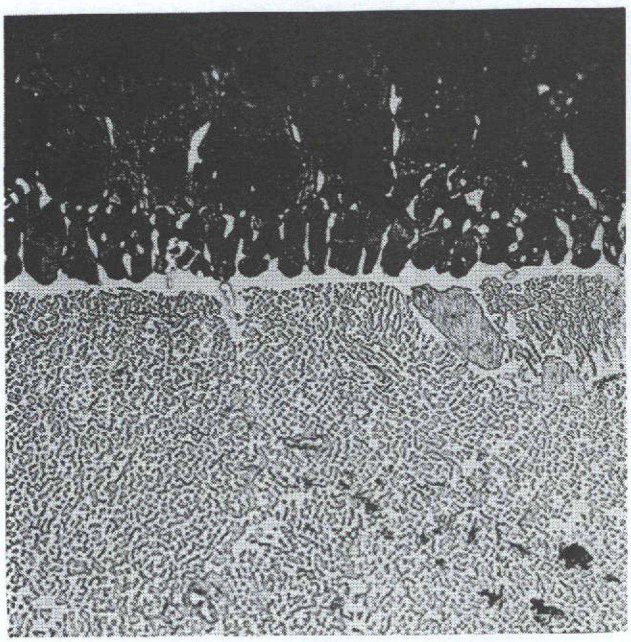

(f) X500

As (e), longitudinal section

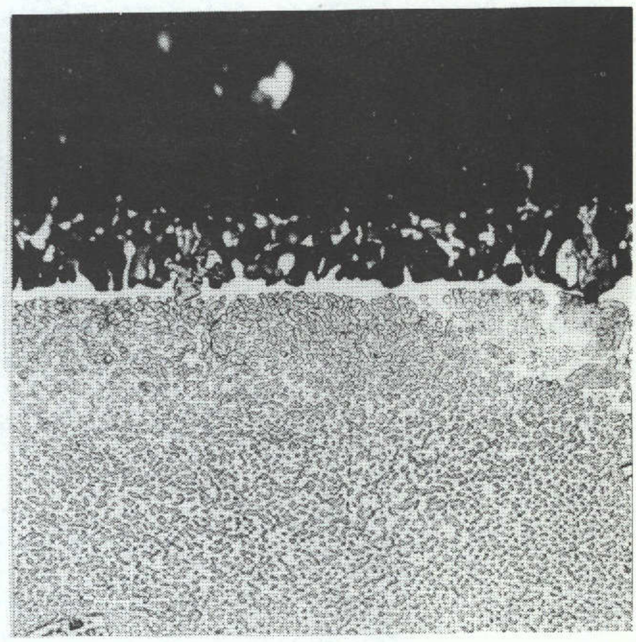

(g) X500

As (e)

Figure 3 (cont.)

Microstructure of IN-100 Specimens

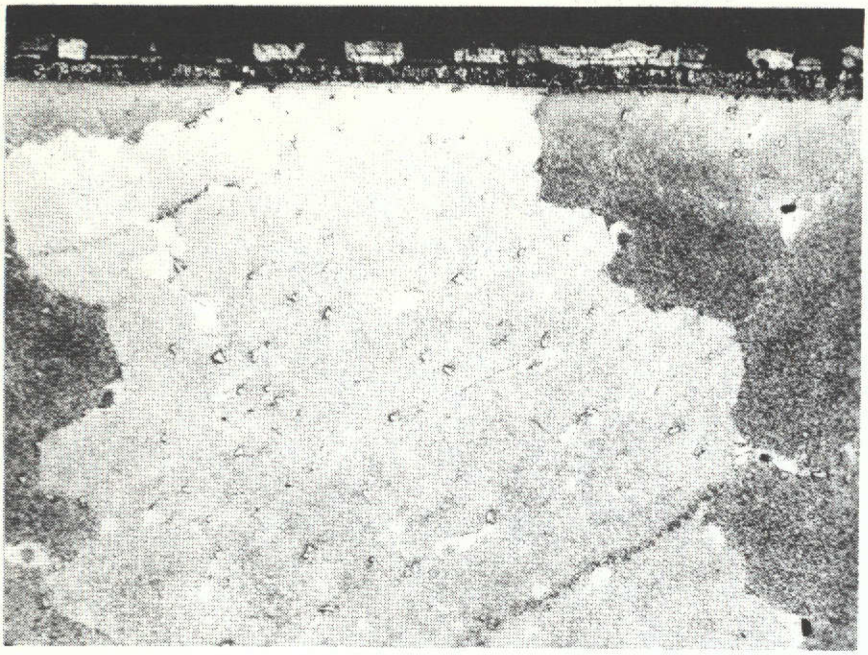

(h) X100

IN-100 + Xcoat A, transverse section tested at 2065/675°F for 200 cycles

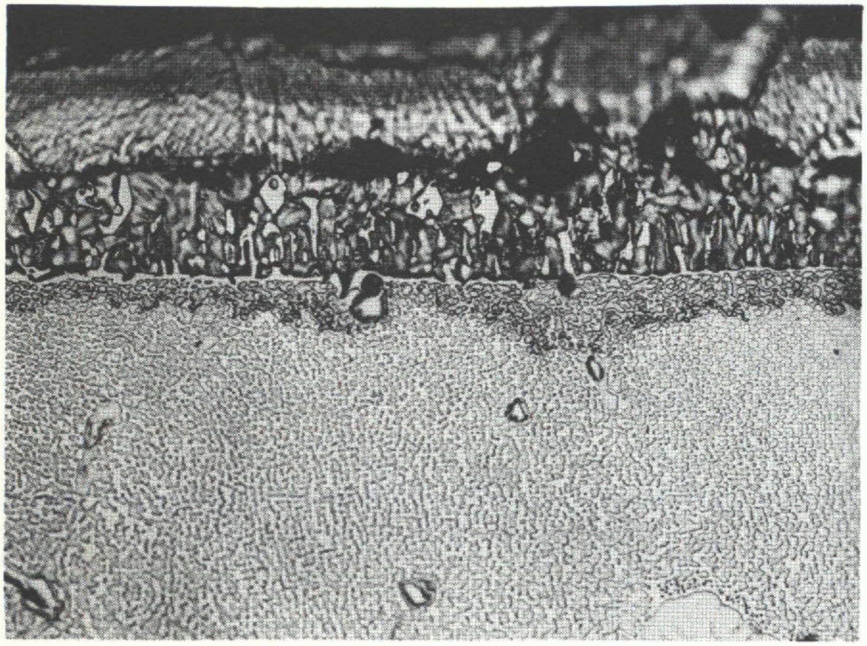

(i) X500

As (h)

Figure 3 (cont.)

Microstructure of IN-100 Specimens

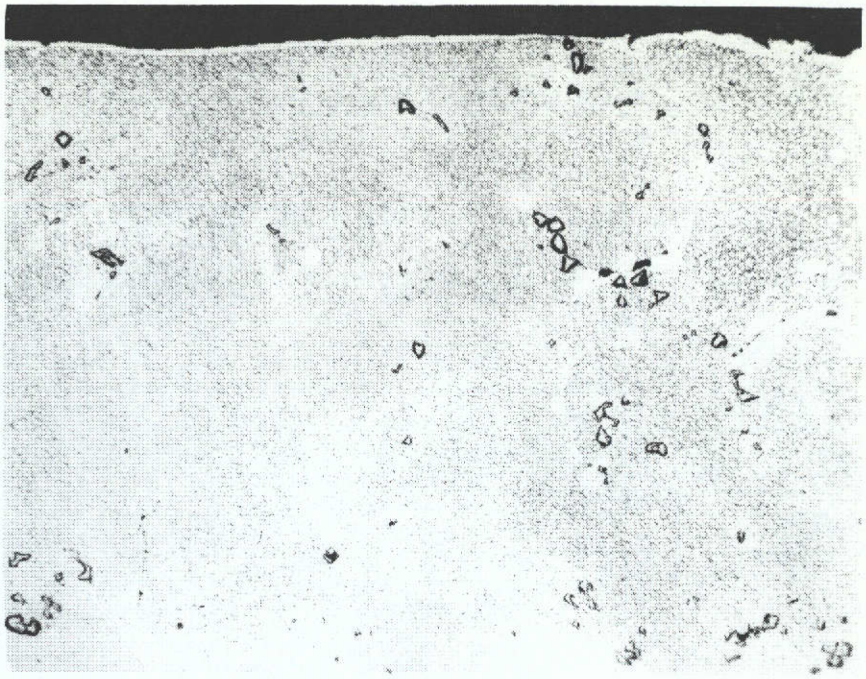

(a) X100

Transverse section tested at 2065/675°F for 2900 cycles

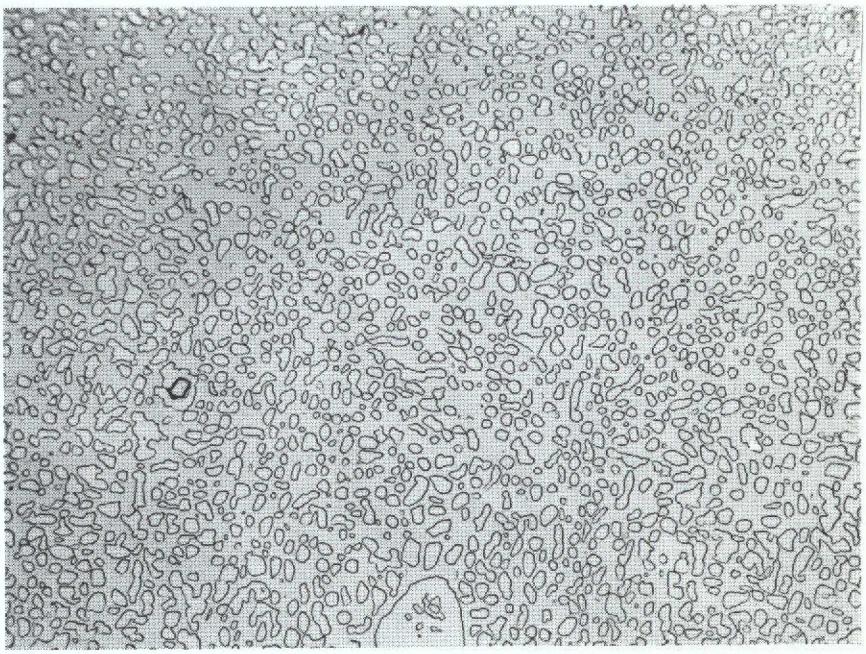

(b) X500

As (a)

Figure 4

Microstructure of IN-100 Directionally Solidified (Kalling's etch)

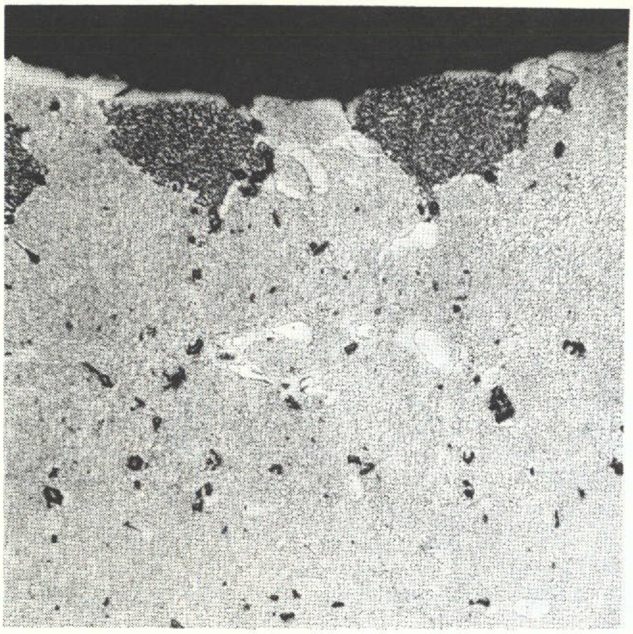

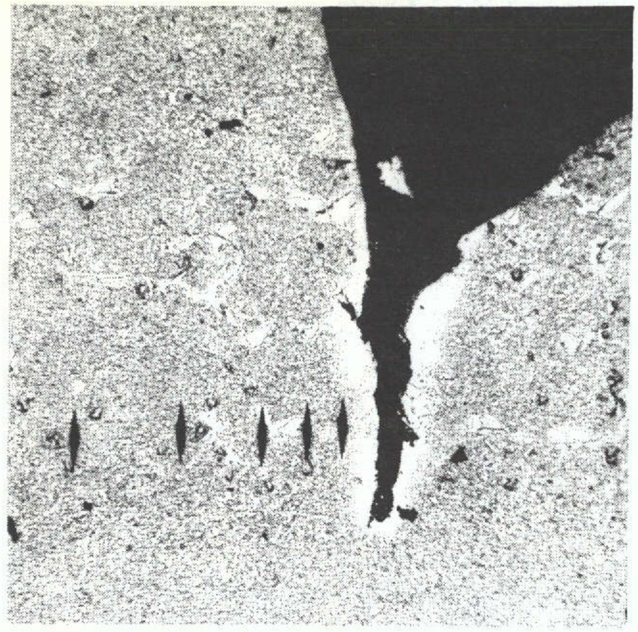

(c) X100
Longitudinal section tested at 2065/675°F for 2900 cycles

(d) X100
As (c); note hardness impressions from side of crack tip

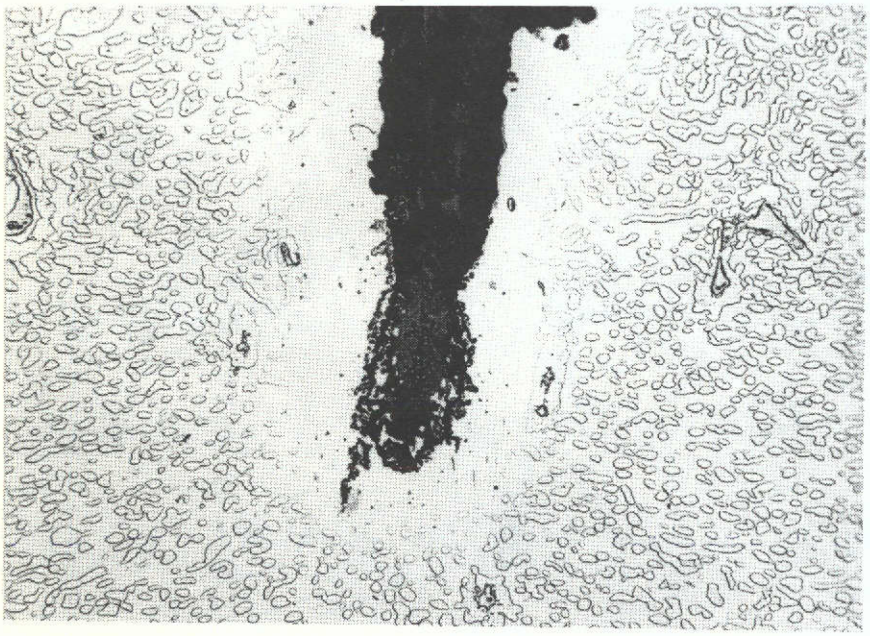

(e) X500
As (d), showing tip of crack

Figure 4 (cont.)

Microstructure of IN-100 Directionally Solidified

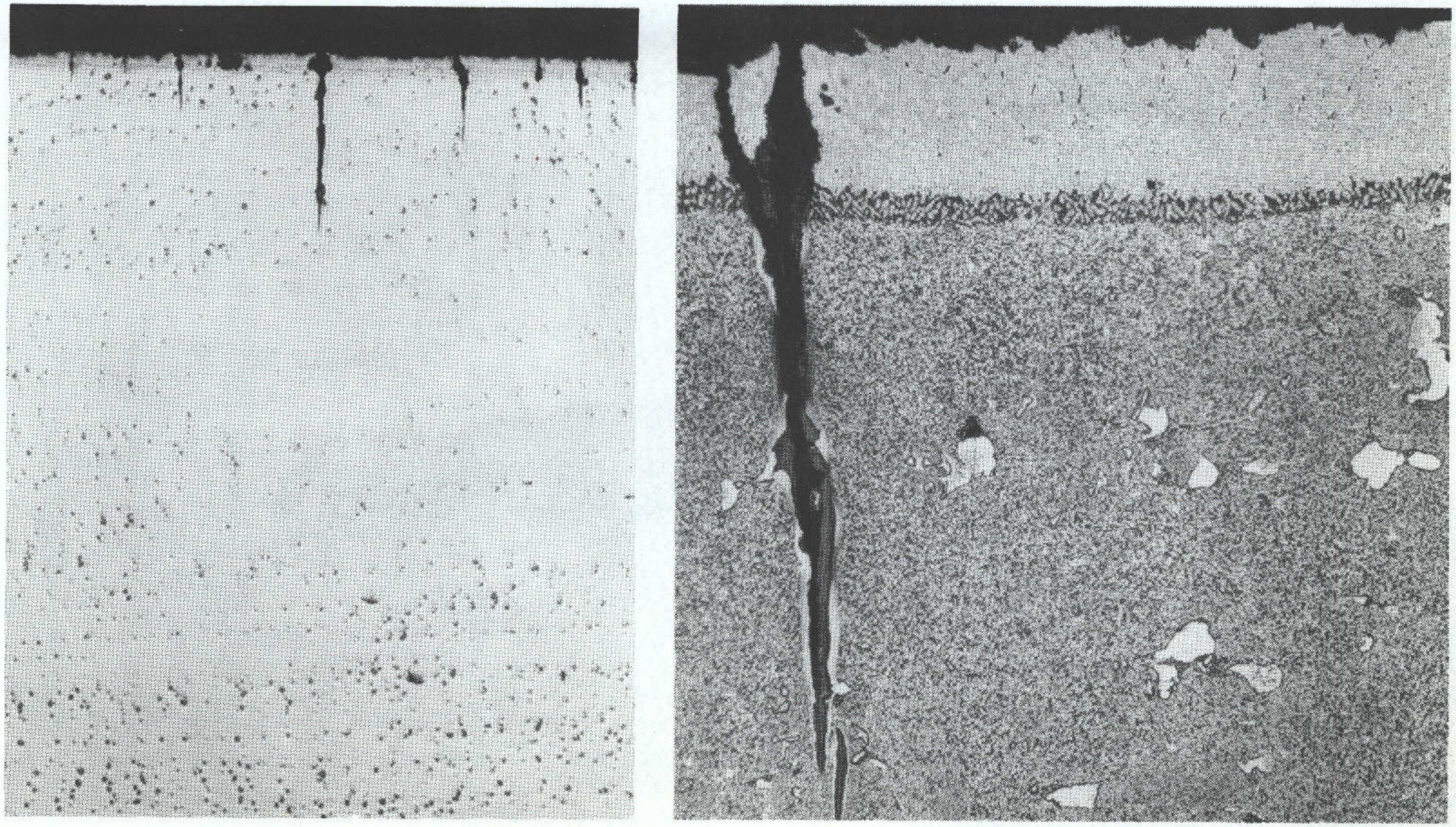

(a) Unetched, X20
Longitudinal section tested at
1990/600°F for 5000 cycles

(b) X125
As (a)

Figure 5

Microstructure of IN-100 Directionally Solidified + Jocoat (Kalling's etch)

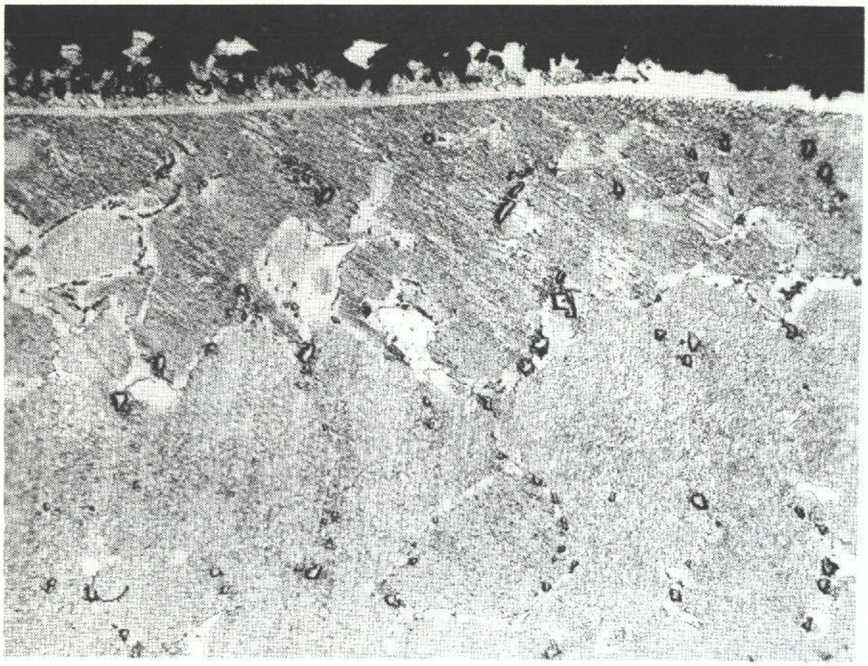

(c) X100

Longitudinal section tested at 2065/675°F for 2200 cycles

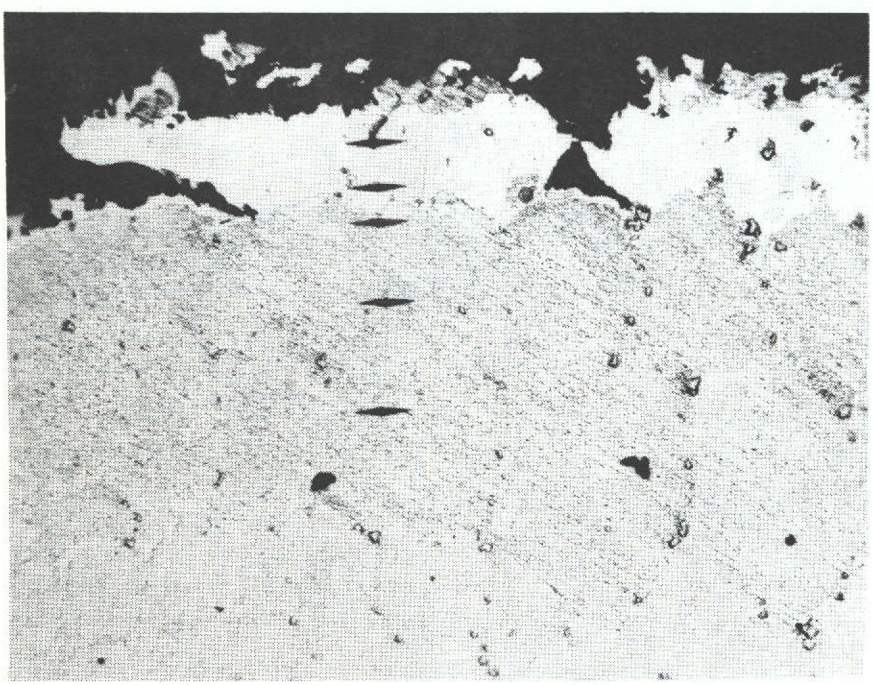

(d) X100

As (c); note the hardness impressions

Figure 5 (cont.)

Microstructure of IN-100 Directionally Solidified + Jocoat

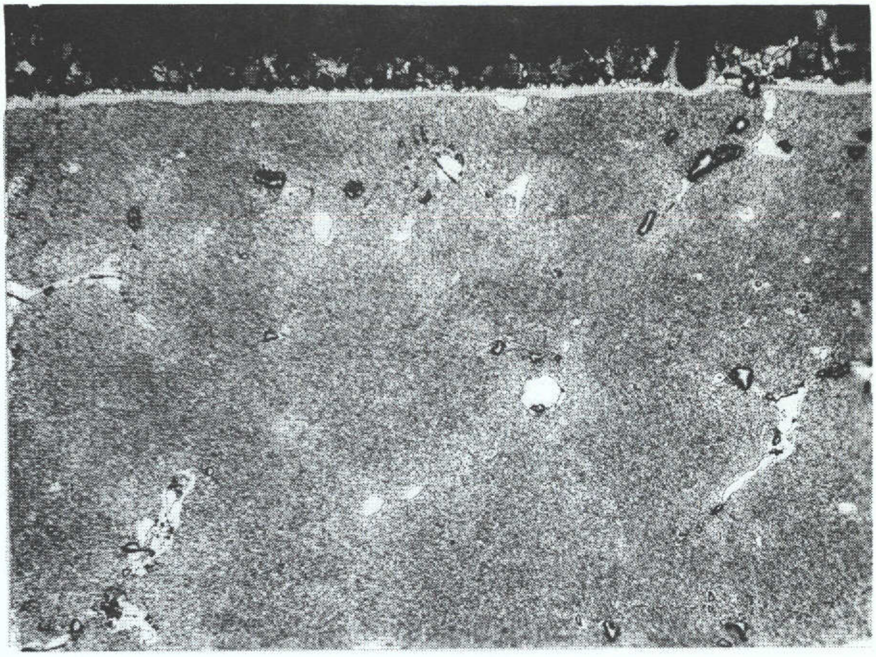

(e) X100

Transverse section tested at 2065/675°F for 2200 cycles

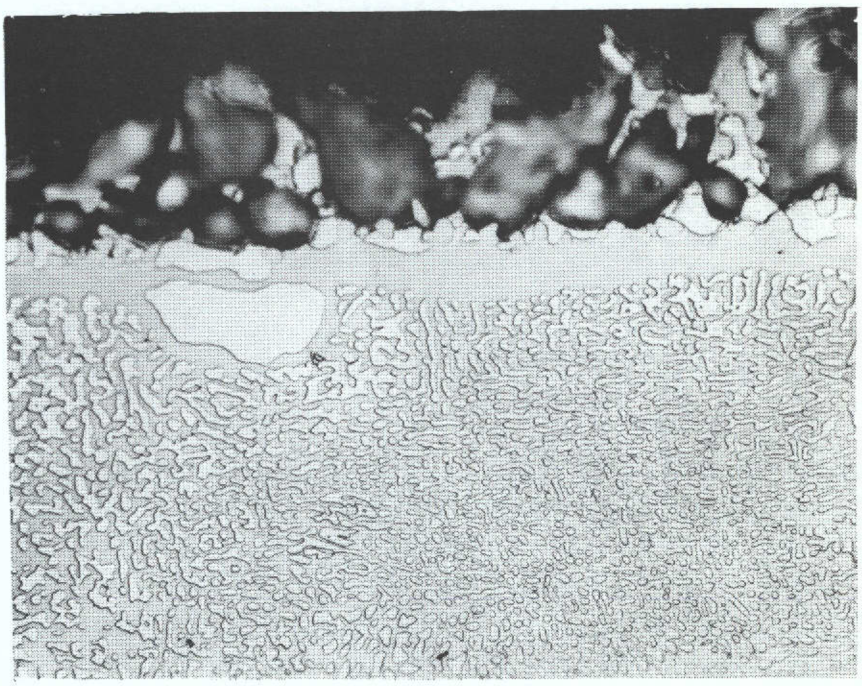

(f) X500

As (e)

Figure 5 (cont.)

Microstructure of IN-100 Directionally Solidified + Jocoat

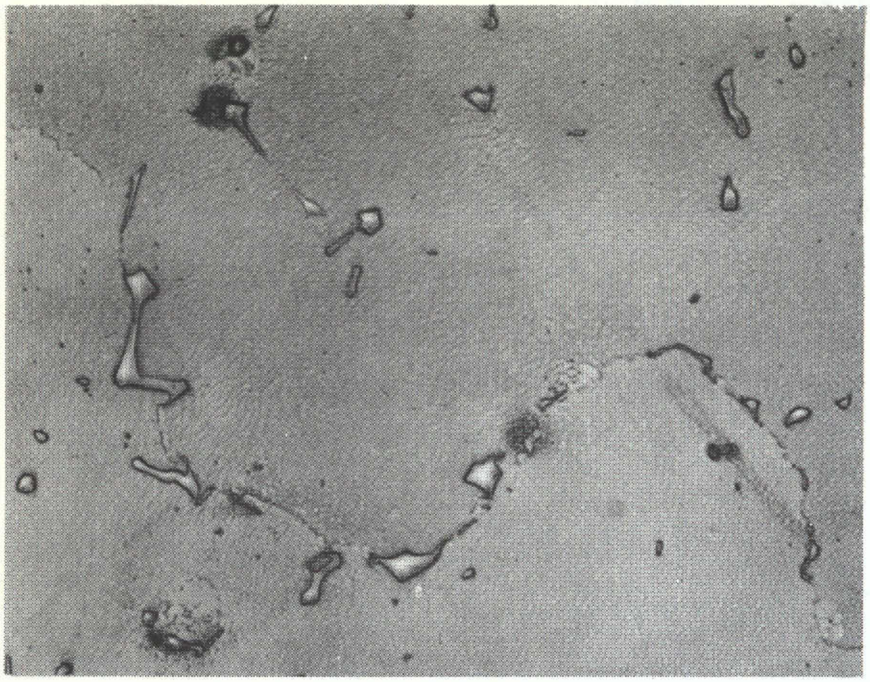

(a) X500
Untested transverse section from uniaxial specimen

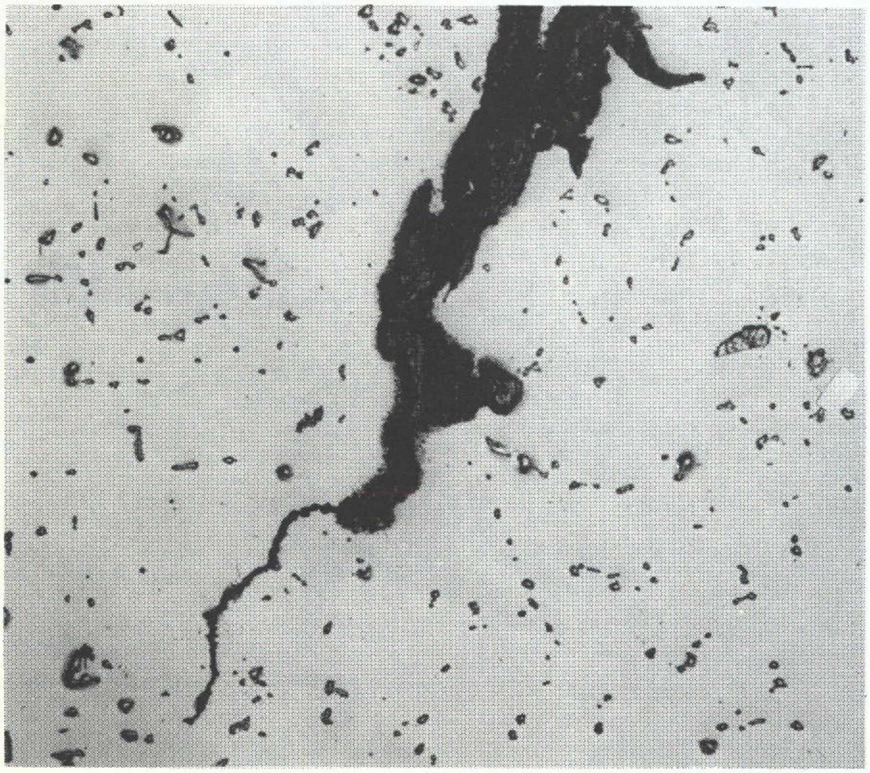

(b) Unetched, X125
Longitudinal section tested at 1990/600°F for 500 cycles. Note the crack formation.

Figure 6

Microstructure of MAR-M 200 Specimens (Kalling's etch)

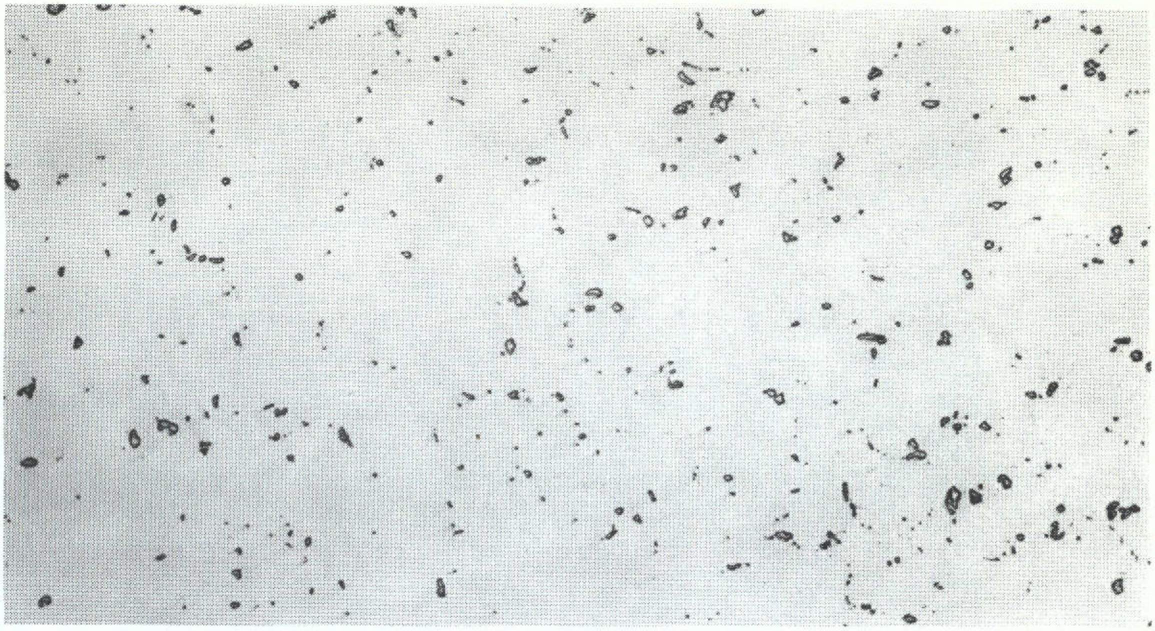

(a) Unetched, X125
Untested transverse section from uniaxial specimen

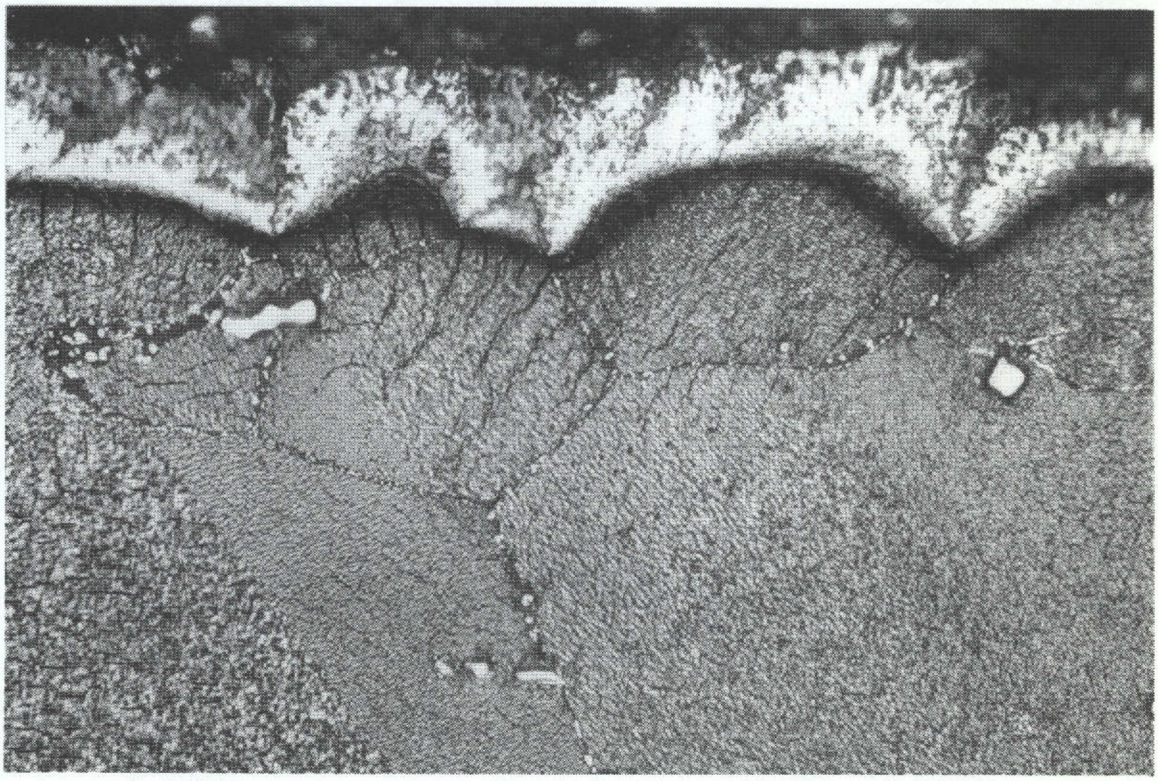

(b) X500
Longitudinal section tested at 1990/600°F for 500 cycles

Figure 7

Microstructure of Udimet 700 Wrought Specimens
(Kalling's etch)

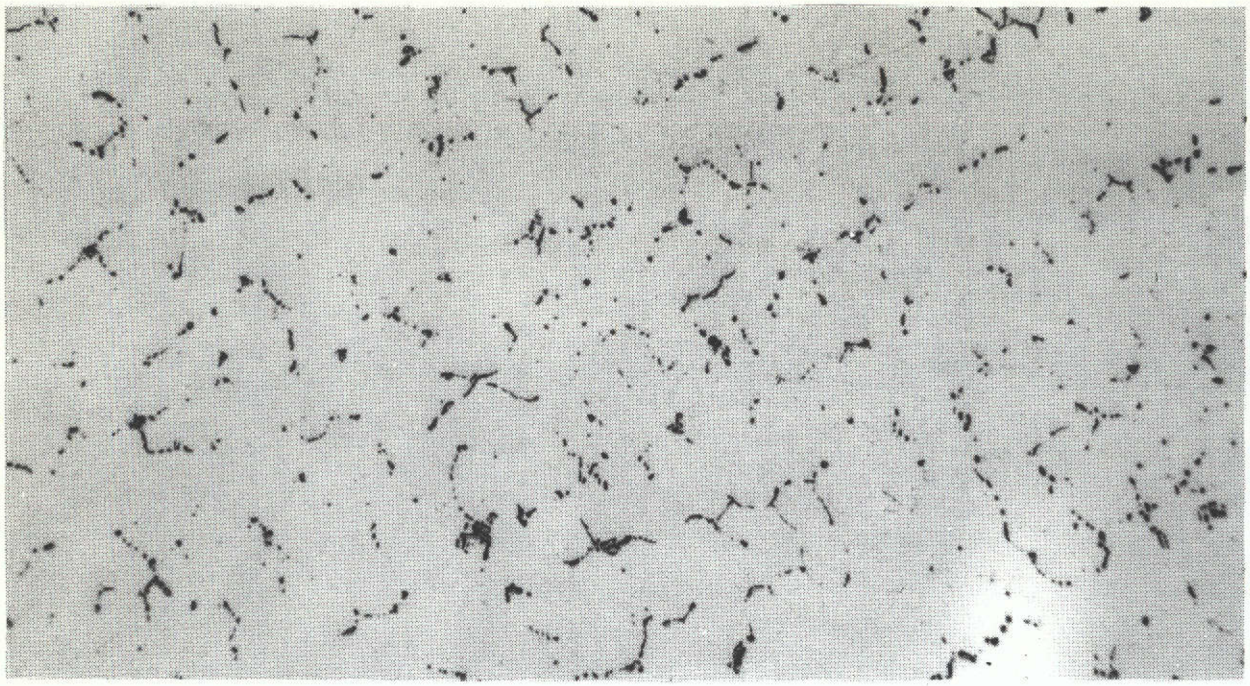

(a) Unetched, X125
Untested transverse section from uniaxial specimen

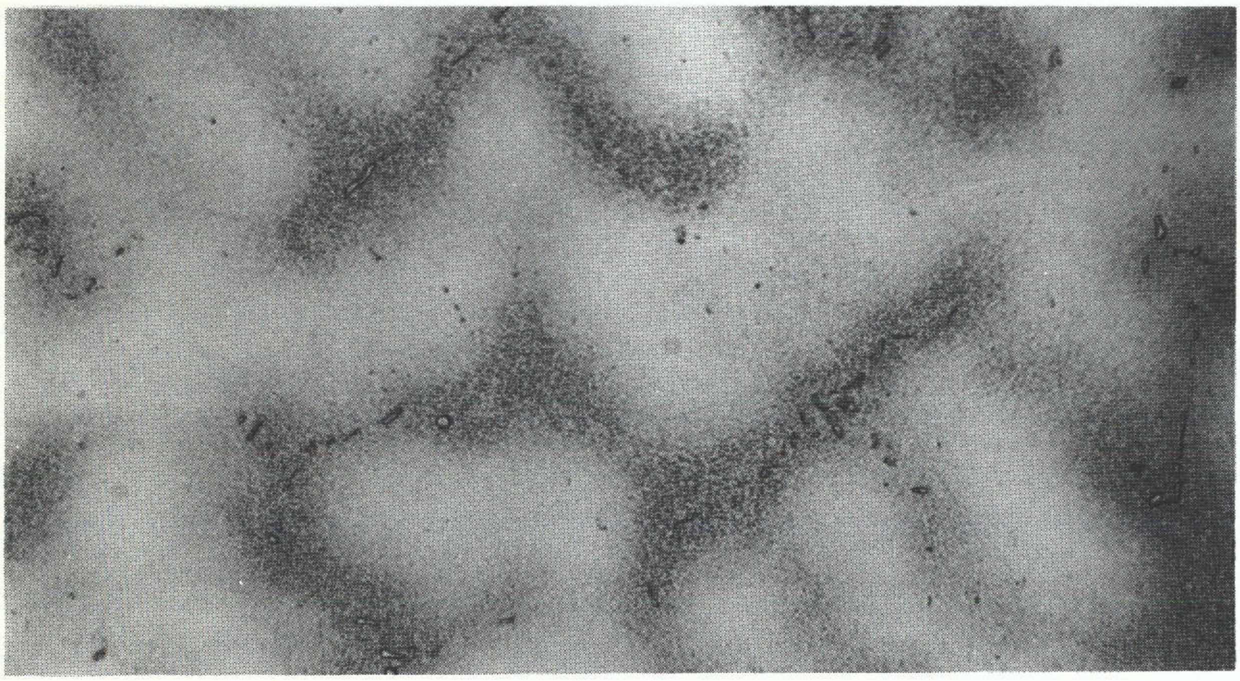

(b) X500
As (a)

Figure 8

Microstructure of Udimet 700 Cast Specimens (Kalling's etch)

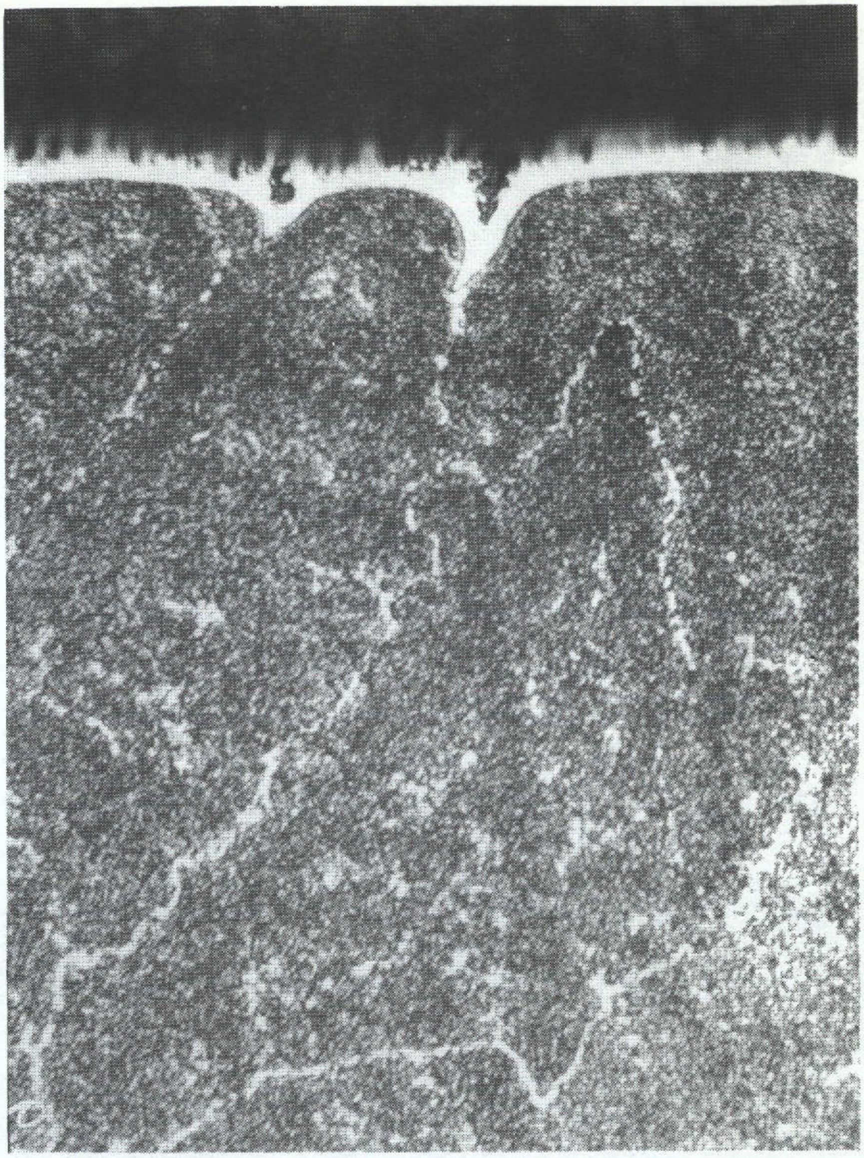

(c) X500
Longitudinal section tested at 1990/600°F for 700 cycles showing initial stages of crack formation.

Figure 8 (cont.)

Microstructure of Udimet 700 Cast Specimens

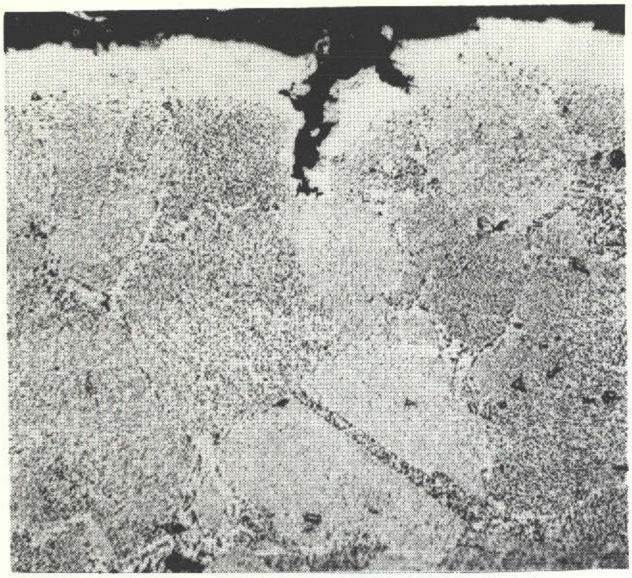

(a) X100
Longitudinal section tested at 2065/675°F for 1300 cycles

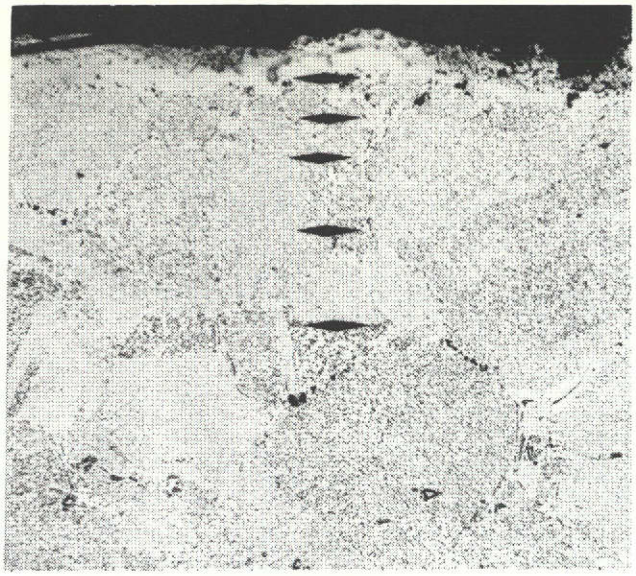

(b) X100
As (a); note the hardness impressions

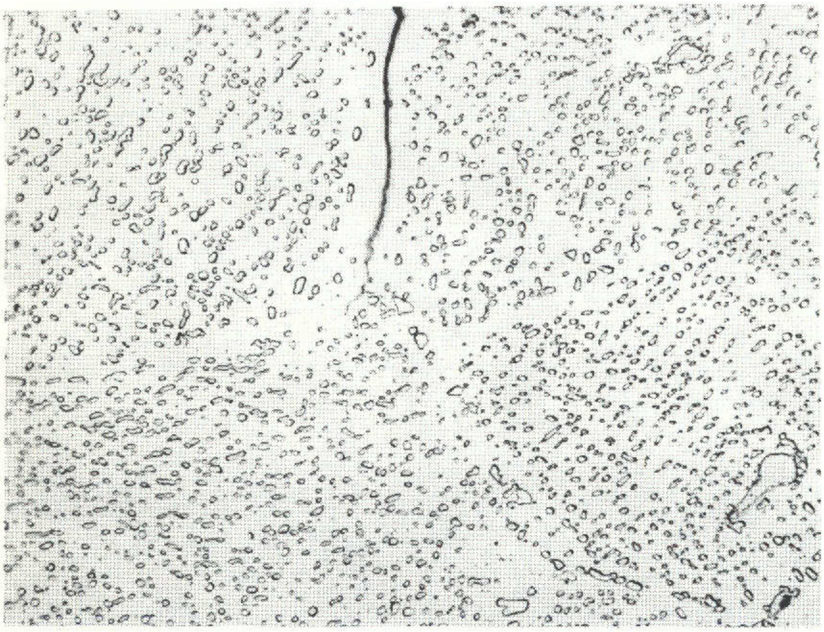

(c) X500
As (a), showing progress of a crack tip

Figure 9

Microstructure of Udimet 700 (SEW) Clad + Xcoat B (Kalling's etch)

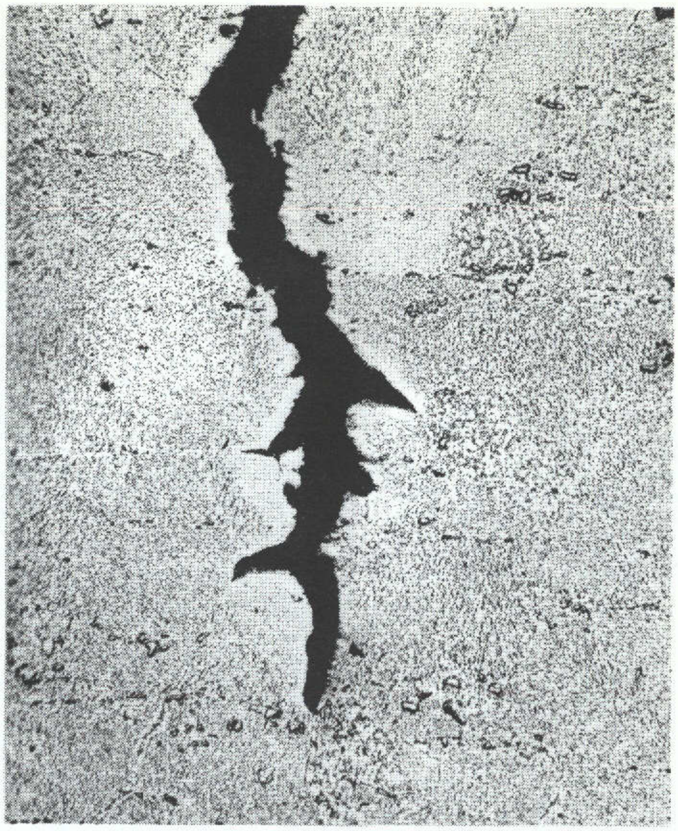

(d) X100
As (a)

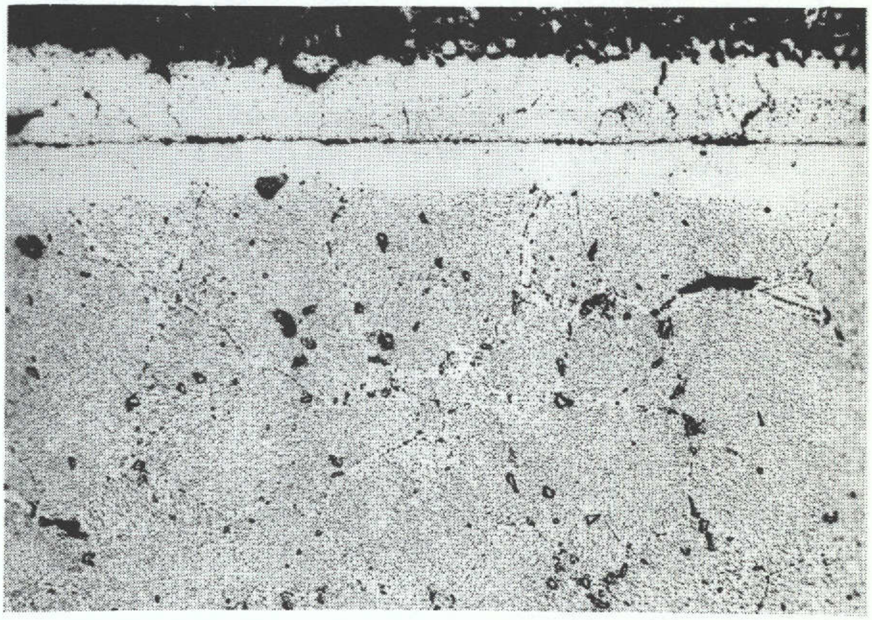

(e) X100
As (a), transverse section through coating

Figure 9 (cont.)
Microstructure of Udimet 700 (SEW) Clad + Xcoat B

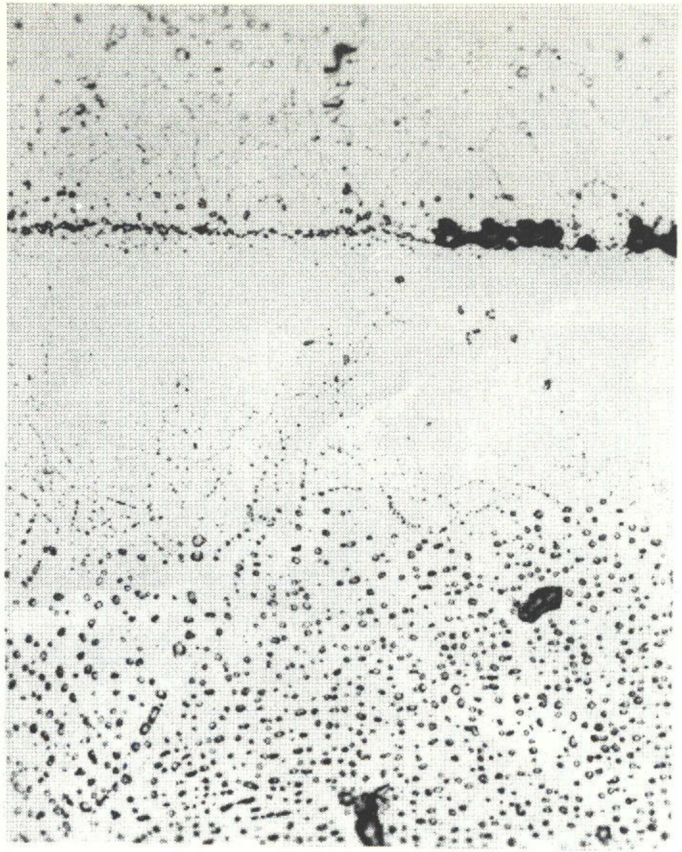

(f) X500
As (e)

(g) X500
As (e)

Figure 9 (cont.)

Microstructure of Udimet 700 (SEW) Clad + Xcoat B

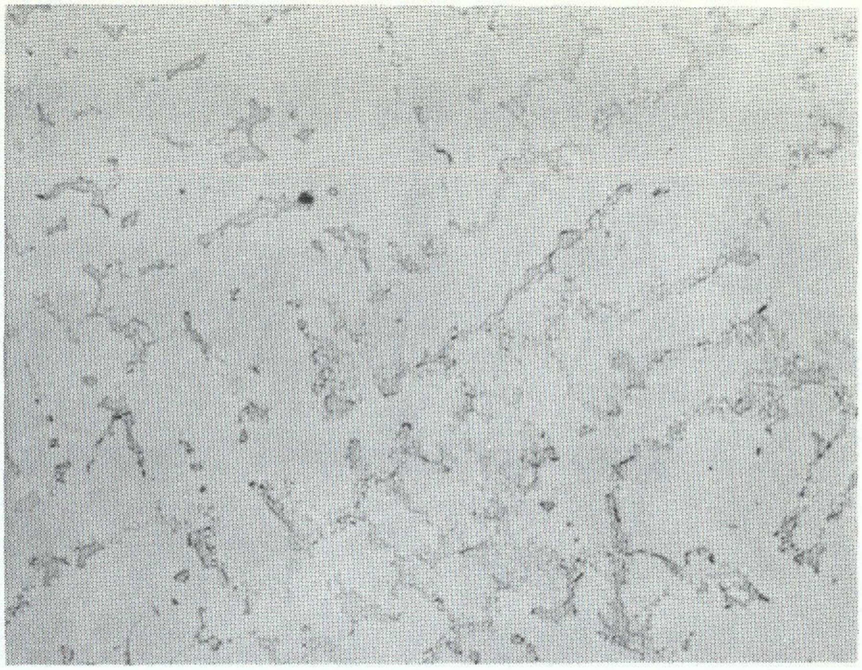

(a) Unetched, X100

Untested transverse section from uniaxial specimen

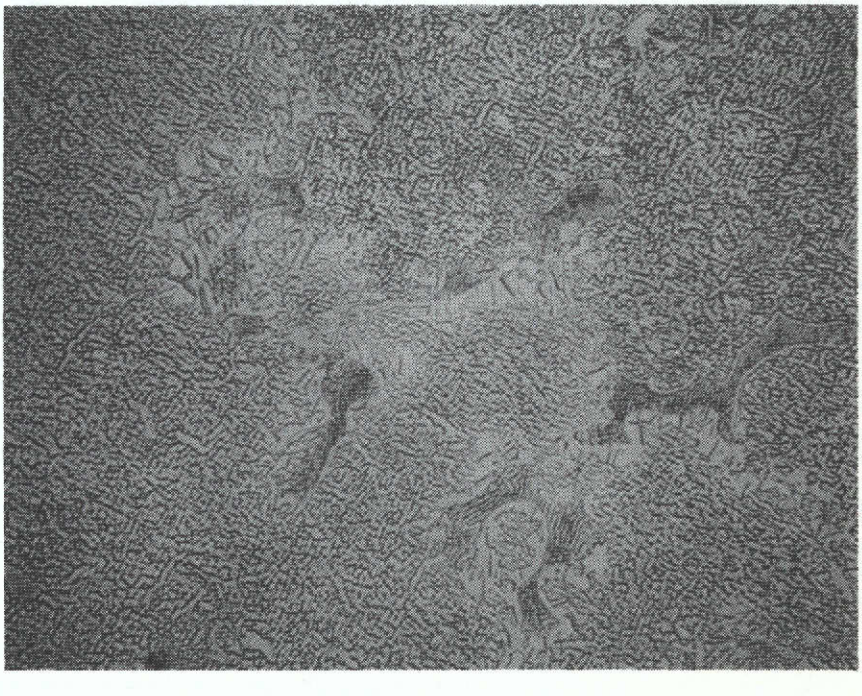

(b) X500

As (a)

Figure 10

Microstructure of NX-188 Specimens (Kalling's etch)

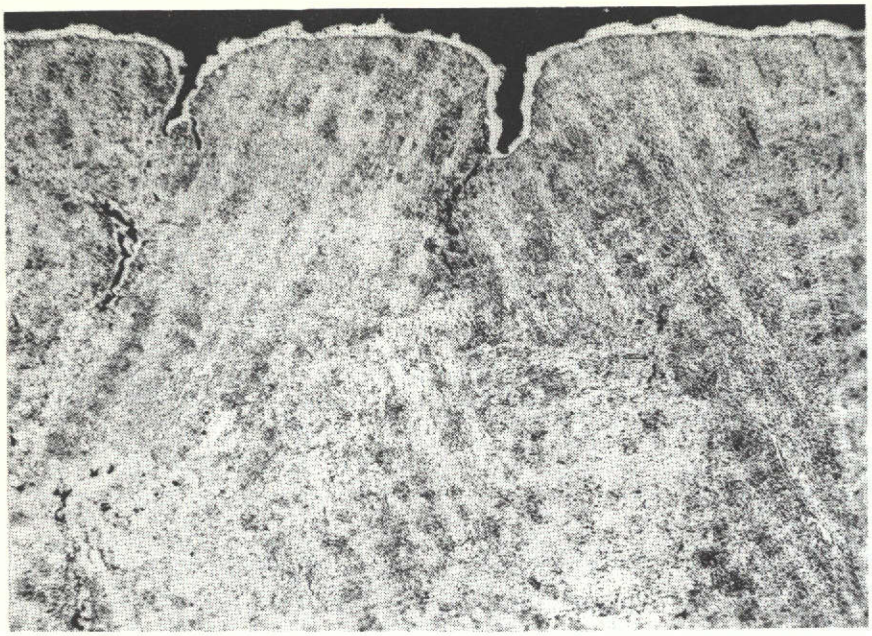

(c) X100

Longitudinal section tested at 2065/675°F for 500 cycles

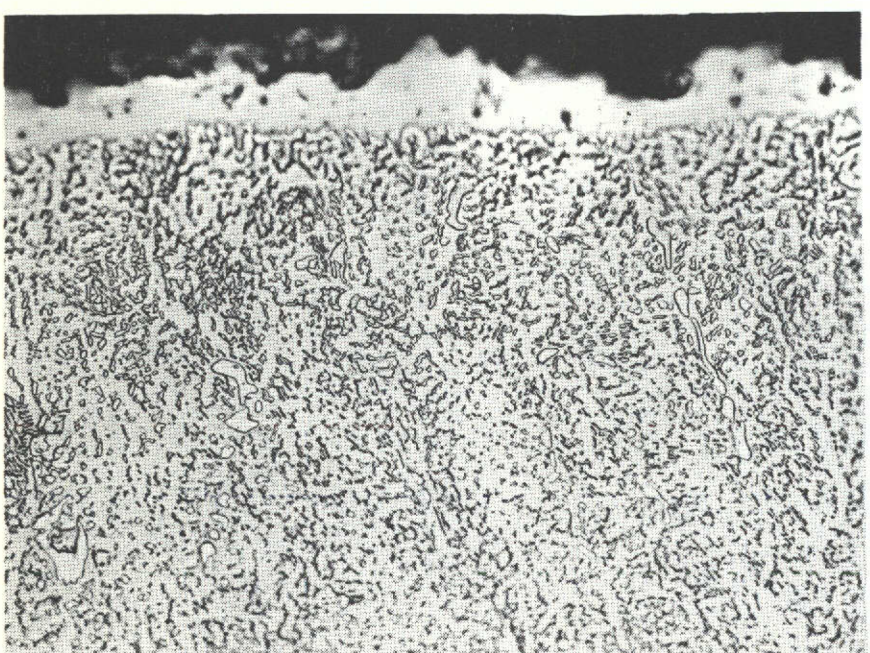

(d) X500

As (c)

Figure 10 (cont.)

Microstructure of NX-188 Specimens

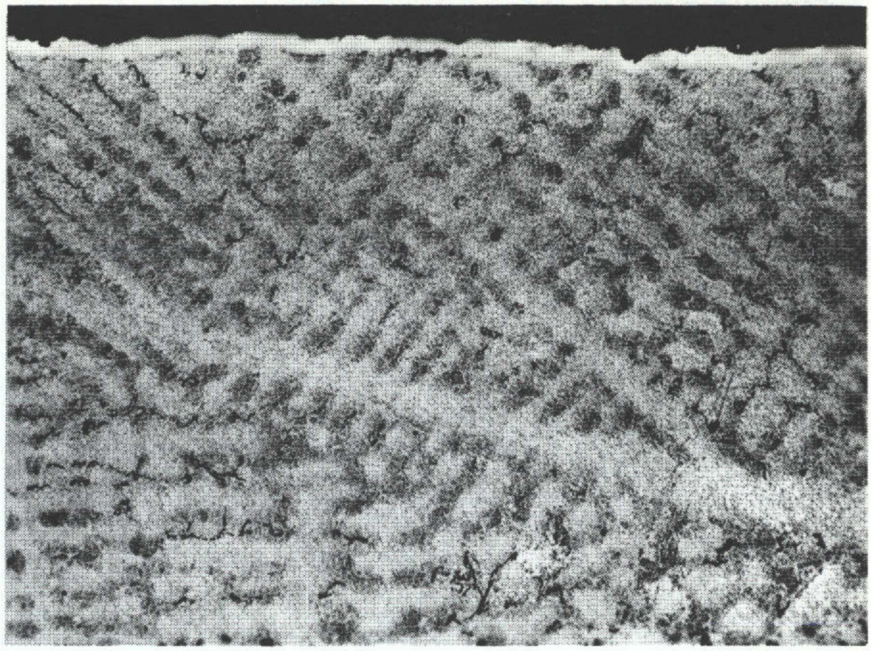

(e) X100

Transverse section tested at 2065/675°F for 500 cycles

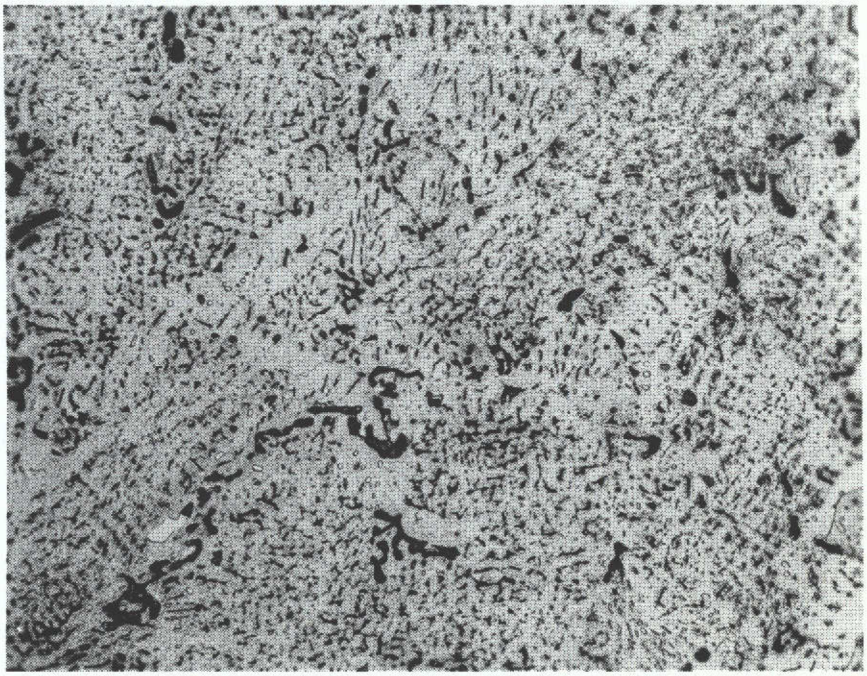

(f) X500

As (e)

Figure 10 (cont.)

Microstructure of NX-188 Specimens

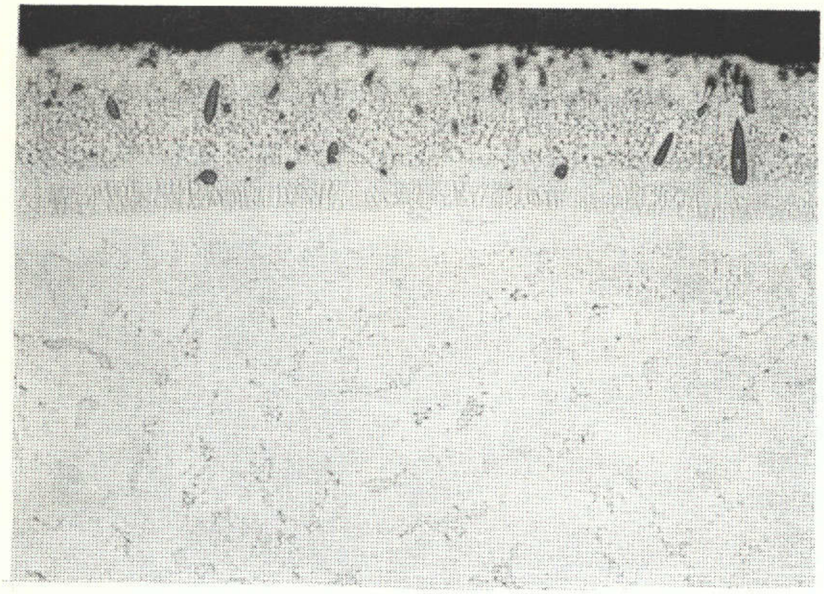

(a) Unetched, X100
Untested transverse section from uniaxial specimen.

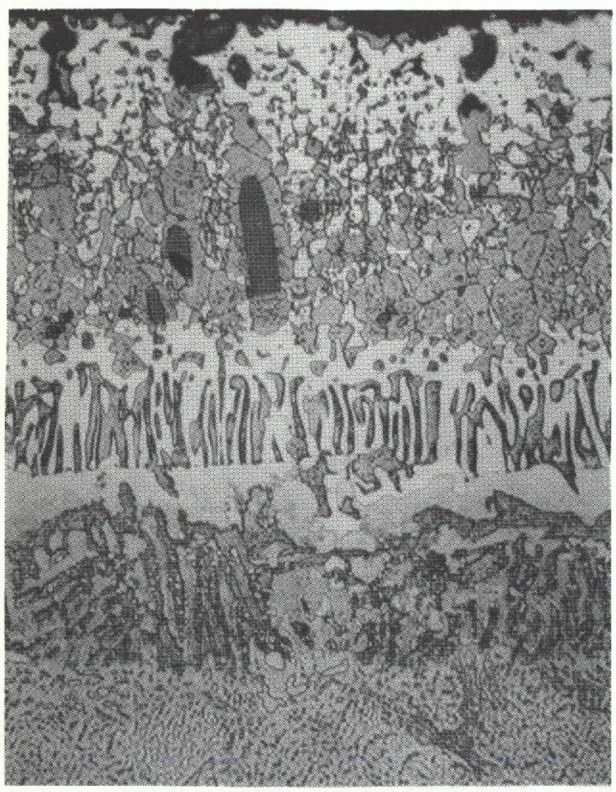

(b) X500
As (a)

Figure 11
Microstructure of NX-188 with RT-1A Coating (Kalling's etch)

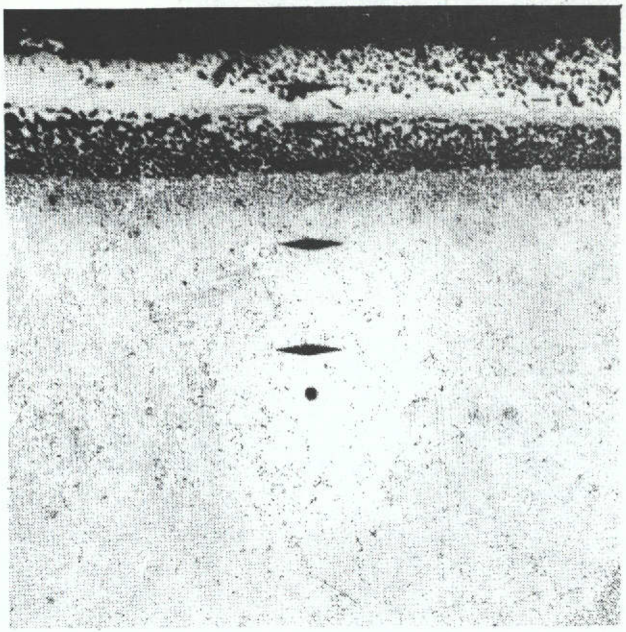

(c) X100
Longitudinal section tested at 2065/675°F for 1100 cycles

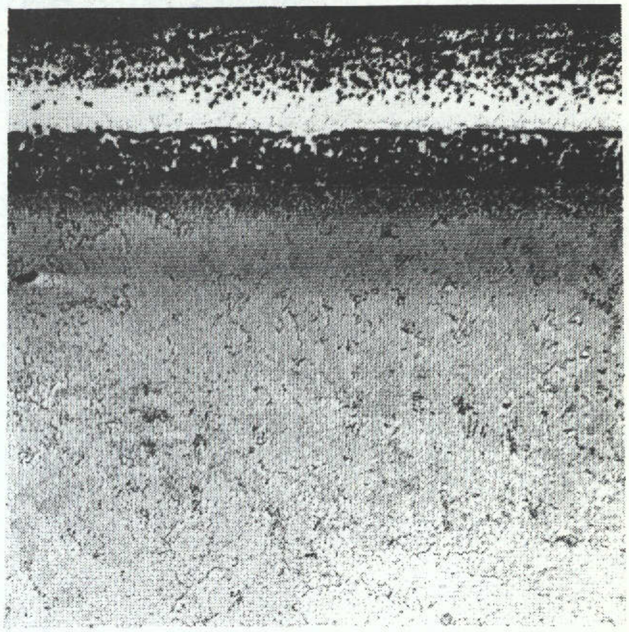

(d) X100
As (c), transverse section

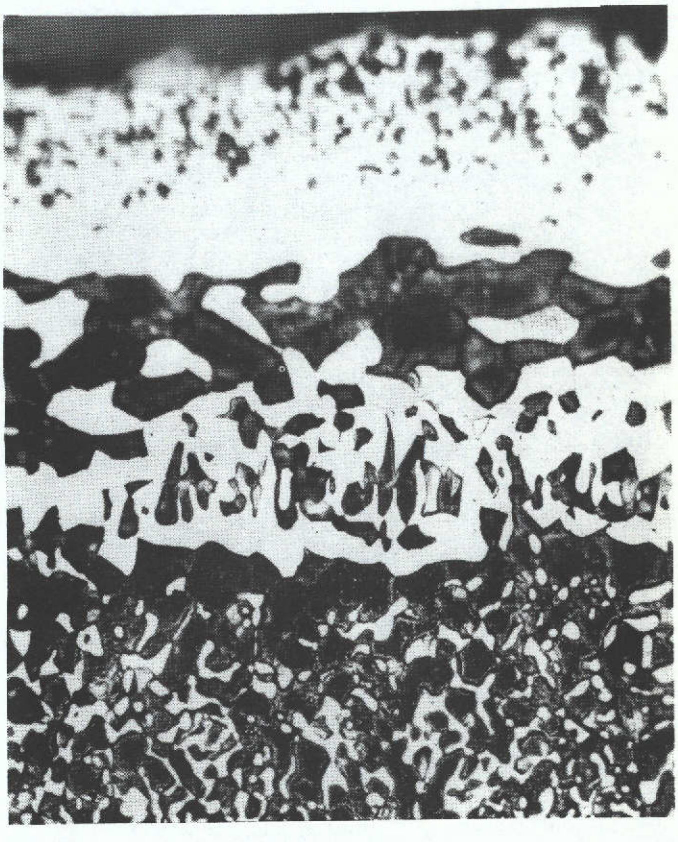

(e) X500
As (d)

Figure 11 (cont.)
Microstructure of NX-188 with RT-1A Coating

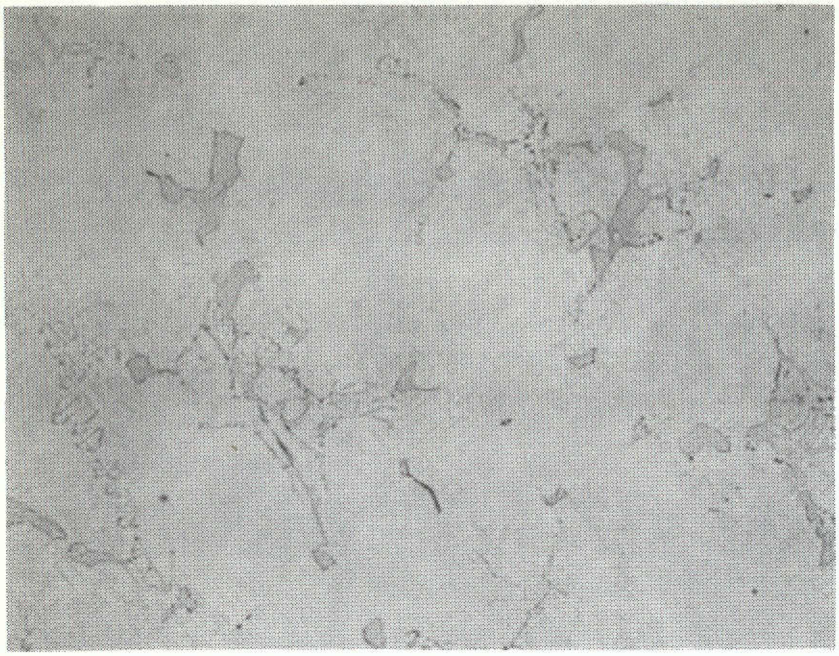

(a) Unetched, X100
Untested transverse section from uniaxial specimen

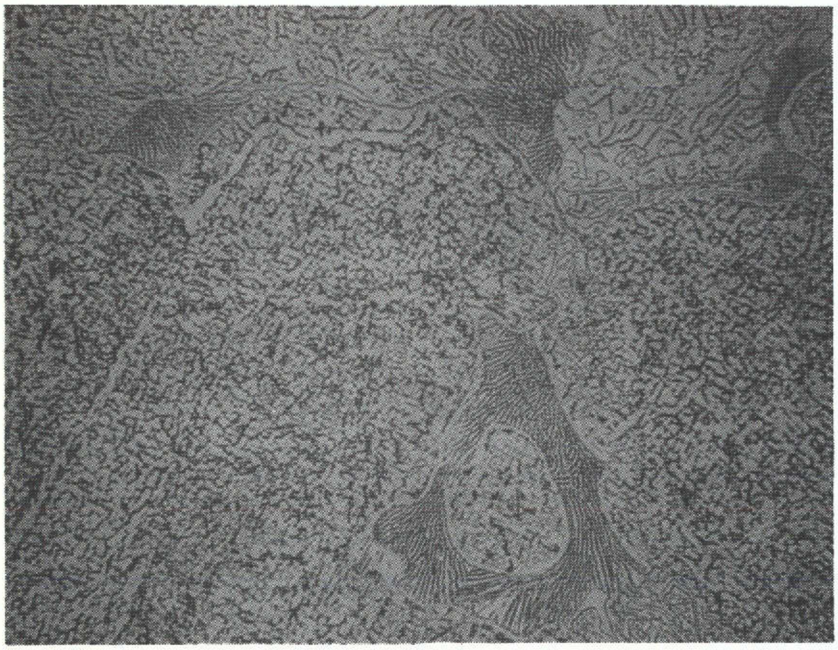

(b) X500
As (a)

Figure 12
Microstructure of NX-188 Directionally Solidified (Kalling's etch)

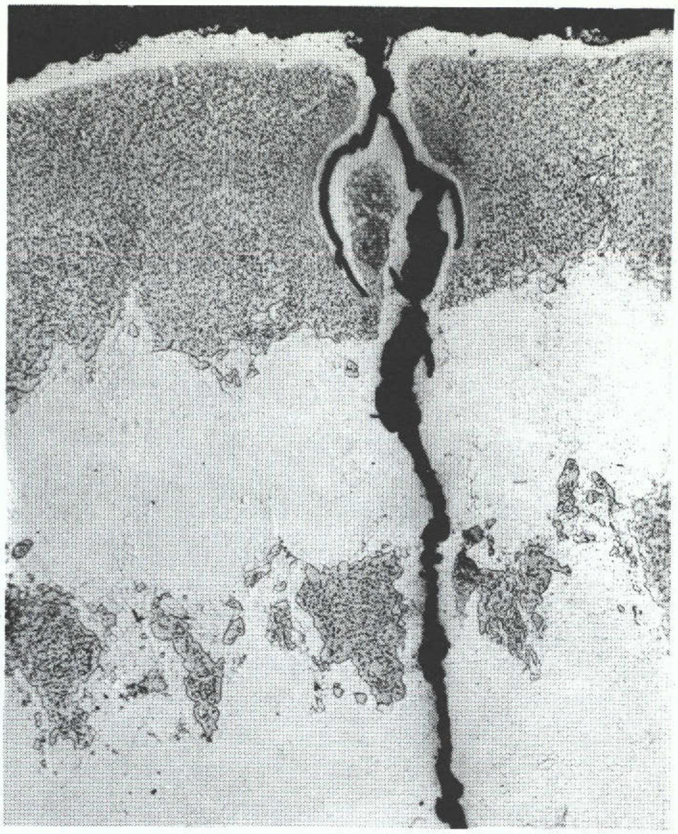

(c) X100
Longitudinal section tested at
2065/675°F for 6500 cycles

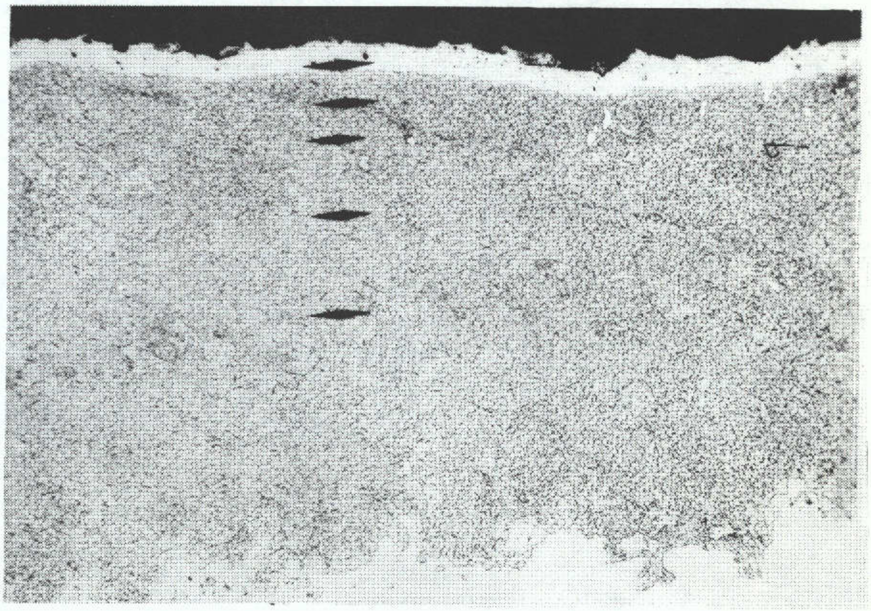

(d) X100
As (c); note the hardness impressions.

Figure 12 (cont.)

Microstructure of NX-188 Directionally Solidified

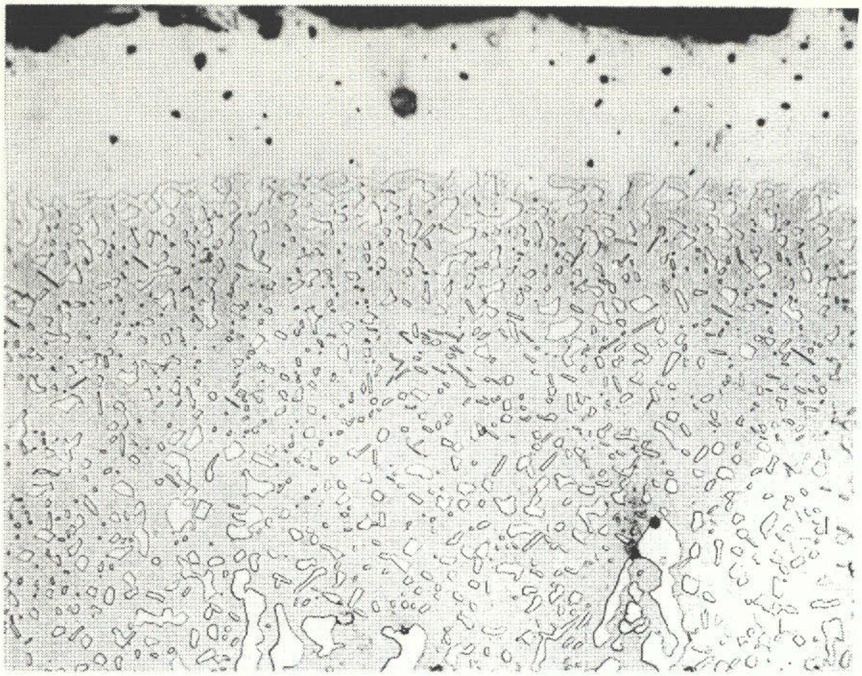

(e) X500

As (c)

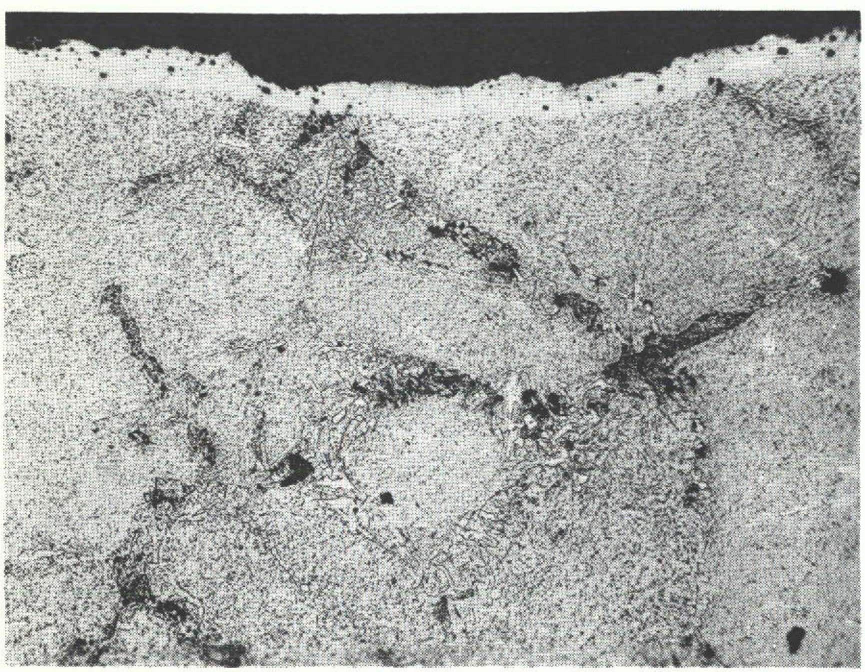

(f) X100

As (c), transverse section

Figure 12 (cont.)

Microstructure of NX-188 Directionally Solidified

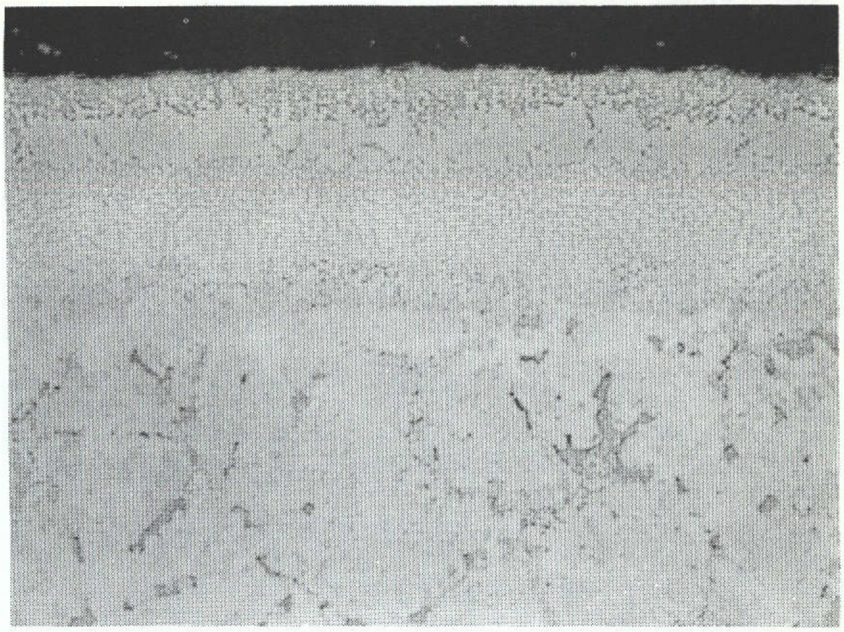

(a) Unetched, X100
Untested transverse section from uniaxial specimen

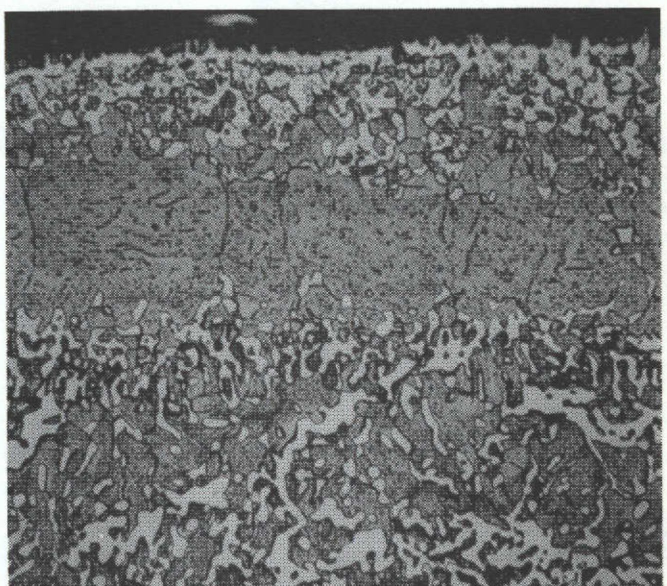

(b) X500
As (a)

Figure 13

Microstructure of NX-188 Directionally Solidified + RT-1A Coating (Kalling's etch)

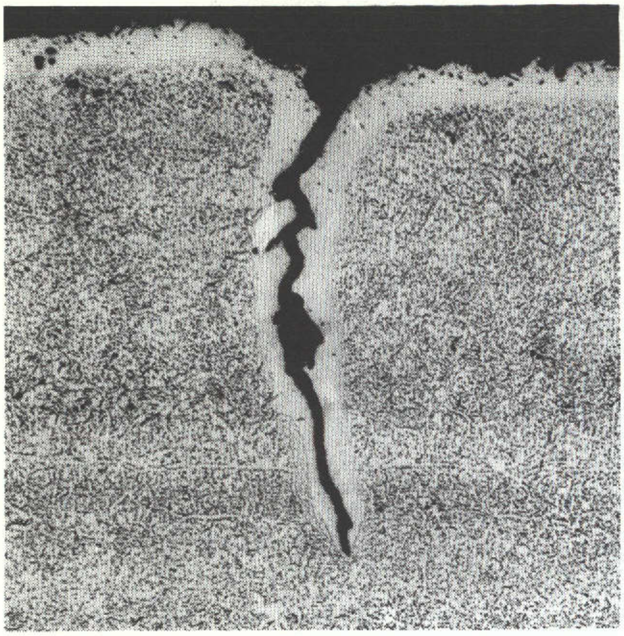

(c) X100
Longitudinal section tested at 2065/675°F for 6100 cycles

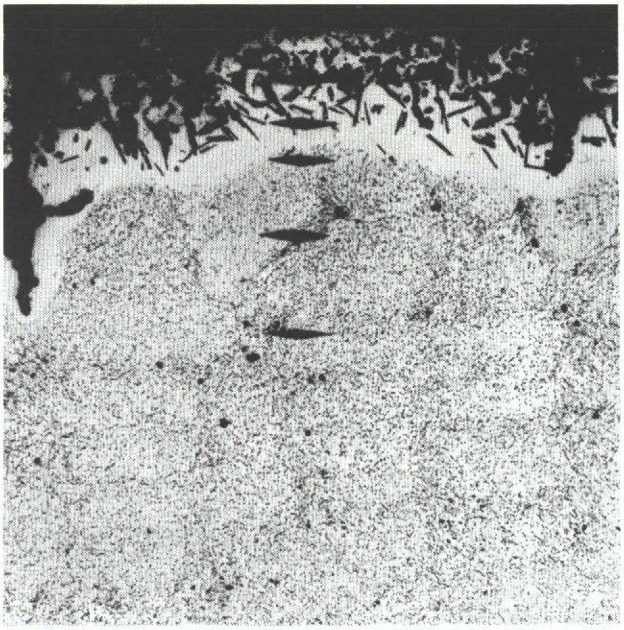

(d) X100
As (c); note the hardness impressions.

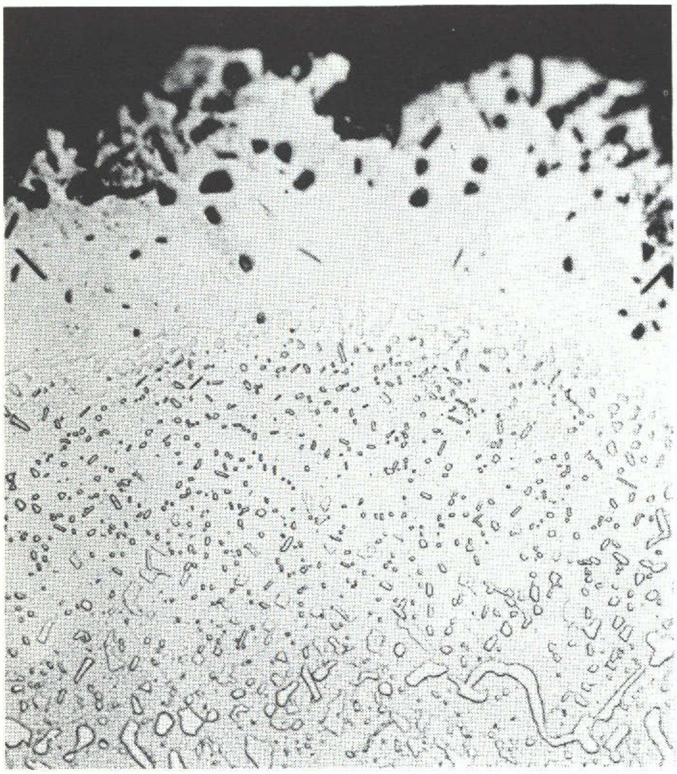

(e) X500
As (c)

Figure 13 (cont.)
Microstructure of NX-188 Directionally Solidified + RT-1A Coating

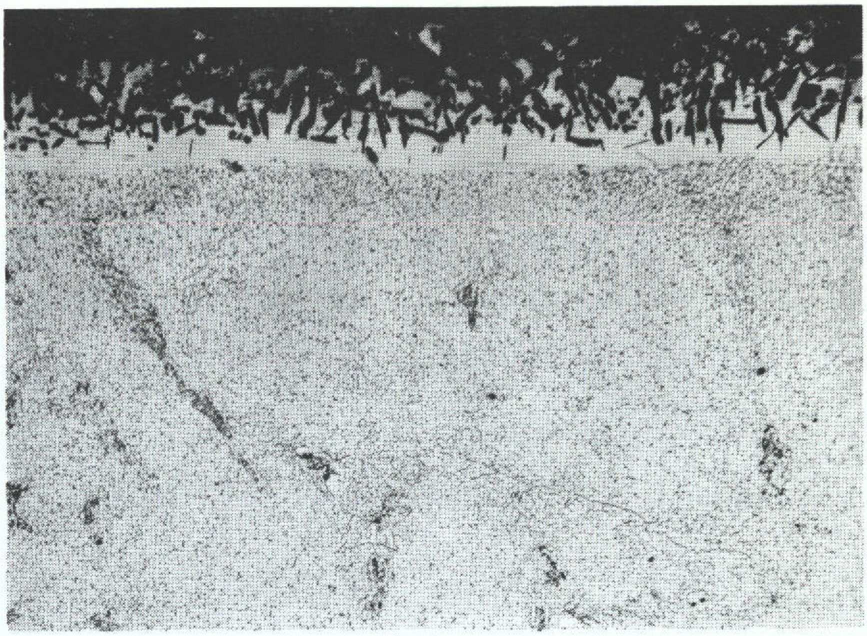

(f) X100
Transverse section tested at 2065/675°F for 6100 cycles

(g) X500
As (f)

Figure 13 (cont.)
Microstructure of NX-188 Directionally Solidified + RT-1A Coating

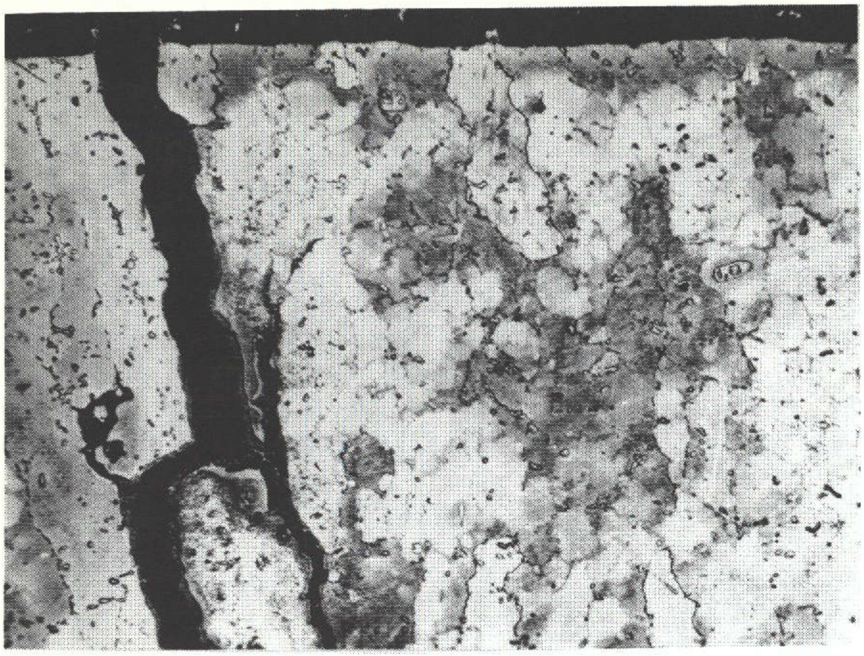

(a) X100

Longitudinal section tested at 2065/675°F for 50 cycles

(b) X100

As (a); note the hardness impressions

Figure 14

Microstructure of WAZ-20 + Jocoat (Kalling's etch)

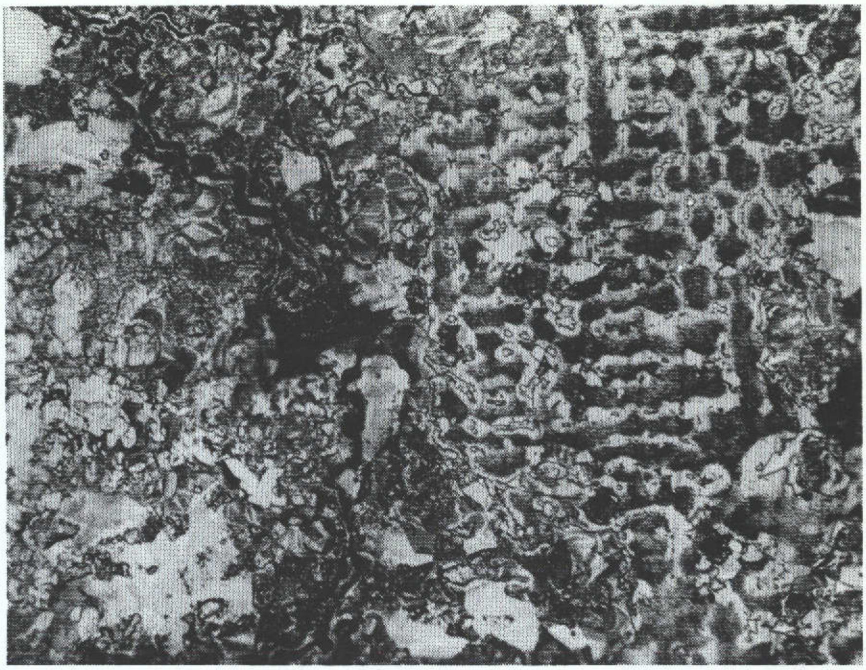

(c) X100

As (a), showing interior dendritic structure

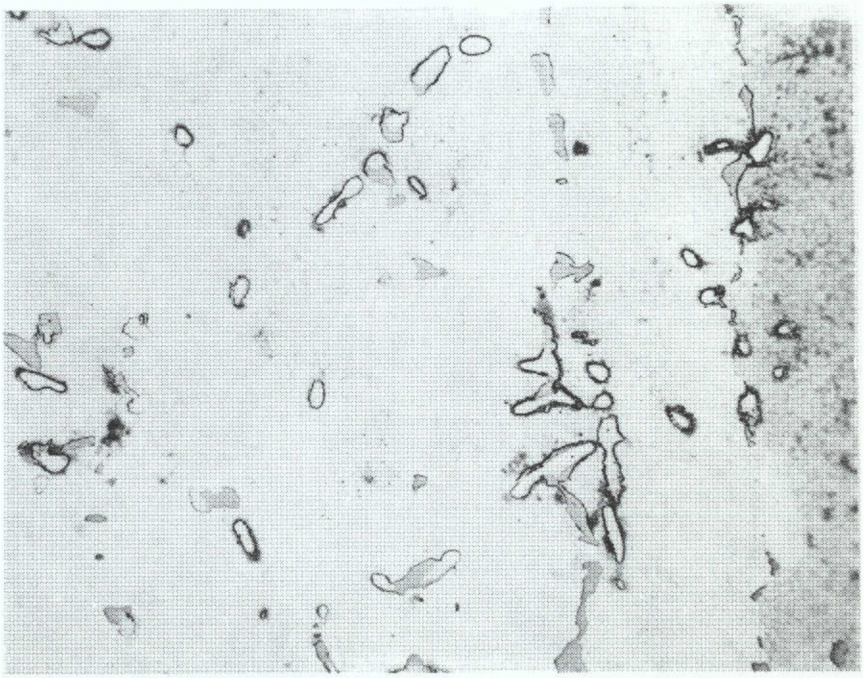

(d) X500

As (a)

Figure 14 (cont.)

Microstructure of WAZ-20 + Jocoat

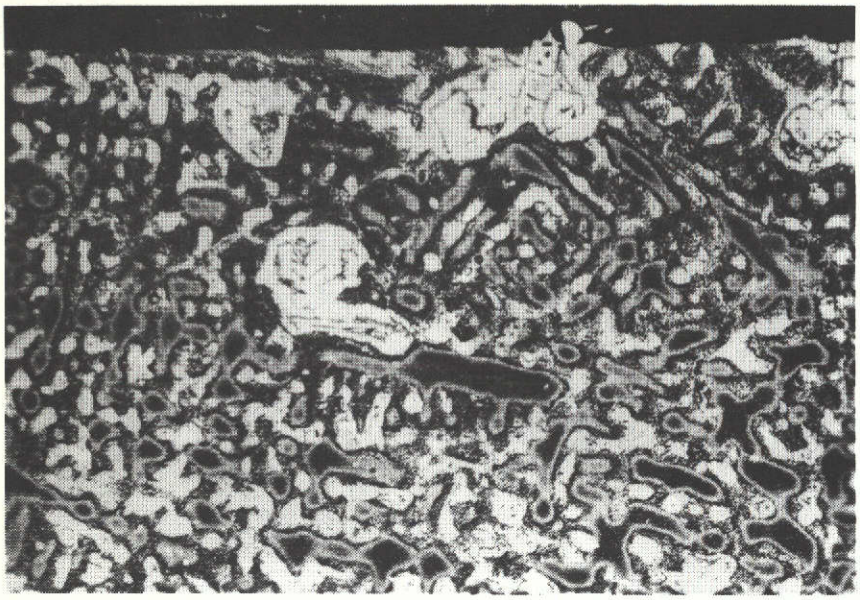

(e) X100

Transverse section tested at 2065/675°F for 50 cycles

(f) X500

As (e)

Figure 14 (cont.)

Microstructure of WAZ-20 + Jocoat

(a) X100

Longitudinal section tested at 2065/675°F for 6100 cycles

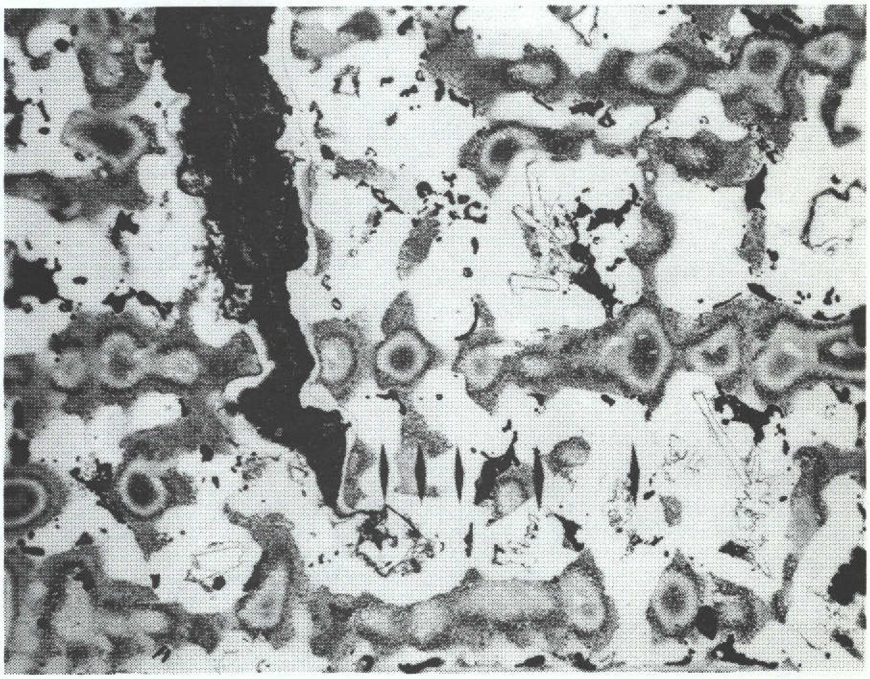

(b) X100

As (a), showing crack tip and hardness impressions

Figure 15

Microstructure of WAZ-20 Directionally Solidified + Jocoat (Kalling's etch)

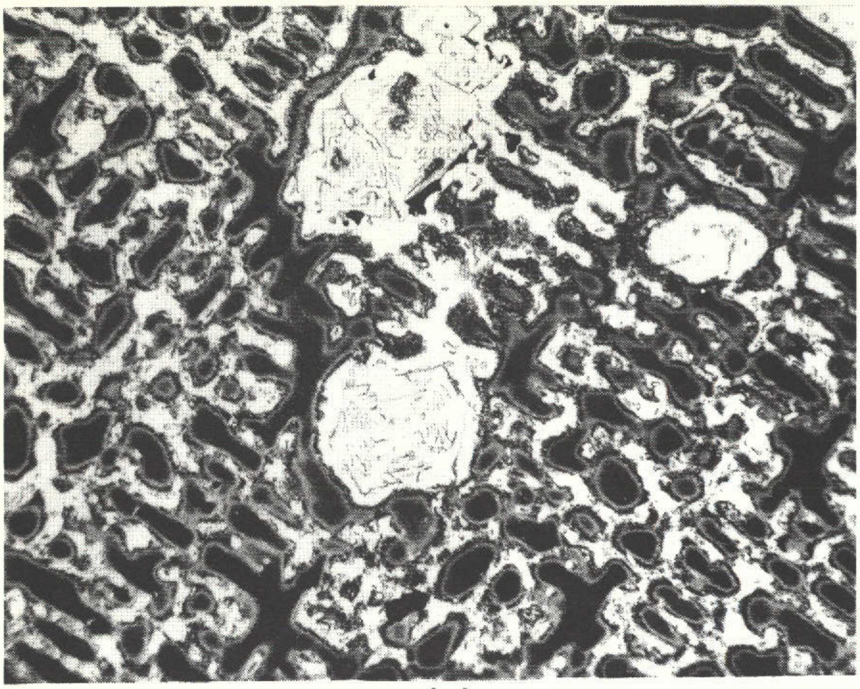

(c) X100

As (a)

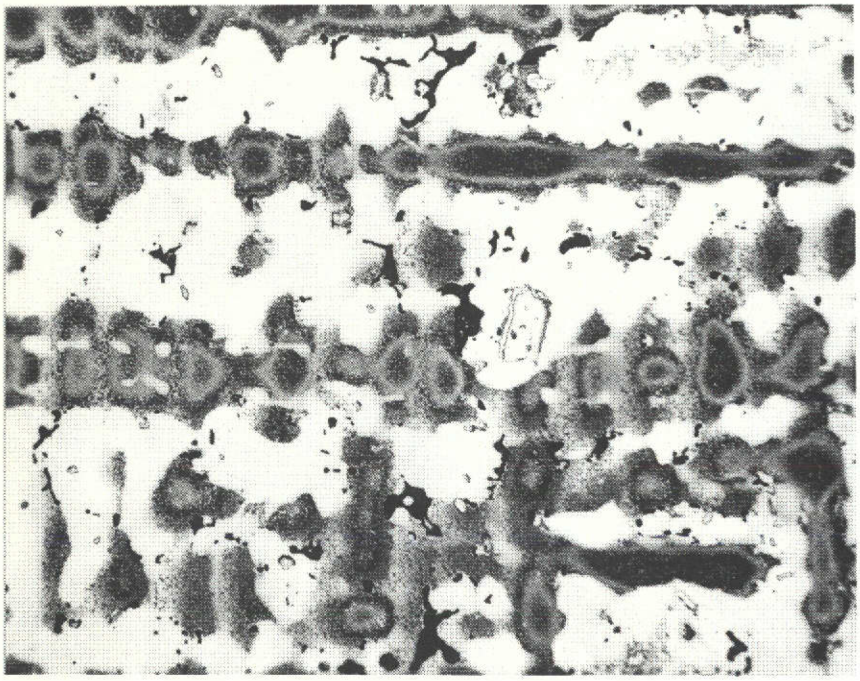

(d) X100

As (a)

Figure 15 (cont.)

Microstructure of WAZ-20 Directionally Solidified + Jocoat

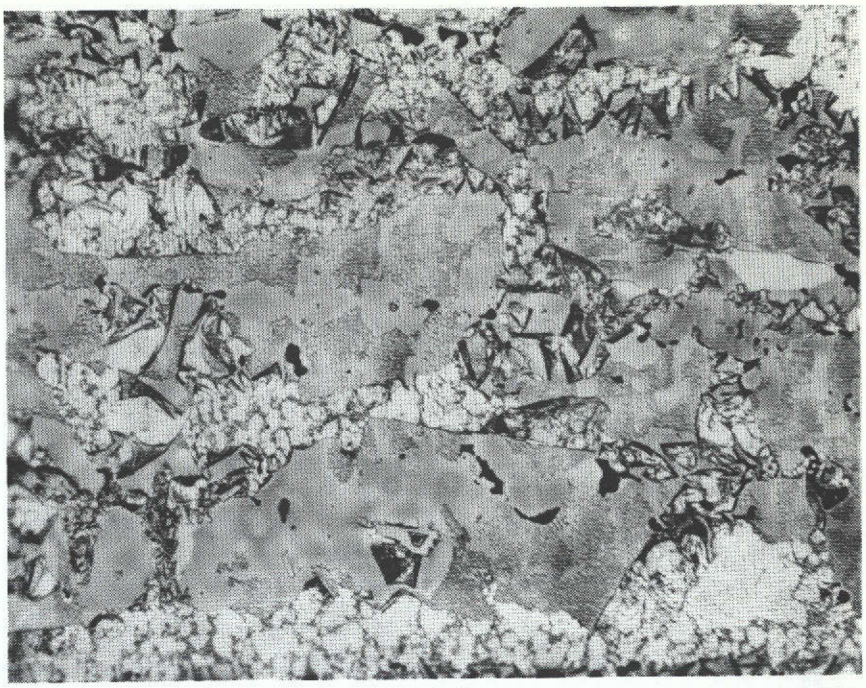

(e) X500

As (a)

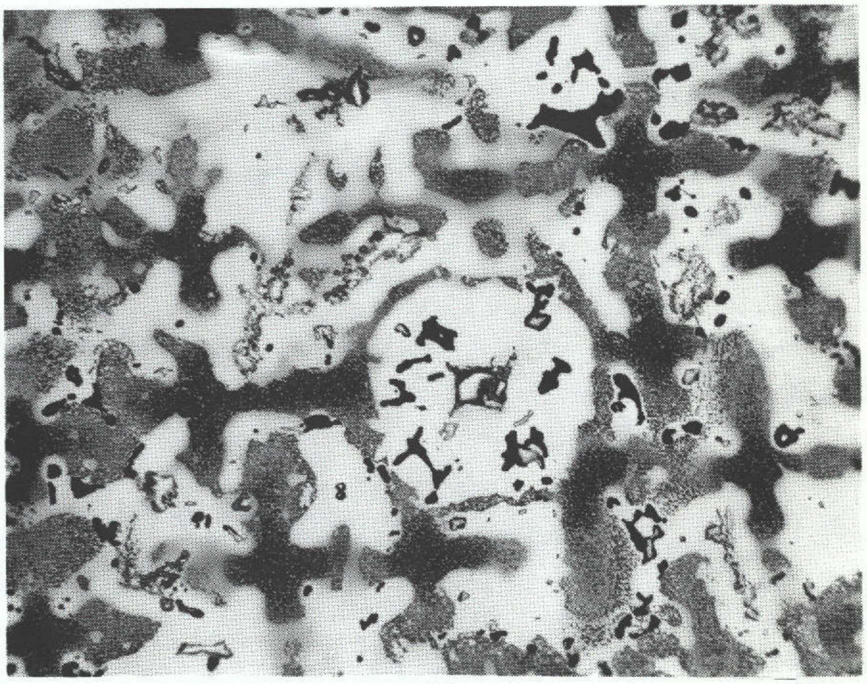

(f) X100

As (a), but transverse section

Figure 15 (cont.)

Microstructure of WAZ-20 Directionally Solidified + Jocoat

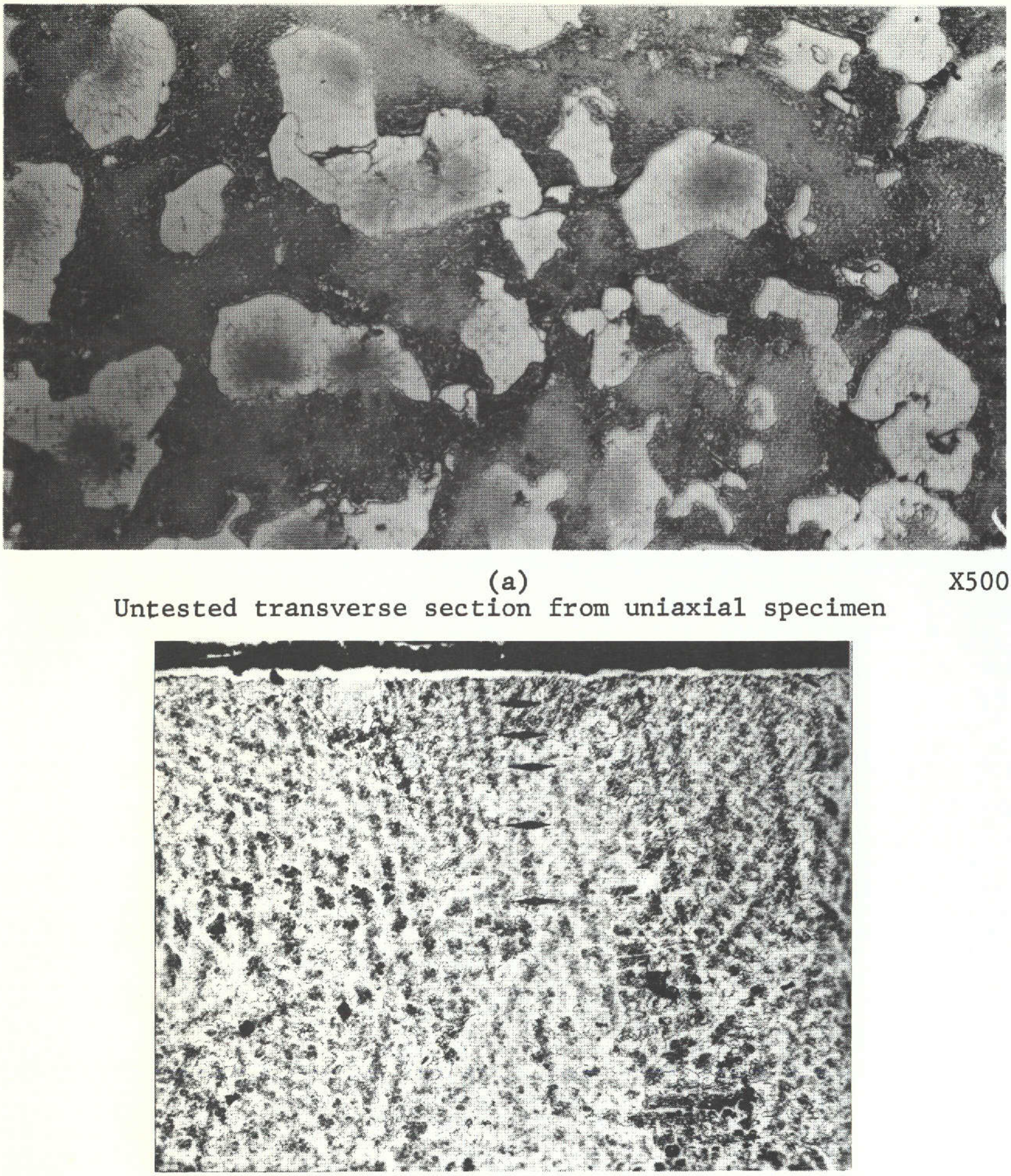

(a) X500
Untested transverse section from uniaxial specimen

(b) X100
Double wedge, longitudinal section tested at 2065/675°F for 1100 cycles

Figure 16
Microstructure of TAZ-8A (Kalling's etch)

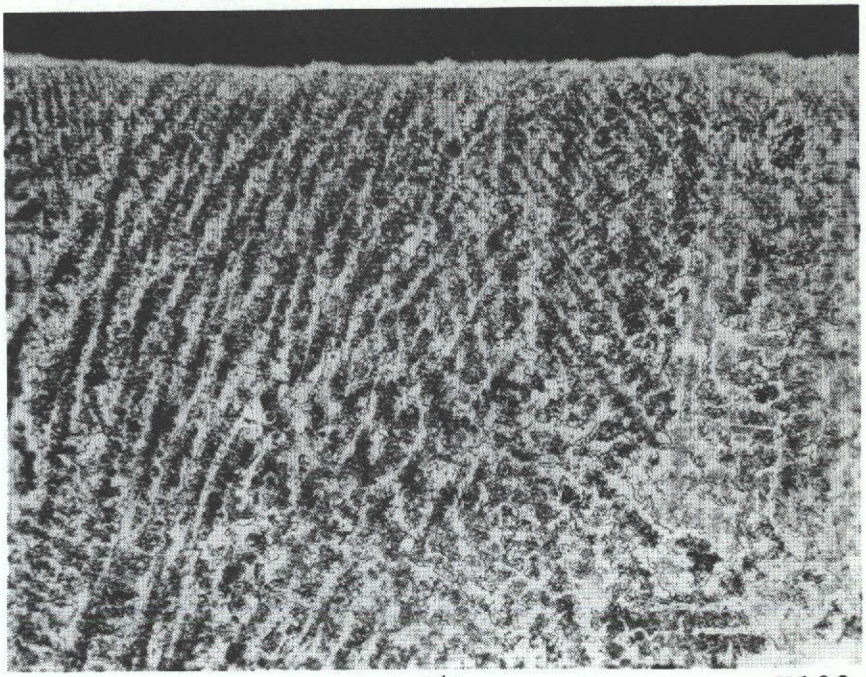

(c) X100

As (b)

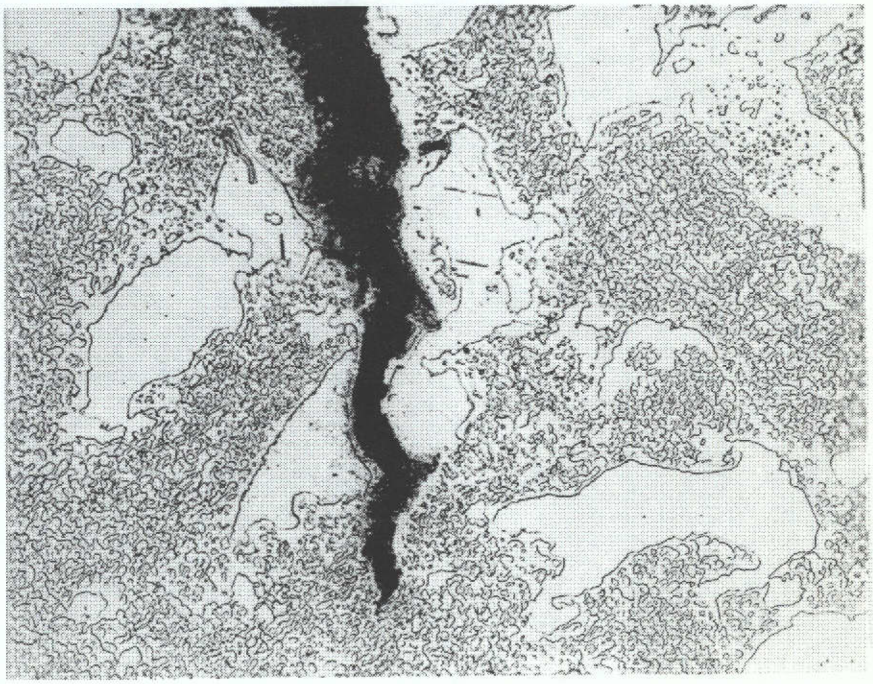

(d) X500

As (b)

Figure 16 (cont.)

Microstructure of TAZ-8A

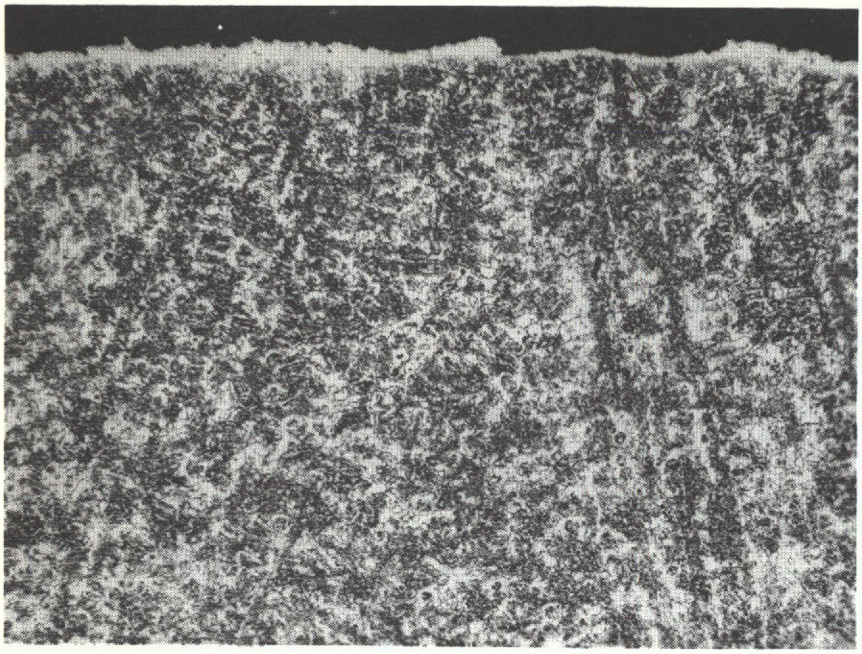

(e) X100

SEW, longitudinal section tested at 2065/675°F for 6100 cycles

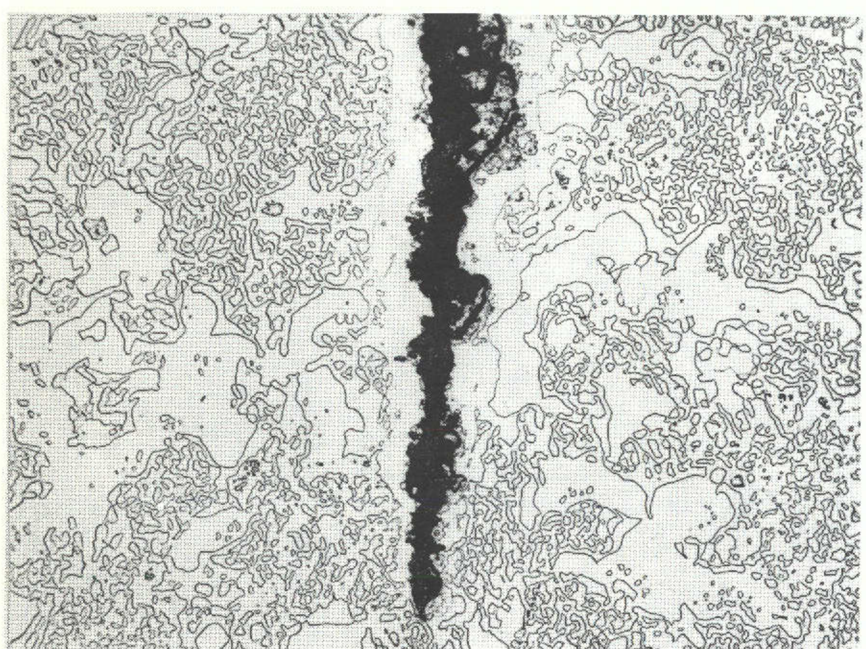

(f) X500

As (e)

Figure 16 (cont.)

Microstructure of TAZ-8A

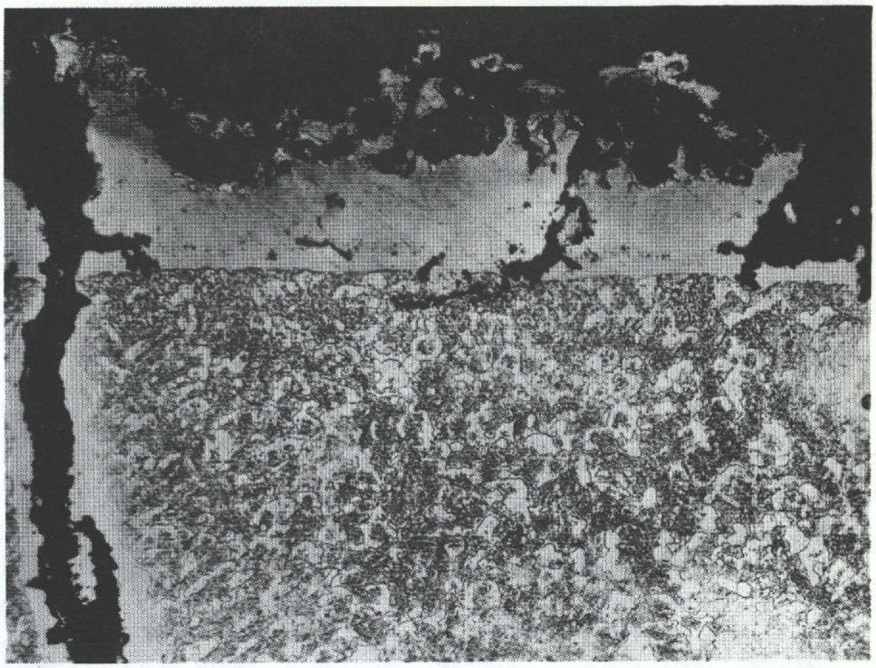

(a) X100

Longitudinal section tested at 2065/675°F for 6100 cycles

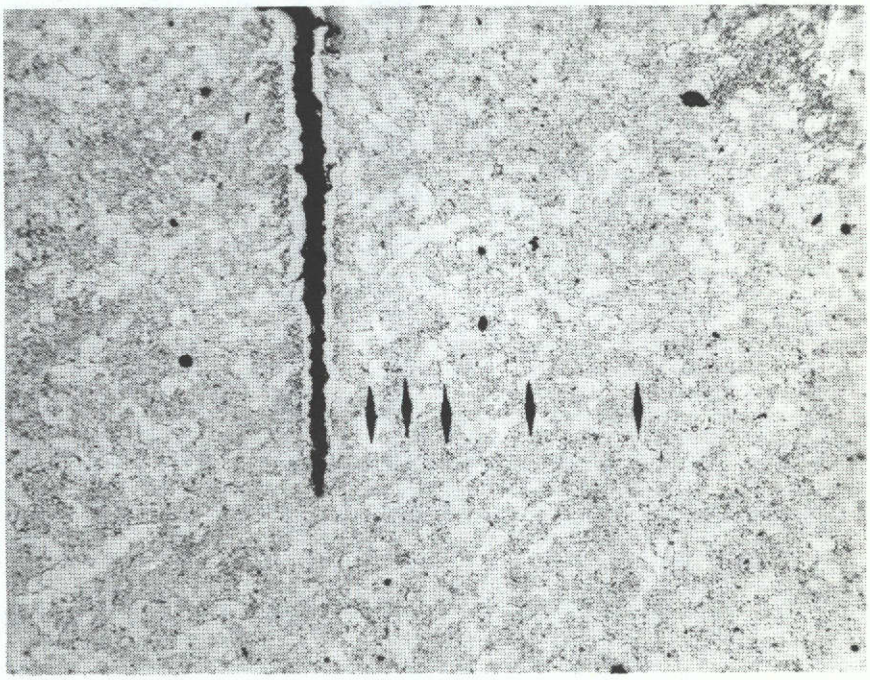

(b) X100

As (a); note hardness impressions

Figure 17

Microstructure of TAZ-8A (SEW) Clad + Xcoat B (Kalling's etch)

(c) X500

As (a)

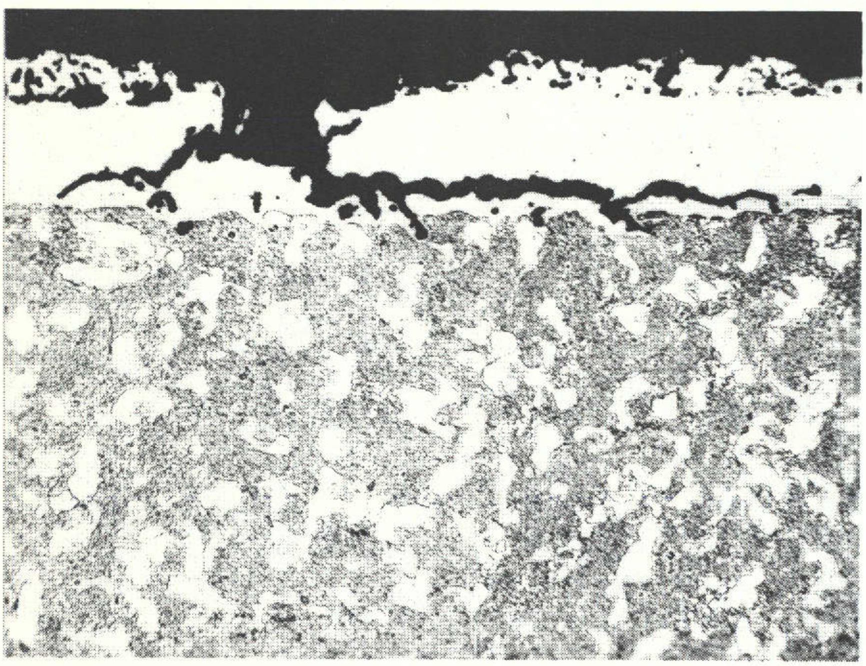

(d) X100

Transverse section tested at 2065/675°F for 6100 cycles

Figure 17 (cont.)

Microstructure of TAZ-8A (SEW) Clad + Xcoat B

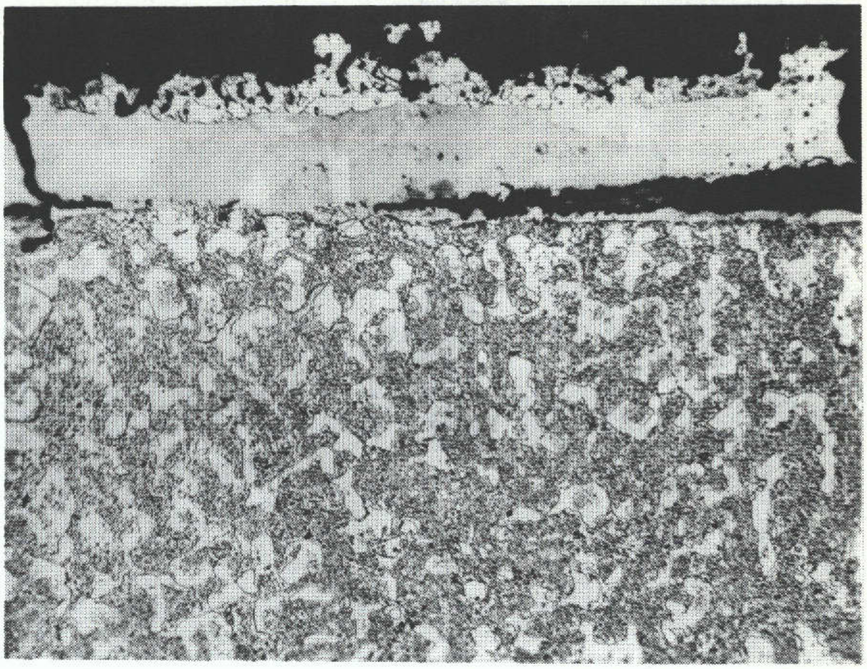

(e) X100

As (d)

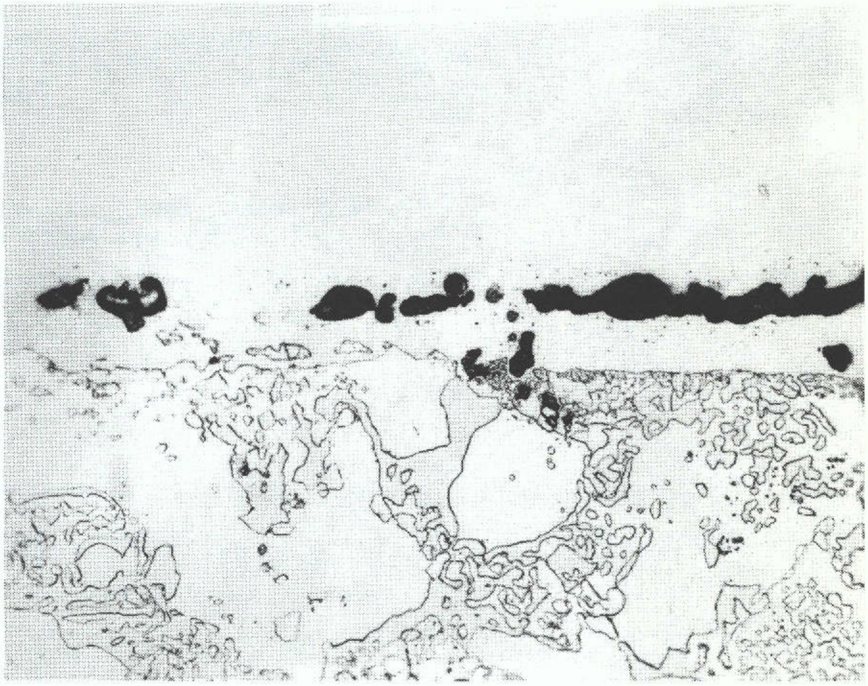

(f) X500

As (d)

Figure 17 (cont.)

Microstructure of TAZ-8A (SEW) Clad + Xcoat B

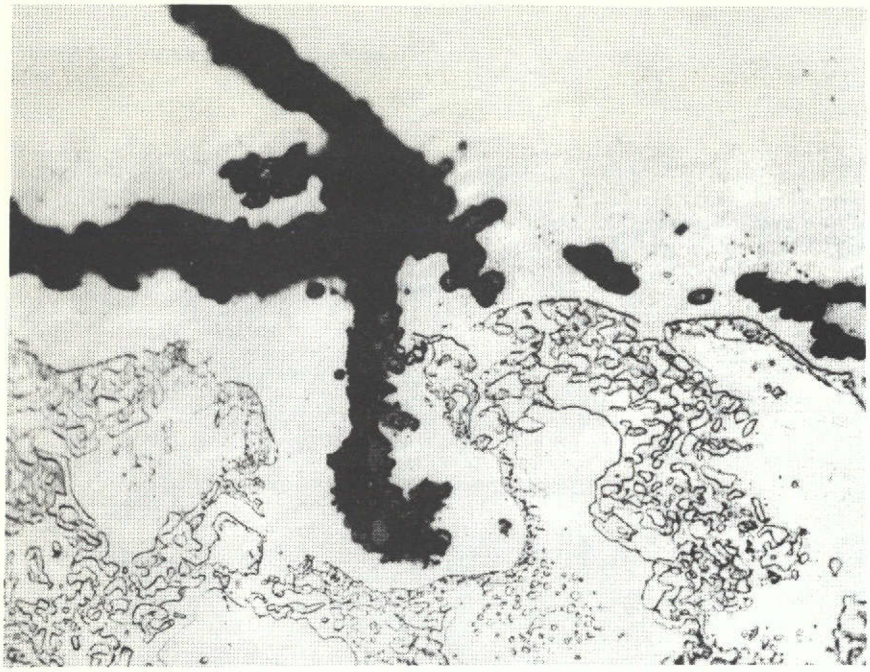

(g) X500

As (d)

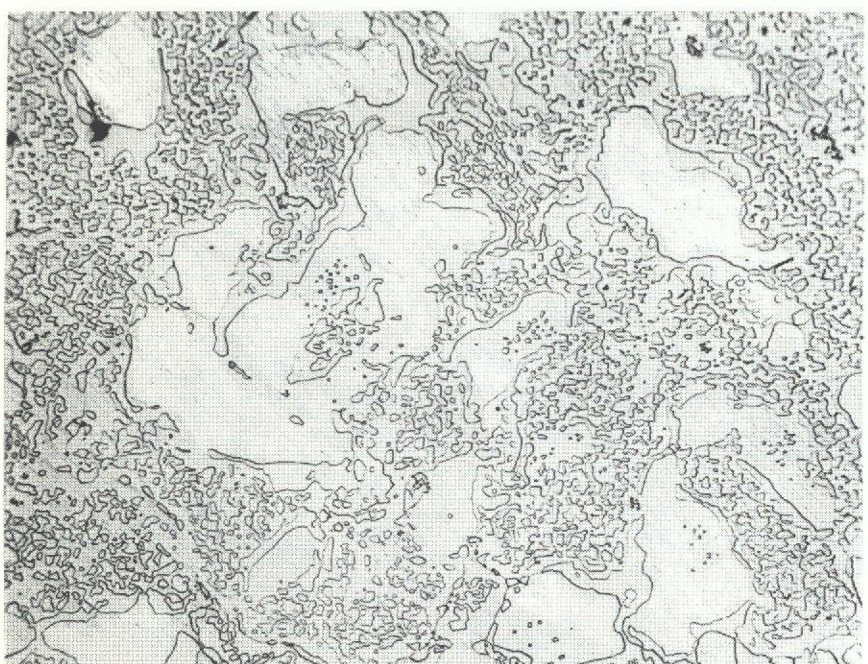

(h) X500

As (d)

Figure 17 (cont.)

Microstructure of TAZ-8A (SEW) Clad + Xcoat B

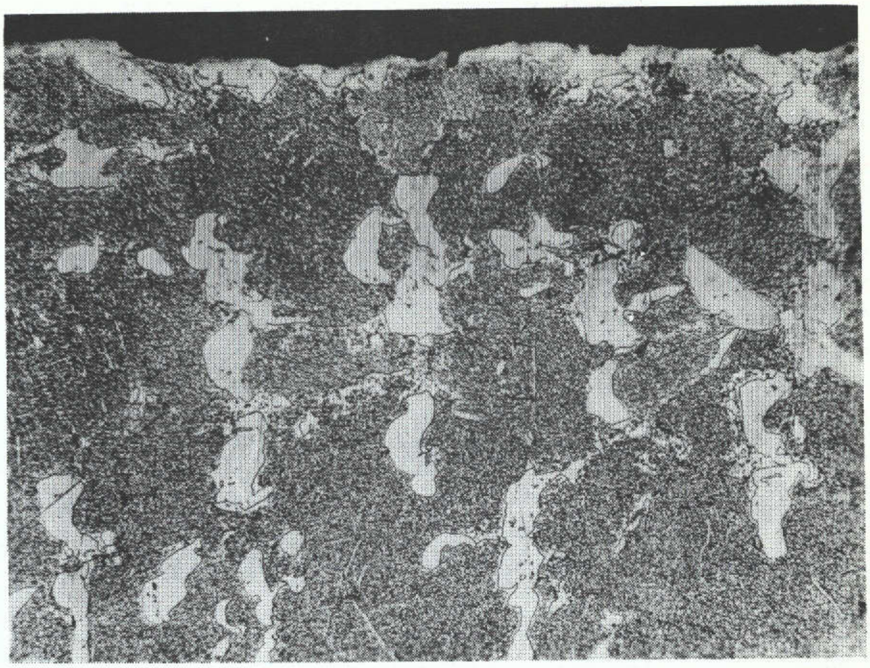

(a) X100

Longitudinal section tested at 2065/675°F for 2200 cycles

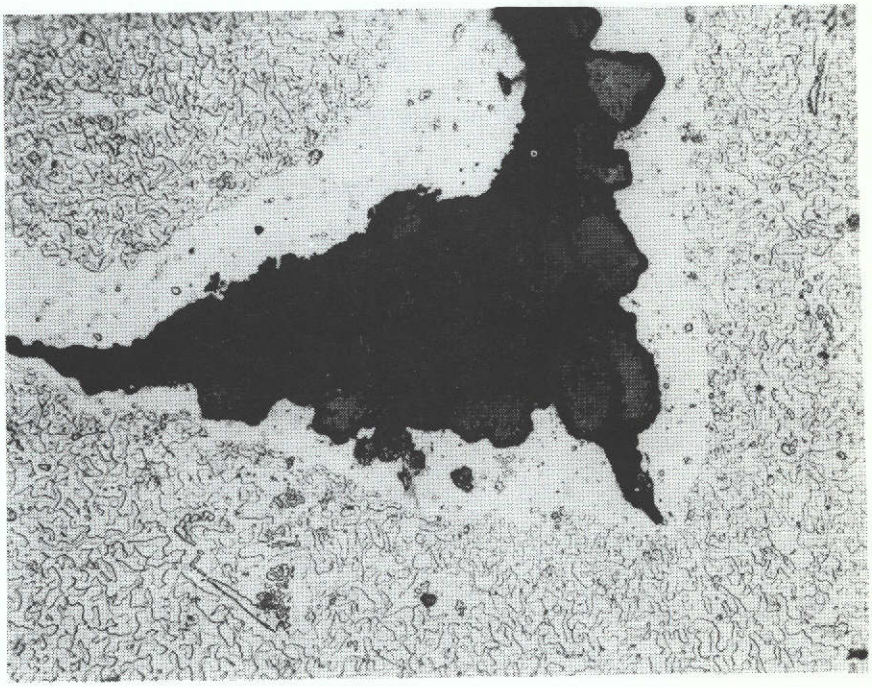

(b) X500

As (a)

Figure 18

Microstructure of TAZ-8A Directionally Solidified (Kalling's etch)

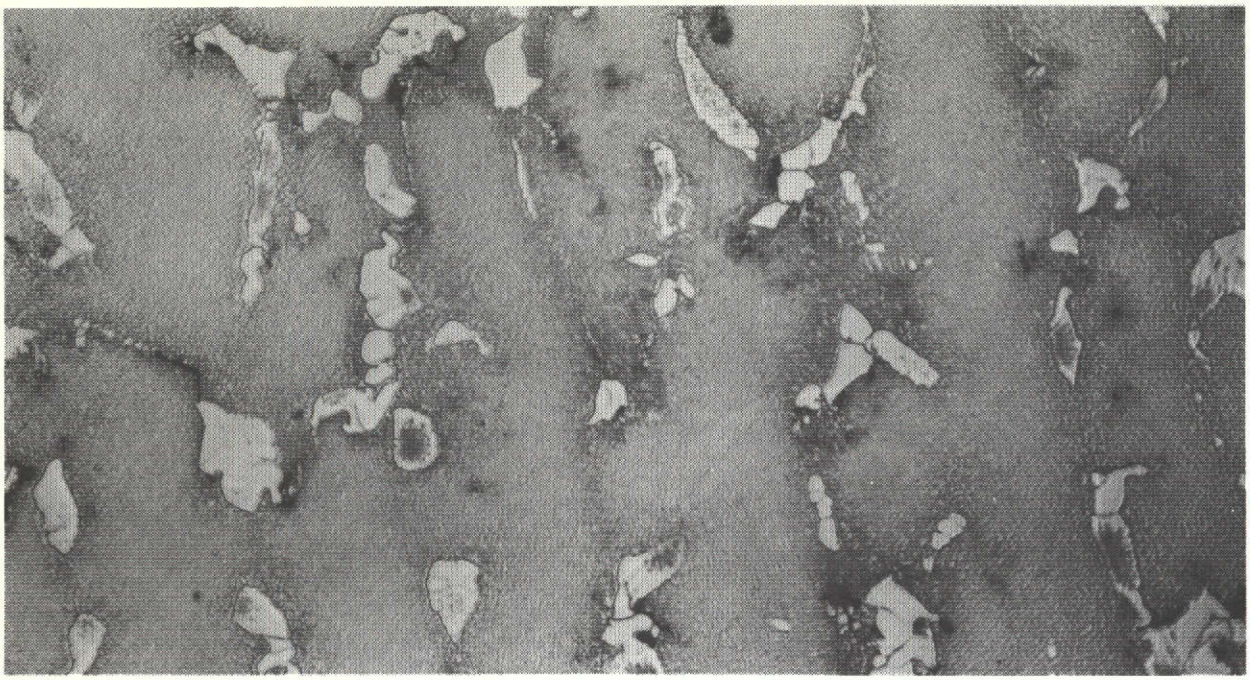

(a) X500

Untested transverse section from uniaxial specimen

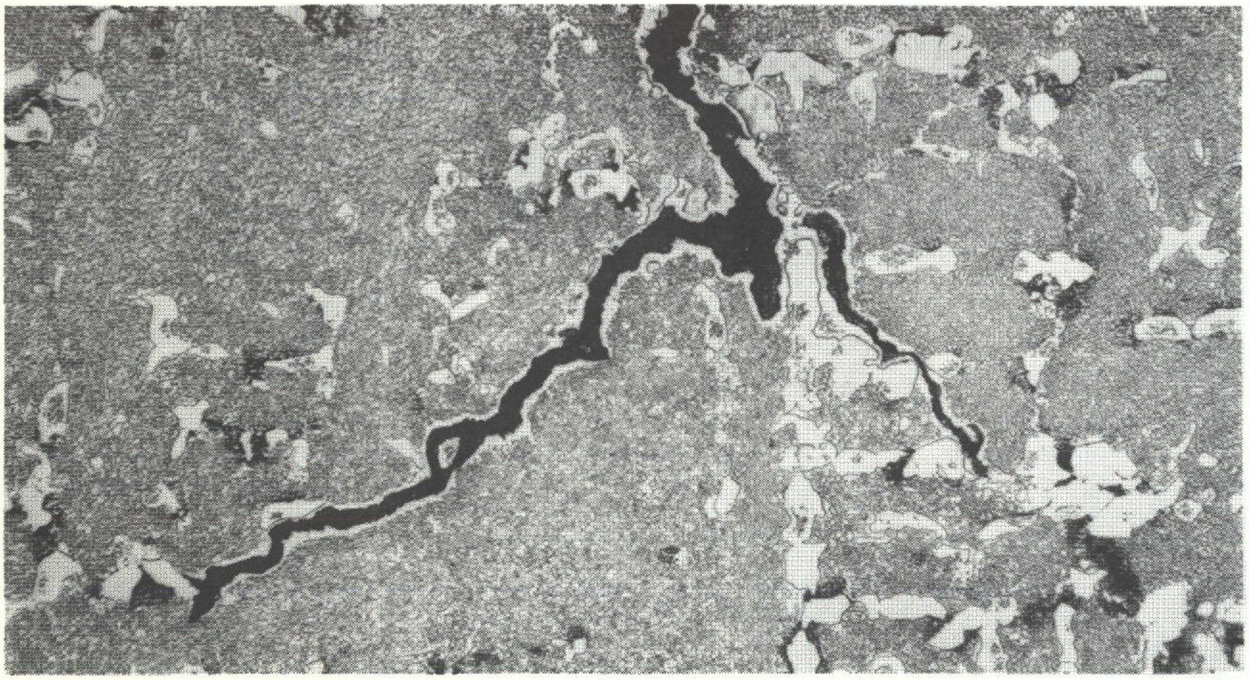

(b) X500

Longitudinal section tested at 1990/600°F for 500 cycles

Figure 19

Microstructure of M22 Specimens. (10% H_2PO_4 electrolytic etch)

X500

Figure 20

Microstructure of IN 713C Specimen. Untested transverse section from uniaxial specimen. (10% H_2PO_4 electrolytic etch)

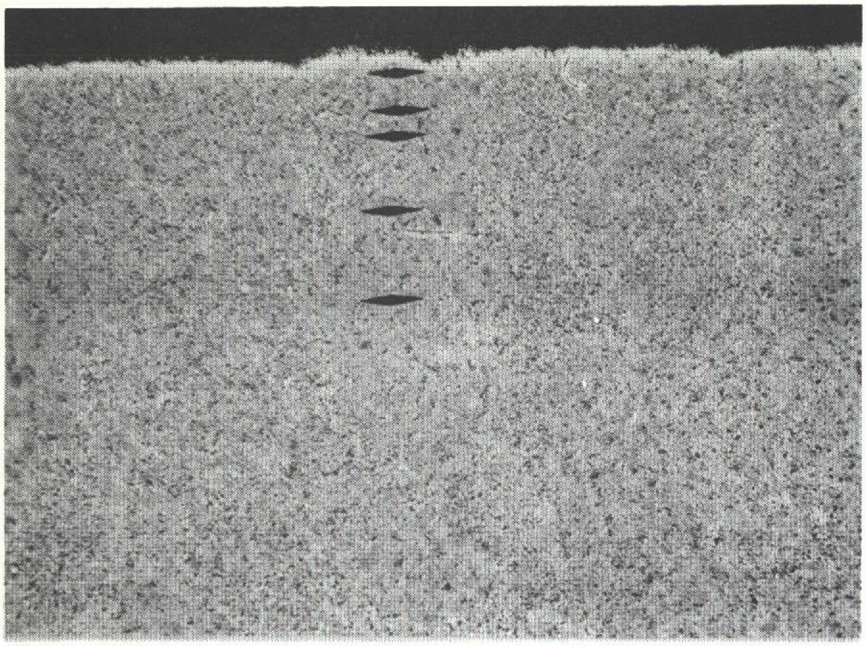

(a) X100
Longitudinal section tested at 2065/675°F for 200 cycles

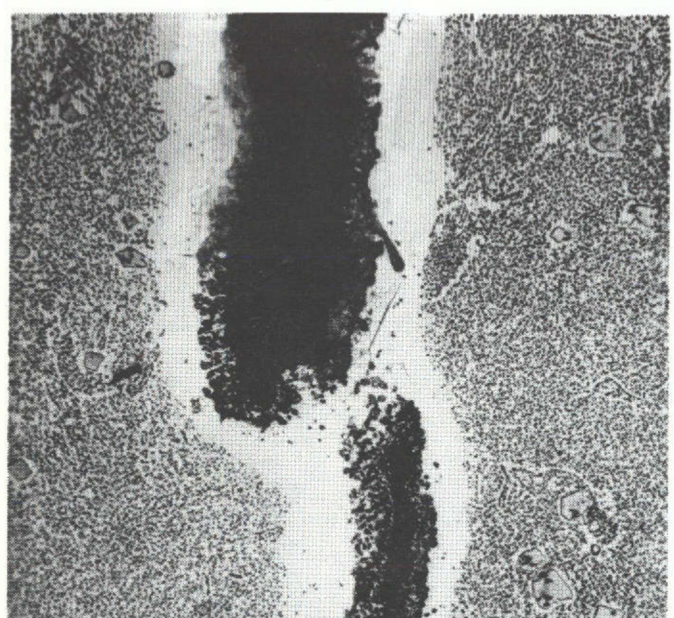

(b) X500
As (a)

Figure 21
Microstructure of IN 738 Specimen (Kalling's etch)

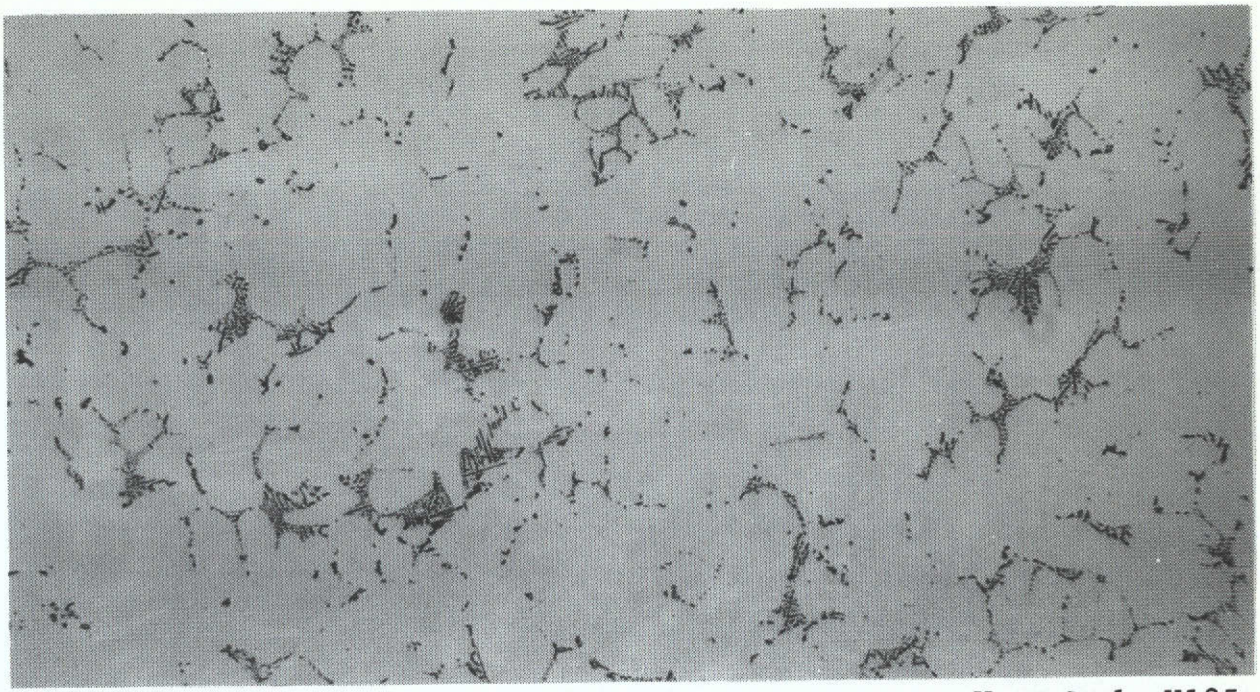

(a) Unetched, X125

Untested transverse section from uniaxial specimen

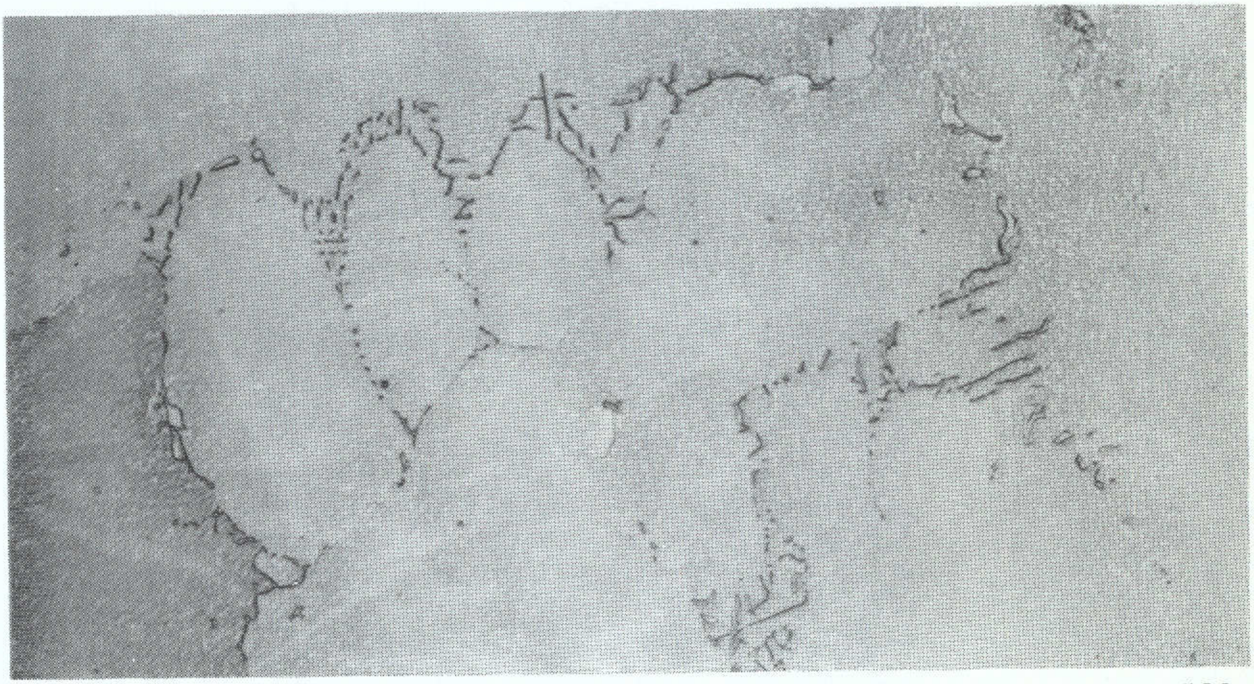

(b) X500

As (a)

Figure 22

Microstructure of IN 162 Specimen (10% H_2PO_4 electrolytic etch)

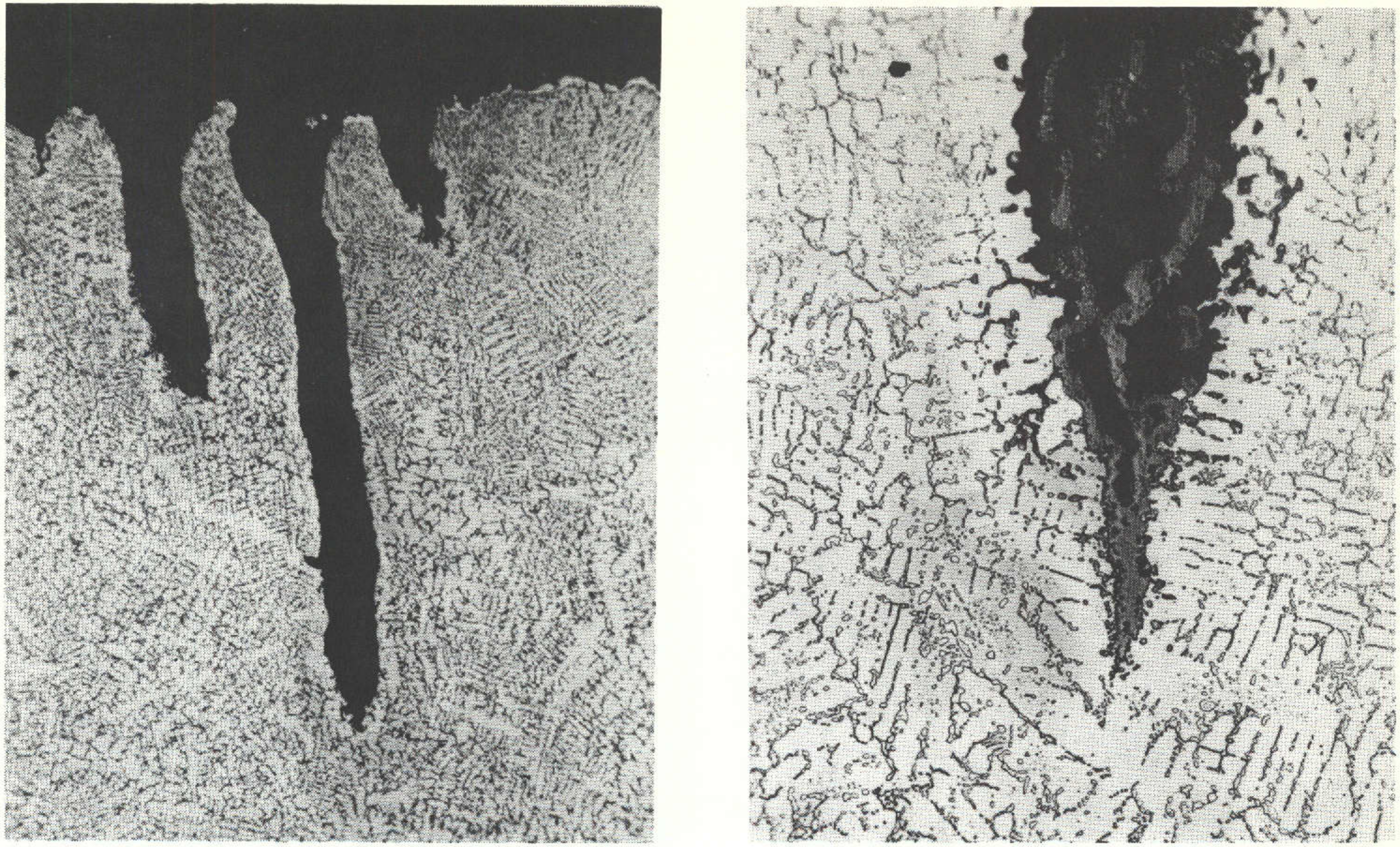

(a) X100
Longitudinal section tested at 2065/675°F for 600 cycles

(b) X500
As (a)

Figure 23

Microstructure of MAR-M 509 Specimen (10% H_2SO_4 electrolytic etch)

X500

Figure 24

Microstructure of René 80. Longitudinal section tested at 2065/675°F for 200 cycles. (10% H_2SO_4 electrolytic etch)

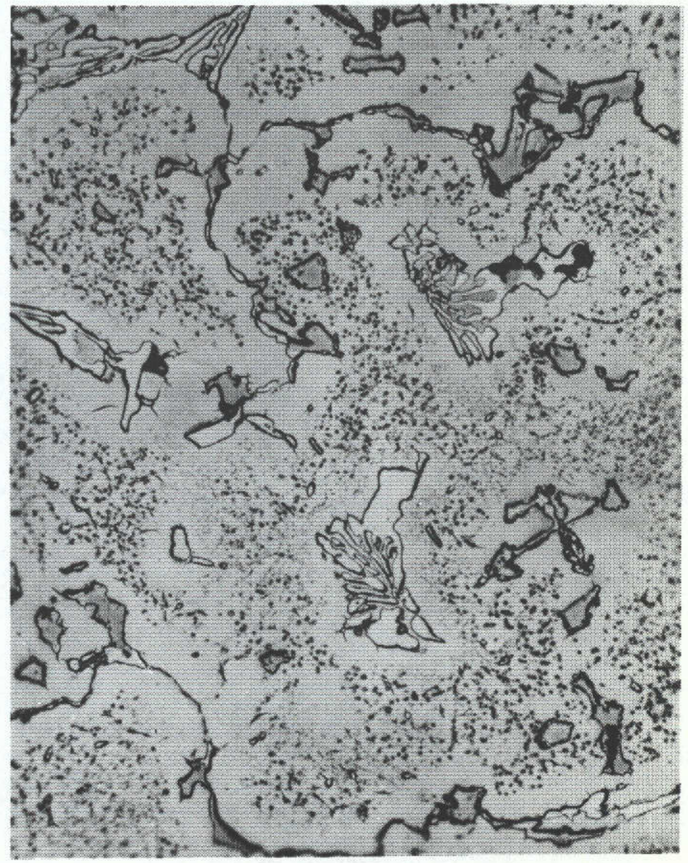

X500

Figure 25

Microstructure of RBH. Longitudinal section tested at 2065/675°F for 300 cycles. (10% H_2SO_4 electrolytic etch)

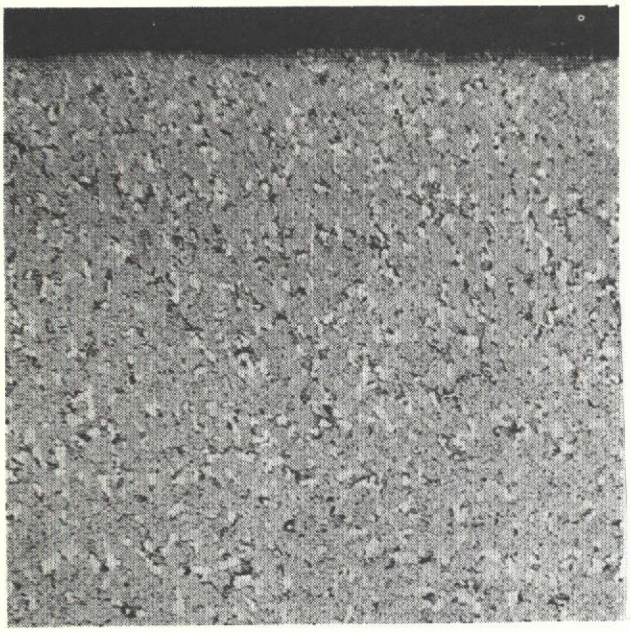

(a) X100
Longitudinal section tested at 2065/675°F for 300 cycles

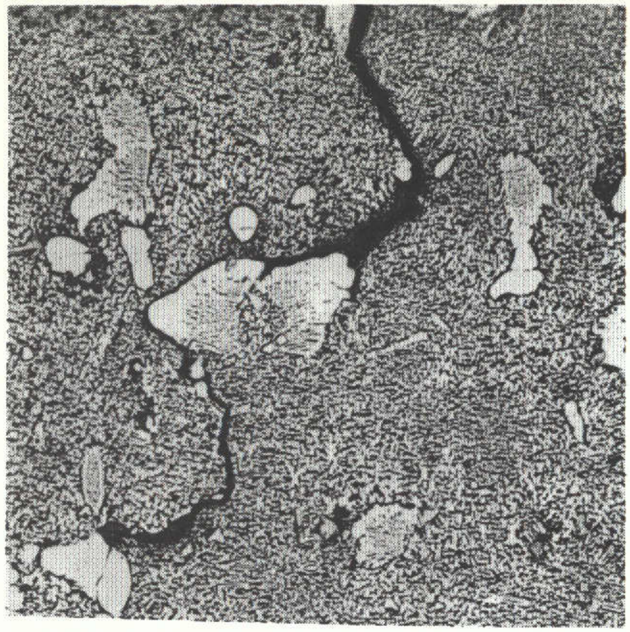

(b) X500
As (a), showing crack path

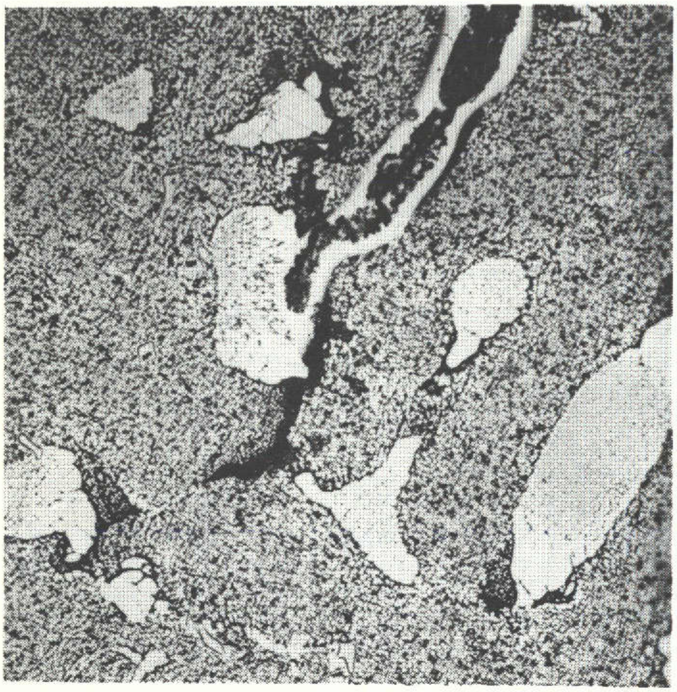

(c) X500
As (a), showing crack tip

Figure 26

Microstructure of NASA VI A Alloy (10% H_2SO_4 electrolytic etch)

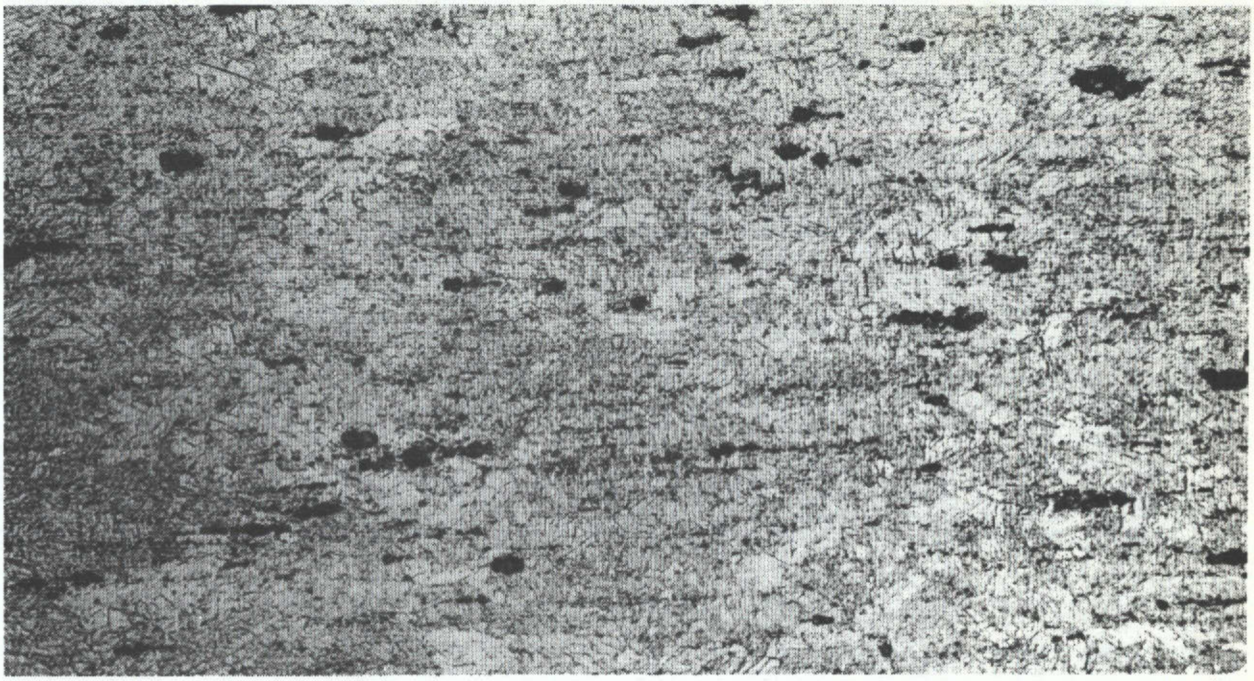

(a) X500

Untested transverse section from uniaxial specimen

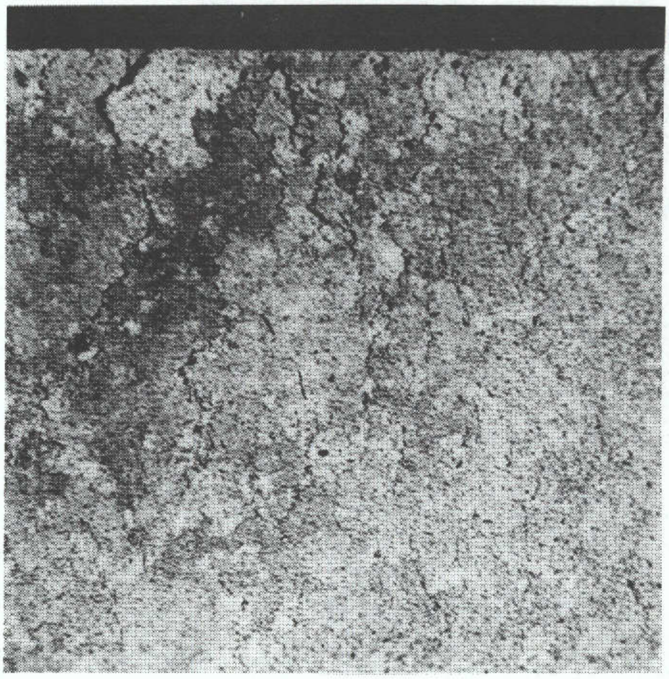

(b) X100

Longitudinal section tested at
2065/675°F for 200 cycles

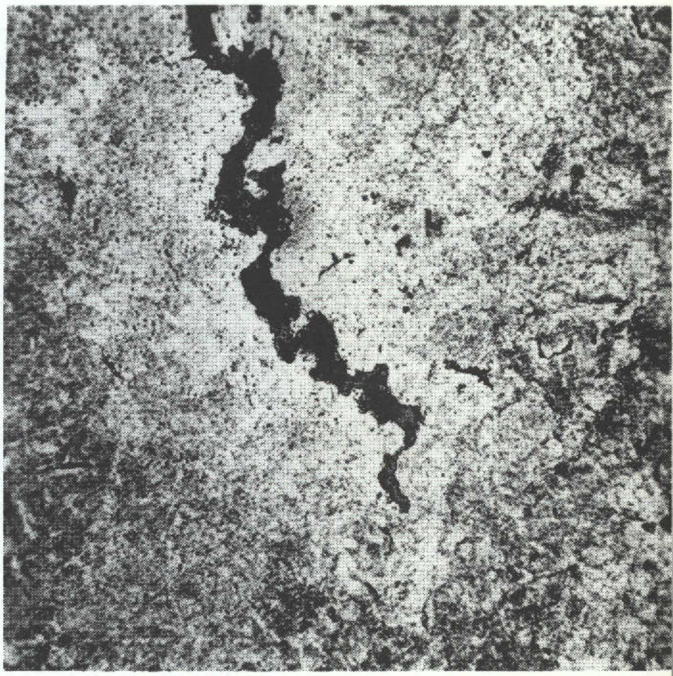

(c) X500

As (b)

Figure 27

Microstructure of TD-NiCr Specimens (Kalling's etch)

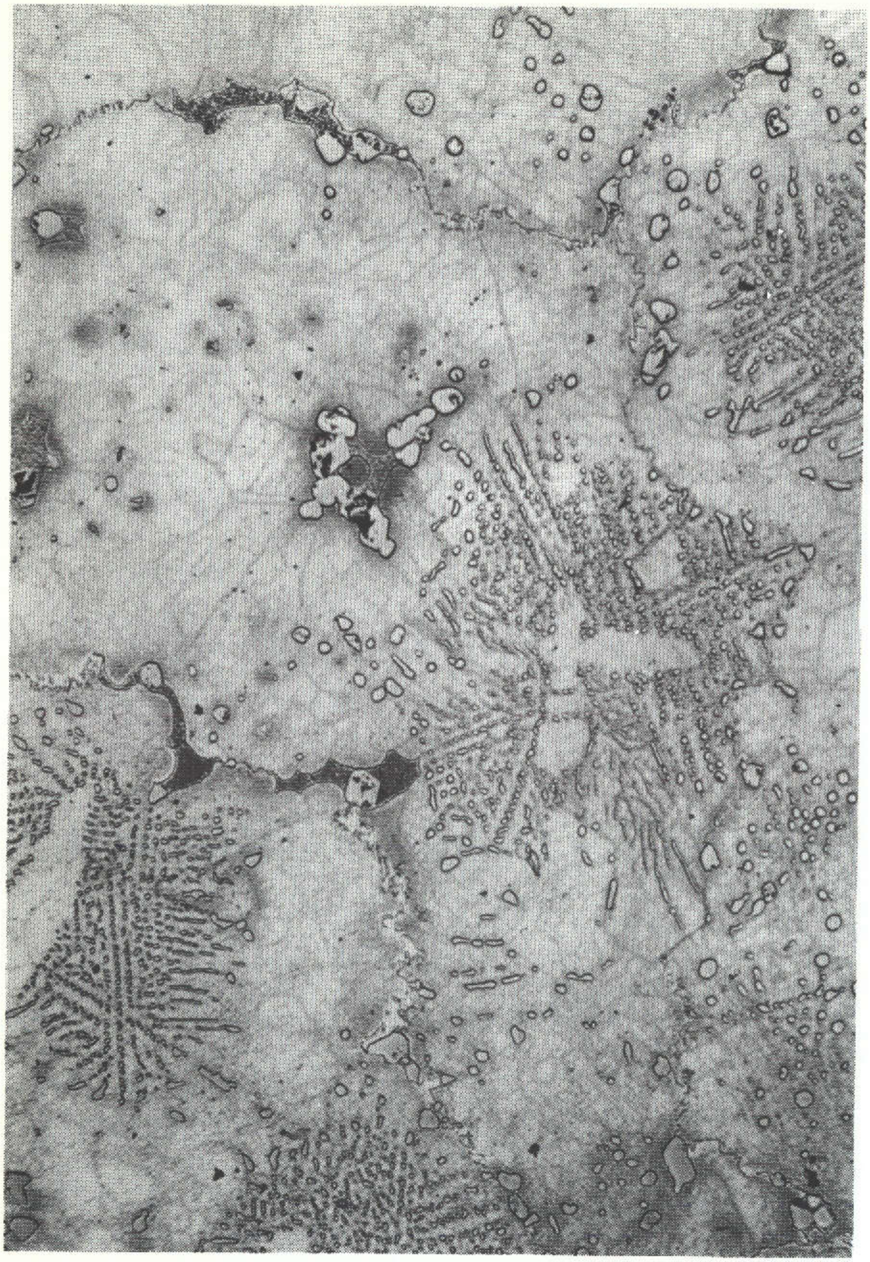

X500

Figure 28

Microstructure of MAR-M 302. Untested transverse section from uniaxial specimen. (HCl-CH_3COOH electrolytic etch)

Figure 29 500X

Microstructure of WI-52. Untested Transverse section from uniaxial specimen. (HCl-CH_3COOH electrolytic etch)

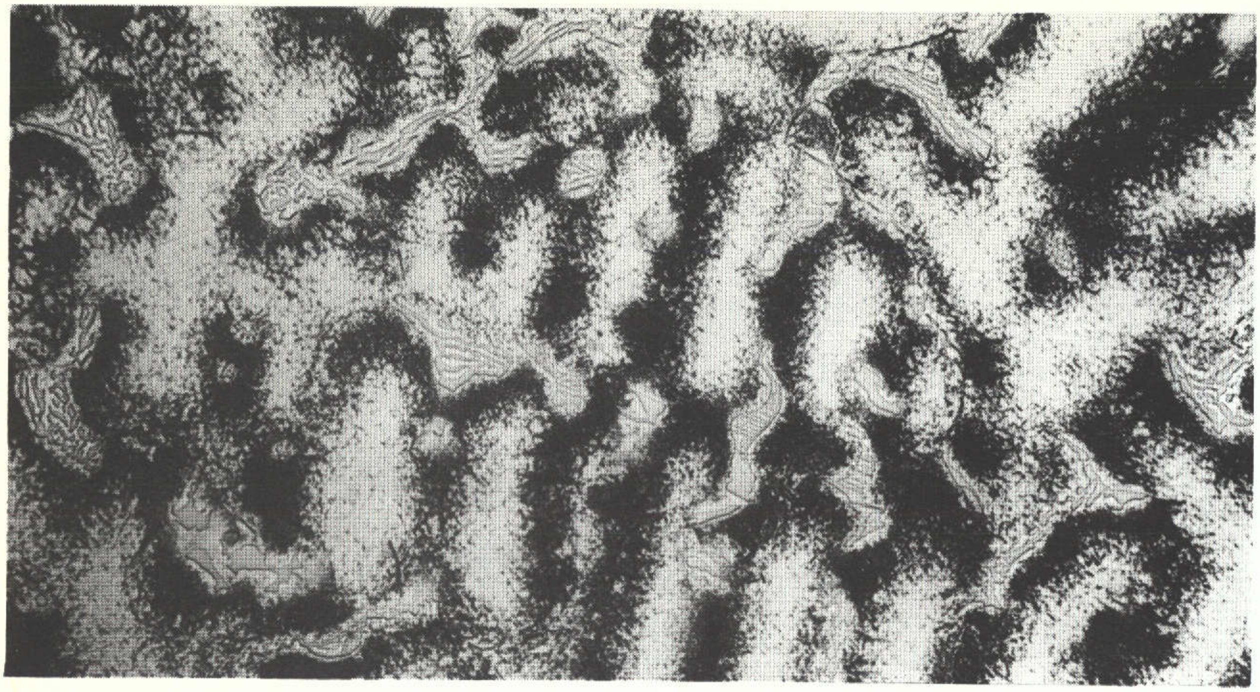

(a) X500
Untested transverse section from uniaxial specimen

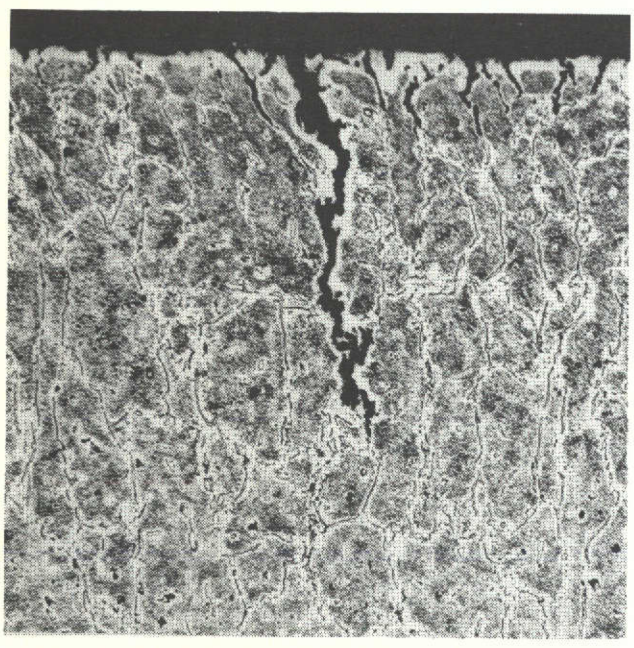

(b) X100
Longitudinal section tested at 2065/675°F for 300 cycles

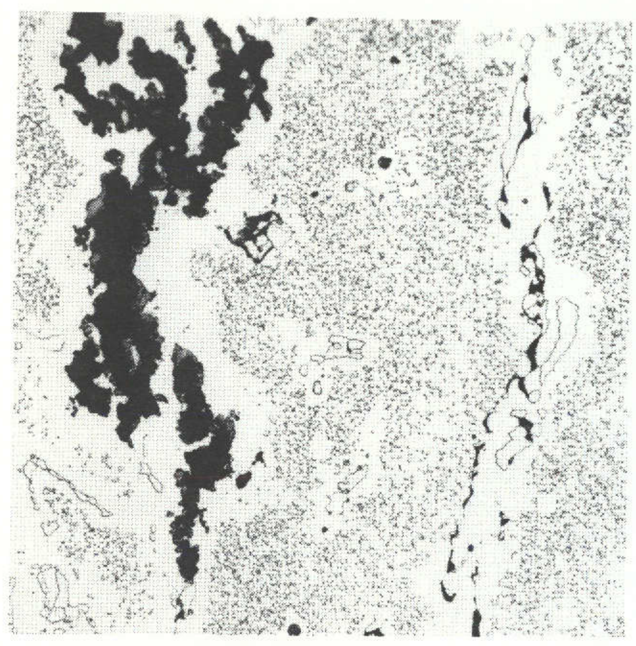

(c) X500
As (b)

Figure 30

Microstructure of X-40 Specimens (10% H_2SO_4 electrolytic etch)